

Diss. ETH No. 27639

# **Prospects for Additive Manufacturing and Hemolysis Testing in Blood Pump Development**

A thesis submitted to attain the degree of

Doctor of Sciences of ETH Zurich  
(Dr. sc. ETH Zurich)

presented by

**Kai von Petersdorff-Campen**

M.Sc. RWTH Aachen University  
born February 2, 1992  
citizen of Germany

accepted on the recommendation of

Prof. Dr. Mirko Meboldt, examiner  
Prof. Dr. Christofer Hierold, co-examiner  
Dr. Marianne Schmid Daners, co-examiner

2021

Kai von Petersdorff-Campen  
kaiv@alumni.ethz.ch

© 2021

ETH Zurich  
Product Development Group Zurich  
Leonhardstrasse 21  
8092 Zurich  
Switzerland

**pd** | **z** Product Development Group Zurich  
Produktentwicklungsgruppe Zürich

# Acknowledgments

My PhD research was part of the Zurich Heart Project, which is an interdisciplinary project among ETH Zurich, University Hospital Zurich and German Heart Institute Berlin. I am grateful to the initiators of this project and to the Stavros Niarchos Foundation, which have funded my research contribution to the Zurich Heart Project.

The successful completion of my PhD thesis has been made possible by the support and input of a number of people, whom I would like to personally thank below.

First of all, I would like to thank the members of my doctoral committee for their valuable mentorship. Prof. Dr. Mirko Meboldt accepted me as a PhD student and throughout the past years showed his unconditional support for all endeavors that I thought were worth pursuing. I am deeply grateful for the opportunity to have worked in such a special place as the Product Development Group Zurich and to have been able to carry out exciting projects with the greatest freedom. I would also like to thank Prof. Dr. Christofer Hierold for accepting to be my co-examiner and bringing his valuable expertise to the evaluation of this thesis. Thank you to Dr. Marianne Schmid Daners, who supported me in many ways and was always willing to stand up for my personal and research interests. She thereby created stability and the room for the successful execution and publication of my research.

I am very fortunate to have been surrounded by experienced and supportive colleagues who provided guidance and were always willing to give feedback. To name only one, I would like to thank Dr. Stefan Hovestadt, who inspired me to join the group and supported and motivated me beyond his obligations as a PhD student.

Some of the most inspiring discussions and creative moments I had were with my fellow doctoral students at the Product Development Group Zurich and Zurich Heart consortium. For these memorable times I would like to thank first and foremost Jonas Abeken, Matthias

Dupuch, Konstantinos Magkoutas, Martin Batliner and Jonas Conrad. I would also like to thank all the people who contribute to making the Product Development Group Zurich such a pleasant, yet a constructive working place. This includes Sara Mettler, Dario Fenner, Stefanie Dennis, Carole Haerry and many more.

Furthermore, my big thanks go to all my students who challenged me and supported me through their work: Yannick Hauswirth, Pascal Gutzwiller, Florian Mauz, Roman von Däniken, Seraina Saurenmann, Rick Saner, Jonas Enke, Damian Lenherr and Sandro Losa.

Last but not least, thank you to my family, to my close friends and to Johanna Klar. Your friendship and support have given me the drive to be able to complete this thesis.

# Contents

<b>Acknowledgments</b>	<b>iii</b>
<b>Abstract</b>	<b>ix</b>
<b>Zusammenfassung</b>	<b>xiii</b>
<b>Nomenclature</b>	<b>xvii</b>
<b>1 Introduction</b>	<b>1</b>
1.1 Background on ventricular assist devices . . . . .	3
1.2 Clinical need and progress of VAD technology . . . . .	11
1.3 Additive manufacturing . . . . .	15
<b>2 Summary of scientific contribution</b>	<b>21</b>
2.1 Integration of pressure sensors into titanium inflow can- nula with AM . . . . .	22
2.2 Novel AM process for fully additive-manufactured ro- tary pump prototype . . . . .	24
2.3 Investigation of the applicability of AM parts in func- tional VAD testing . . . . .	25
2.4 Improving methods for <i>in vitro</i> testing of blood damage	27
<b>3 Pressure and Bernoulli-based flow measurement via a ta-     pered inflow VAD cannula</b>	<b>29</b>
3.1 Introduction . . . . .	29
3.2 Material and methods . . . . .	32
3.3 Results . . . . .	40
3.4 Discussion . . . . .	46

Contents

<b>4</b>	<b>3D printing of functional assemblies with integrated polymer-bonded magnets demonstrated with a prototype of a rotary blood pump</b>	<b>53</b>
4.1	Introduction . . . . .	53
4.2	Materials and methods . . . . .	55
4.3	Results and discussion . . . . .	59
4.4	Conclusion . . . . .	64
<b>5</b>	<b>In vitro testing and comparison of additively manufactured polymer impellers for the CentriMag blood pump</b>	<b>65</b>
5.1	Introduction . . . . .	65
5.2	Material and methods . . . . .	66
5.3	Results . . . . .	73
5.4	Discussion . . . . .	80
5.5	Conclusion . . . . .	84
<b>6</b>	<b>Hemolysis testing in vitro: A review of challenges and potential improvements</b>	<b>85</b>
6.1	Introduction . . . . .	85
6.2	Challenges of <i>in vitro</i> testing of hemolysis . . . . .	87
6.3	Potential approaches for improving <i>in vitro</i> testing of hemolysis . . . . .	95
6.4	Conclusion . . . . .	108
<b>7</b>	<b>Potential factors for poor reproducibility of in vitro hemolysis testing</b>	<b>109</b>
7.1	Introduction . . . . .	109
7.2	Material and methods . . . . .	111
7.3	Results . . . . .	116
7.4	Discussion . . . . .	124
7.5	Conclusion . . . . .	127
<b>8</b>	<b>Conclusion and Outlook</b>	<b>129</b>
8.1	Conclusion . . . . .	129
8.2	Outlook . . . . .	131
<b>Appendix A</b>	<b>Survey on the current use of AM in VADs</b>	<b>137</b>
A.1	Summary of the survey results . . . . .	137

A.2 Questionnaire . . . . .	142
<b>Appendix B Pressure and Bernoulli-based flow measurement via a tapered inflow VAD cannula</b>	<b>149</b>
B.1 Manufacturing of cannula blanks . . . . .	149
B.2 Production of functional cannulas . . . . .	149
B.3 Thermal sensitivity calculation . . . . .	151
B.4 Algorithm for extraction of physiological features . . .	153
B.5 Validity of proposed analytical model . . . . .	154
<b>Appendix C In vitro testing and comparison of additively manufactured polymer impellers for the CentriMag blood pump</b>	<b>159</b>
C.1 Additive manufacturing processes . . . . .	159
C.2 Computational fluid dynamics simulation . . . . .	160
C.3 Mock circulatory loop for hydraulic measurements . .	162
C.4 Mock circulatory loop for hemolysis measurements . .	163
<b>Bibliography</b>	<b>165</b>
<b>Curriculum Vitae</b>	<b>193</b>





# Abstract

The treatment of heart failure with a ventricular assist device (VAD) is subject to various severe complications. Many of these complications originate in the VAD design, which in turn is a consequence of the VAD development process. Although additive manufacturing (AM), colloquially known as 3D printing, generally holds excellent potential for design and process improvements in engineering processes, the use of AM in VAD development is currently limited only to the very early prototyping stages and therefore, is not being used to its full potential. With AM technologies becoming increasingly mature, the key challenge for using AM in VAD design and development is to identify value-adding applications and overcome application-specific manufacturability and manufacturing quality challenges.

This thesis reports applications for AM in VAD development that enable design improvements through design integration as well as through the possibility of rapid design iterations. As a prerequisite for rapid design iterations, it furthermore reports anchor points for improving the hemolysis testing as the bottleneck testing procedure.

Firstly, the design integration potential of AM was investigated by embedding sensing functionality into a VAD. An inflow cannula of a commercial VAD was redesigned to integrate a sensing concept that enabled the measurement of total pressure and flow rate at an accuracy ( $\pm 0.6$  mmHg,  $\pm 0.14$  L/min) and resolution (100 Hz) required for continuous monitoring and future automatic adaption of the VAD to the patients' need. The use of AM for the fabrication of measurement channels enabled a miniaturized integration into the thin cannula wall.

Secondly, the limits of design integration with AM were investigated by developing and testing a functional pump prototype that was additively manufactured in a single production step. To enable the simultaneous integration of rotor and bearing magnets, a printable magnetic polymer compound was developed that could be used

## *Contents*

in combination with other polymers on a multi-material printer. The printed magnets had a remanence of 353 mT, which is about a third of sintered NdFeB magnets used in current VADs. Despite the insufficient manufacturing quality for medical use, the prototype could be operated at 1000 rpm and was able to deliver a low flow rate of 3 L/min, however, at a very low pressure head of 6 mmHg.

Thirdly, the potential of AM to enable rapid design iterations was investigated by replacing the original impeller of a commercial VAD with AM impellers and then comparing their hydraulic characteristics and the hemolysis induced. AM impellers were manufactured using four different AM processes. While hydraulic test results were only slightly influenced by the use of AM parts, a significant increase in hemolysis was observed depending on the surface roughness of the AM parts. Only impellers manufactured by stereolithography were comparable to the injection-molded original impeller regarding low surface roughness and hemolysis levels. The results indicate a threshold level of surface roughness that depends on the local level of wall shear stress and above which the surface contributes significantly to hemolysis.

In addition, the potential of accelerating the hemolysis testing procedures was investigated, as they represent a bottleneck of a rapid and iterative development process that AM can enable. The following three critical factors of a standard hemolysis test protocol for VAD development were identified: difficulty of obtaining blood, the high experimental workload, and the poor reproducibility of the results. To experimentally investigate the source of poor reproducibility, blood from 23 bovine donors was used for hemolysis testing in combination with a comprehensive blood analysis. The results showed that differences in the susceptibility to hemolysis between blood samples from different donors were the primary cause of poor reproducibility. Another result was that the adjustment of hematocrit to a standard level, as required by the standard protocol, might introduce additional between-donor variations. Additionally, potential approaches to reduce the complexity and workload of VAD hemolysis testing were reviewed, including the replacement of blood with standardized shear-sensitive fluids and the use of novel sensors for a simplified measurement of hemoglobin concentrations.

In conclusion, both design improvements through integration and process improvements through rapid design iterations can be achieved by AM of VAD components. However, the use of AM is restricted by low manufacturing quality, especially regarding surface roughness. To enable large-scale testing and iterative development with AM prototypes, bottlenecks in the *in vitro* validation of hemolysis have to be solved.



# Zusammenfassung

Bei der Behandlung von Herzinsuffizienz mit implantierten Blutpumpen treten häufig Komplikationen wie Schlaganfälle, innere Blutungen oder Infektionen auf. Ursächlich dafür sind Aspekte der Konstruktion und des Betriebs der Geräte, deren Kompatibilität mit dem menschlichen Organismus bei der Entwicklung nicht ausreichend berücksichtigt wurde. Additive Fertigung (AF), umgangssprachlich auch als 3D-Druck bezeichnet, kommt in der Blutpumpenentwicklung derzeit nur im frühen Prototyping zum Einsatz, wodurch das volle Potential für Konstruktions- und Produktionsverbesserungen nicht ausgeschöpft wird. AF-Technologien wurden in den letzten Jahren zunehmend ausgereift, sodass die zentrale Herausforderung für den Einsatz in der Blutpumpenentwicklung nun darin besteht, wertschöpfende Anwendungen zu identifizieren und anwendungsspezifische Hindernisse zu überwinden.

Im Rahmen dieser Arbeit wurden Anwendungen für die AF in der VAD-Entwicklung untersucht, die Designverbesserungen durch Designintegration sowie durch die Möglichkeit von schnellen Designiterationen ermöglichen. Weiterhin wurden Ansätze verfolgt, die Erhebung der durch Blutpumpen hervorgerufenen Blutschädigung zu erleichtern, da diese Untersuchungen ein limitierender Faktor in der VAD-Entwicklung sind.

Zunächst wurde die Anwendung von AF für die Integration neuer Funktionalität in eine Blutpumpe untersucht. Das entwickelte Konzept beinhaltet zwei Druckmesspunkte, die an verschiedenen Stellen innerhalb eines konischen Kanülenrohrs platziert werden, sodass sich die Durchmesser der Kanüle an den beiden Messpunkten unterscheiden. Entsprechend dem Bernoulli-Effekt haben die unterschiedlichen Flussgeschwindigkeit an den Messpunkten eine Differenz im gemessenen statischen Druck zur Folge. Darauf basierend können sowohl der Gesamtdruck als auch die Flussrate berechnet werden. Die Fähigkeit von AF zur Fertigung komplexer Strukturen ermöglicht hier eine mi-

## Contents

niaturisierte Integration mit einer weniger stark eingeschränkten Platzierung der Druckmesspunkte innerhalb der dünnen Kanülenwände. Die AF-Prototypen erlaubten die Bestimmung von Gesamtdruck und Flussrate mit der erforderlichen Genauigkeit und Auflösung zur Ermittlung der relevanten Metriken, auf denen Überwachungs- und Steuerungsalgorithmen basieren.

Um die Machbarkeitsgrenzen von AF in Bezug auf vereinfachtes Prototyping und auf Designintegration zu erschliessen, wurde in einer weiteren Studie ein funktionsfähiger Pumpenprototyp in einem einzigen Produktionsschritt additiv gefertigt. Die gleichzeitige Integration von Rotor- und Lagermagneten wurde durch die Entwicklung einer magnetischen Polymerverbindung ermöglicht, die zur Verwendung auf einem Multimaterialdrucker geeignet war. Die gedruckten Magnete hatten eine Remanenz von 353 mT, was etwa einem Drittel jener von gesinterten NdFeB-Magnete entspricht, die in aktuellen Blutpumpen verwendet werden. Trotz der für den medizinischen Einsatz unzureichenden Fertigungsqualität konnte der Prototyp mit 1000 U/min betrieben werden und war in der Lage, eine geringe Flussrate von 3 L/min bei einer niedrigen Druckhöhe von 6 mmHg zu erzeugen.

Weil bei AF die Fertigung ohne bauteilspezifische Werkzeuge erfolgt, werden bei der Fertigung kleiner Stückzahlen kürzere Vorlaufzeiten und niedrigere Produktionskosten erzielt als bei der konventionellen Fertigung. Dies ist besonders in der Prototypenfertigung interessant und erleichtert das Fertigen und Testen zahlreicher Designvarianten. Daher wurde zusätzlich die Eignung von AF-Teilen für den Einsatz in Prototypen untersucht, die *in vitro* hinsichtlich hydraulischer Eigenschaften und Hämolyse getestet werden. Vier gängige AF-Prozesse wurden hinsichtlich Wasseraufnahme, Fertigungsgenauigkeit und Oberflächenrauigkeit untersucht. Anschliessend wurde der Impeller einer kommerziellen Blutpumpe durch additiv gefertigte Impeller der gleichen Geometrie ersetzt. Für jedes AF-Verfahren wurde der Einfluss auf die hydraulische Leistung und die Hämolyse analysiert. Während die hydraulischen Testergebnisse durch die Verwendung von AF-Teilen nur geringfügig beeinflusst wurden, wurde ein signifikanter Anstieg der Hämolyse in Abhängigkeit von der Oberflächenrauigkeit

des Teils beobachtet. Nur die stereolithografisch hergestellten Impeller wiesen eine vergleichbare Oberflächenrauigkeit und Hämolyse auf wie der spritzgegossene Originalimpeller. Die Ergebnisse deuten auf einen von der vorliegenden Wandscherkraft abhängigen Schwellenwert der Oberflächenrauigkeit hin, oberhalb dessen die Oberfläche wesentlich zur Hämolyse beiträgt.

Eine weitere Erkenntnis dieser Studie war, dass die Anzahl durchführbarer Hämolysetests stärker begrenzt ist als die Herstellung von Prototypen mittels AF. Um die Voraussetzung für eine schnelle, iterative Entwicklung mit AF zu schaffen, wurde daher des Weiteren analysiert, welche Faktoren den Durchsatz von Hämolysetests begrenzen und wie diese adressiert werden können. Dabei wurden die Schwierigkeit der Blutbeschaffung, der hohe experimentelle Arbeitsaufwand und die geringe Reproduzierbarkeit der Testergebnisse als die Hauptfaktoren identifiziert und mögliche Lösungsansätze erarbeitet. Zusätzlich wurden in einer experimentellen Studie mit Blut von 23 Rindern die Ursachen und potentielle Ansätze zur Verbesserung der Reproduzierbarkeit von Hämolyseversuchen tiefergehend untersucht. Die Ergebnisse zeigten, dass Unterschiede in der Hämolyseanfälligkeit zwischen Blut von verschiedenen Spendern die Hauptursache für die schlechte Reproduzierbarkeit waren. Des Weiteren wurde gezeigt, dass die Standardisierung des Hämatokrits durch Verdünnung, wie im Standardprotokoll gefordert, zusätzliche Variation der Bluteigenschaften herbeiführt.

Zusammenfassend lässt sich sagen, dass sowohl Produktverbesserungen als auch Prozessverbesserungen durch AF von Blutpumpenkomponenten erreicht werden können. Der Einsatz wird jedoch durch die geringe Fertigungsqualität eingeschränkt, insbesondere bei noch nicht ausgereiften AF-Technologien, wie der AF von Magneten. Um den Übergang zur einer iterativen Entwicklung mit zahlreichen Tests mit AF-Prototypen zu ermöglichen, müssen weiterhin die Methoden zur *in vitro* Validierung der durch die Pumpen verursachten Hämolyse gelöst werden.





# Nomenclature

The following list explains the acronyms and abbreviations as well as Greek and Latin symbols used in the dissertation. They are listed in alphabetic order. Pressure analyses are performed in  $Pa$ , but are stated and depicted as  $mmHg$  ( $1\text{ mmHg} = 133.32\text{ Pa}$ ) as this is the common convention in the clinical environment. Viscosity is depicted either as centiPoise ( $cP$ ) or  $mPa \cdot s$  ( $1\text{ cP} = 1\text{ mPa} \cdot s$ ).

## Abbreviations and Acronyms

AM	Additive Manufacturing
ASTM	American Society for Testing and Materials
BSA	Bovine serum albumin
BVOH	Buteneiol vinyl alcohol copolymer
CFD	Computational fluid dynamics
ECMO	Extracorporeal membrane oxygenation
FDA	Federal Drug Administration
FDM	Fused deposition modeling
Hb	Hemoglobin
HF	Heart failure
HMC	Hybrid mock circulation
HTx	Heart transplantation
IC	Inflow cannula
IH	Index of hemolysis
IQR	Inter-quartile range
IR	Inflow reservoir
ISO	International Organization for Standardization
LDS	Large-diameter sensor
LV	Left ventricle
MagFil	Magnetic filament

## Nomenclature

MJ	Material jetting
MJF	Multi-jet fusion
OR	Outflow reservoir
PA12	Polyamide-12
PBS	Phosphate buffered saline
PC testing	Testing under physiological conditions
PLA	Polylactic acid
PLB	Plasma-like buffer
POM	Polyoxymethylene
PVC	Polyvinyl chloride
RBC	Red blood cell
RBP	Rotary blood pump
RMSE	Root mean square error
SD	Standard deviation
SDS	Small-diameter sensor
SEM	Scanning electron microscopy
SF testing	Static pressure testing with flow
SLA	Stereolithography
SLS	Selective laser sintering
SNR	Signal-to-noise ratio
SP testing	Static pressure testing
TCS	Temperature cross-sensitivity
TGA	Thermogravimetric analysis
VAD	Ventricular assist device
VWF	von Willebrand factor

## Latin Symbols

$a$	Density-dependent factor	$(g/cm^3)$
$AoP$	Aortic pressure	$(mmHg)$
$B_r$	Magnetic remanence	$(T)$
$c$	Geometric factor	$(1/m^{-4})$
$CAP$	Cardiac cycle averaged pressure	$(mmHg)$
$CAQ$	Cardiac cycle averaged flow rate	$(L/min)$
$CO$	Cardiac output	$(L/min)$
$CV$	Coefficient of variation	$(\%)$

## Nomenclature

<i>EDP</i>	End-diastolic pressure	( <i>mmHg</i> )
<i>ESP</i>	End-systolic pressure	( <i>mmHg</i> )
<i>H</i>	Pressure Head	( <i>mmHg</i> )
<i>Ht</i>	Hematocrit	(%)
<i>I</i>	Motor current	( <i>A</i> )
<i>LVP</i>	Left ventricular pressure	( <i>mmHg</i> )
<i>MCV</i>	Mean corpuscular volume	( <i>fL</i> )
<i>MPV</i>	Mean platelet volume	( <i>fL</i> )
<i>n</i>	Pump speed	( <i>rpm</i> )
<i>NIH</i>	Normalized index of hemolysis	( <i>mg/100L</i> )
<i>MIH</i>	Modified index of hemolysis	(-)
<i>p<sub>dynamic</sub></i>	Dynamic pressure	( <i>mmHg</i> )
<i>p<sub>hydraulic</sub></i>	Hydraulic power	( <i>W</i> )
<i>p<sub>mechanic</sub></i>	Mechanical power	( <i>W</i> )
<i>p<sub>static</sub></i>	Static pressure	( <i>mmHg</i> )
<i>p<sub>static,trans</sub></i>	Transmitted static pressure	( <i>mmHg</i> )
<i>p<sub>total</sub></i>	Total pressure	( <i>mmHg</i> )
<i>PHb</i>	Plasma hemoglobin concentration	( <i>mg/dL</i> )
<i>PIP</i>	Pump inlet pressure	( <i>mmHg</i> )
<i>Q</i>	Flow rate	( <i>L/min</i> )
<i>R<sub>0</sub></i>	Upstream radius of inflow cannula	( <i>mm</i> )
<i>R<sub>a</sub></i>	Roughness as arithmetical mean deviation from line profile	( <i>μm</i> )
<i>R<sub>L</sub></i>	Downstream radius of inflow cannula	( <i>mm</i> )
<i>r<sub>s</sub></i>	Spearman rank correlation coefficient	(-)
<i>R<sub>z</sub></i>	Roughness as maximum peak-valley distance on line profile	( <i>μm</i> )
<i>s</i>	Absolute flow speed	( <i>m/s</i> )
<i>S<sub>a</sub></i>	Roughness as arithmetical mean deviation of surface profile	( <i>μm</i> )
<i>SSL</i>	Systolic slope	( <i>mmHg/L/min</i> )
<i>T</i>	Motor torque	( <i>Nm</i> )
<i>t</i>	Sampling time	( <i>min</i> )
<i>tHb</i>	Total hemoglobin	( <i>g/dL</i> )

## Nomenclature

$u$	Absolute blade speed	( $m/s$ )
$V$	Volume	( $m^3$ )
$w$	Relative flow speed	( $m/s$ )
$WSS$	Wall shear stress	( $Pa$ )
$y^+$	Dimensionless wall distance	( $-$ )

## Greek Symbols

$\beta$	Blade angle	( $^\circ$ )
$\delta_v$	Laminar sublayer height	( $\mu m$ )
$\delta_{v,95}$	Laminar sublayer height corresponding to the 95th percentile WSS	( $\mu m$ )
$\eta$	Efficiency	(%)
$\mu$	Dynamic viscosity	( $cP$ )
$\omega$	Rotational speed	( $rad/s$ )
$\Phi$	Porosity	(%)
$\rho$	Density	( $g/cm^3$ )
$\tau_w$	Wall shear stress	( $Pa$ )

# 1 Introduction

Heart failure (HF) is a chronic condition in which the heart's pumping function progressively deteriorates and becomes insufficient to meet the body's perfusion need. It is the most severe form of cardiovascular disease and often develops if preceding conditions have damaged or weakened the heart muscle. Such preceding conditions are high blood pressure (hypertension), heart attacks (myocardial infarction), abnormal heart rhythms (arrhythmias), or congenital heart defects, such as faulty heart valves, that force the heart muscle to work harder than usual. Two distinct pathophysiological mechanisms can develop that impede the achievable stroke work: (1) Systolic heart failure ("pumping problem") is characterized by a weakened heart musculature that cannot contract vigorously enough and causes a reduction of ejection pressure. The ventricle does not empty properly, leading to the constant stretching and progressing dilatation of the ventricle. (2) Diastolic heart failure ("filling problem") is characterized by a stiffened heart musculature that cannot fully relax and causes a reduction of stroke volume.

HF affects about 1-2% of the population worldwide [1], which has led some to describe it as a global pandemic [2]. The American Heart Association reported 6.2 million new heart failure cases between 2013 and 2016 in the US alone and a one-year mortality of 22%. This corresponds to a proportion of 0.14% of the population dying from HF every year. HF primarily occurs in older patients, with more than 80% being 65 years of age or older [1]. Therefore, with an aging population worldwide, a further increase in HF cases is expected. In the US, the number of patients living with HF is projected to increase by 47% by 2030 compared to 2012 [3].

In the past, the transplantation of a donor heart was the most viable treatment option for advanced HF patients, where pharmacological therapy was insufficient. However, while the number of HF patients

## 1 Introduction

has steadily increased over the past decades, the number of heart transplantations (HTx) performed worldwide has remained relatively stable at 5,000/year due to a lack of additional donors [4]. Therefore, the implantation of mechanical blood pumps, so-called ventricular assist devices (VADs), has become an established cardiac support option for patients who are awaiting HTx, who are not candidates for HTx, or who are in myocardial recovery. Several devices have received regulatory approval as long-term applications in recent years, resulting in a progressive increase of VAD implantations (3,198 implantations in the US [5] in 2019). However, therapy with VADs is frequently associated with complications, such as gastrointestinal bleeding, strokes, or infections, which decrease long-term survival drastically (5-year survival of 43% [5]) compared to HTx (5-year survival of 70% [4]).

The Zurich Heart Project constitutes a multidisciplinary research initiative of the University of Zurich, the University Hospital Zurich, the German Heart Institute Berlin, and ETH Zurich, which aims to develop and apply new technologies for improved next-generation VADs. As part of the Zurich Heart Project, the goal of this work is to investigate the potential of additive manufacturing (AM) technologies to advance VAD technology. In recent years, several AM technologies have been developed to a high level of maturity. To push this technology to the VAD field value-adding applications need to be identified and application-specific hurdles must be overcome. In order to benefit from AM's ability to solve bottlenecks in prototyping, secondary bottlenecks, e.g., in testing said prototypes, must be avoided. Therefore, another goal of this work is to investigate how blood damage testing – an important part of the *in vitro* validation of pump designs – can be improved in terms of testing effort and reproducibility of results.

The following sections first introduce the current state of VAD technology and the typical test methods for VAD functionality during pre-clinical development (Section 1.1), second elaborate on the remaining clinical need and ongoing progress of VADs (Section 1.2) and third explain the benefits and challenges associated with the application of AM (Section 1.3). Chapter 2 identifies applications of AM in the VAD field that contribute to the continuing clinical need and motivates the studies further presented in this thesis (Chapters 3 - 7).

## 1.1 Background on ventricular assist devices

### 1.1.1 Therapy with VADs

VADs are mechanical pumps implanted at the left ventricle (LV) that are specifically designed to pump blood. The implantation necessitates a highly invasive surgery with the opening of the chest. The pump inflow cannula is sutured into a circular opening cut into the LV's myocardium. The pump outflow is connected to the aorta via an anastomosis. That way the VAD works in parallel with the diseased LV and assists in pumping oxygenated blood from the lungs to the body. VADs are driven electrically or hydraulically via a driveline that penetrates the skin on the patient's abdomen (Figure 1.1). While the first VADs were mainly used to keep patients alive until a donor heart was available (bridge-to-transplant), most of today's VADs have been approved as a destination therapy alternative to HTx (Figure 1.3) and are predominantly used accordingly (destination therapy, 73% in 2019 [5]). VAD systems includes body-worn battery packs that enable patients to receive up to 17 hours of battery-powered support [6].

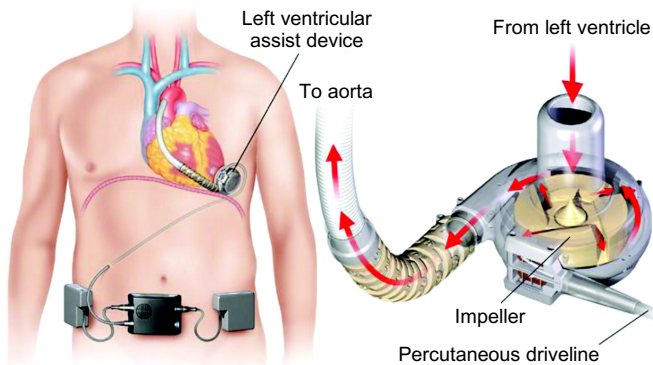


**Figure 1.1:** Implantation and components of the HeartWare ventricular assist device. Reused and modified with permission from [7], ©2012 American Heart Association, Inc.

## 1 Introduction

The treatment of an HF patient with a VAD is associated with high costs. In 2017 Shreibati et al. [8] reported that the average total cost for VAD implantation is \$175,000, which is more than twice the cost of HTx. A large fraction of the total cost is the acquisition cost of the device itself, which ranges between \$80,000 (HVAD, HeartWare [9]), \$95,000 (HeartMate3, Abbott [9]), and \$150,000 (HeartMate2, Abbott [10]). Additionally, VAD therapy necessitates close follow-up care and often leads to hospital readmission causing high costs of between \$167,000 and \$597,000 per life-year gained [8].

### 1.1.2 Evolution of VADs

A variety of different rotary blood pumps have been developed and introduced into the clinic. While the following section provides a concise summary of the history of VADs, a comprehensive overview may be found in [11, 12].

The first generation of VADs consisted of pulsatile pumps that aimed at imitating the heart's pumping mechanism. In such pumps, the volume of a blood chamber is changed periodically by displacement of a membrane or pusher plate, while one-way valves at the pump in- and outlet are used to deliver a directed pulsatile flow. However, poor patient outcomes, mostly extracorporeal use and a lack of durability have limited the use of such devices. Today, pulsatile pumps are only sporadically implanted, for example in pediatric patients [13].

A breakthrough in treatment success with VADs and the patients' quality of life came with the transition to pumps that use spinning turbodynamic impellers to deliver a continuous flow, which is controlled by the impellers' rotational speed. These rotary pumps are significantly smaller and allow the implantation of the pump within the pericardial space. Furthermore, they are driven electrically and therefore have thinner drivelines and produce less noise. Patients showed fewer adverse events and had a 30% higher survival rate than patients with pulsatile pumps [14]. Today this type of VAD is used almost exclusively.

An initial challenge of rotary, continuous-flow VADs was the frequent formation of blood clots at sites of high shear or stagnant blood flow. The technology thus has evolved in the last decade from shaft-



## 1.1 Background on ventricular assist devices

driven impellers and mechanical contact bearings to pumps with a contactless electromagnetic drive and hydrodynamic and magnetic bearings. Figure 1.2 shows conceptual schematics of the different systems for a radial pump. The pumps were increasingly optimized towards low shear forces as well as secondary flow paths to reduce blood damage and the occurrence of blood stagnation.

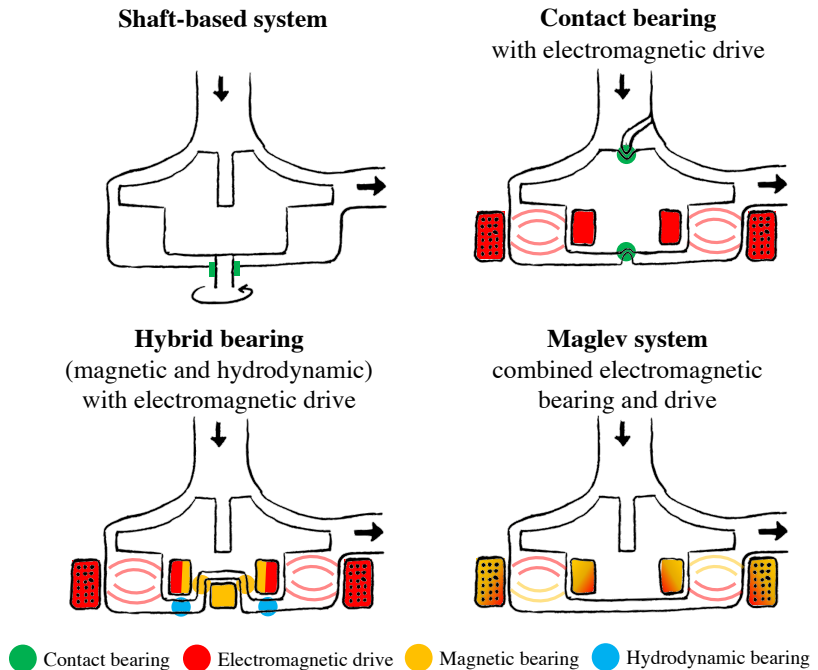


**Figure 1.2:** Drive and bearing systems used in axial and radial rotary VADs illustrated for a radial pump.

The most widely implanted VAD today is the HeartMate3 (Abbott, Chicago, IL, USA) (77% in 2019, [5]). It is based on the magnetic levitation technology. Magnetic bearing forces generated by coils inside the pump casing cause the impeller to levitate in the housing and at the same time provide radial stabilization and positioning. An

## 1 Introduction

additional rotating magnetic field generates the torque necessary for the impeller’s rotation. Radial position and rotational speed are constantly controlled by a feedback control loop. HeartMate3 shows a strongly reduced incidence of blot clot formation, which can be attributed to the large gap sizes and its periodic speed modulation (reduction and increase of rotor speed every 2 seconds for wash-out cycle and ”artificial pulse”). As shown in Figure 1.3, it thus has taken a large market share from VADs with mechanical or hybrid bearings in recent years.

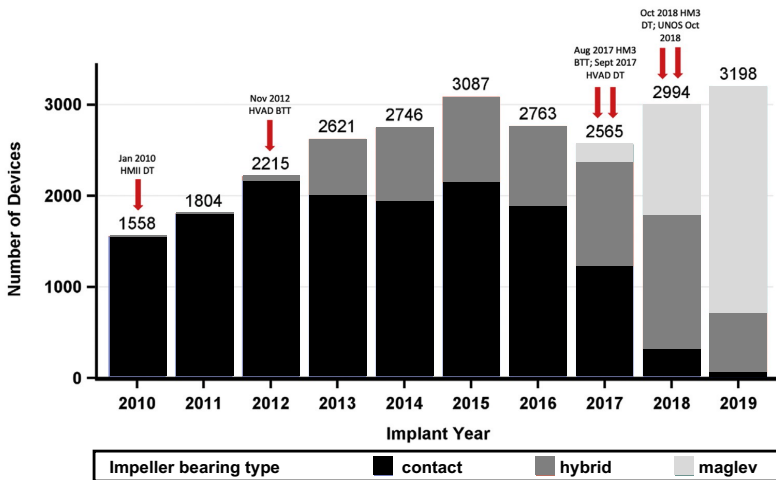


**Figure 1.3:** Evolution of VADs implanted in the United States captured by the Interagency Registry for Mechanically Assisted Circulatory Support from 2010 to 2019 color-coded by bearing type. The data includes patients that receive a VAD for the first time and for left-ventricular support only. Additionally, new device approvals are depicted (BTT, bridge to transplant; DT, destination therapy; HM3, HeartMate 3 (Abbott, Chicago, IL); HMII, HeartMate II (Abbott); HVAD, HeartWare Ventricular Assist Device (Medtronic, Minneapolis, MN); maglev, magnetically levitated; UNOS, United Network of Organ Sharing). Modified and reused with permission from [5], Copyright ©2021, Elsevier.

### 1.1.3 Working principle of rotary pumps

In a rotary pump, a rotating impeller's mechanical energy is transferred into hydrodynamic energy of the fluid. Rotary pumps are categorized into axial and radial flow pumps depending on whether the fluid is discharged parallel or perpendicular to the impeller's rotational axis. The following explanations refer to radial pumps. In such pumps, the liquid is set in rotation and accelerated outward by centrifugal force, creating suction at the pump inlet, which is located in the center of the impeller. After exiting the impeller the fluid is collected in a circumferential volute and deflected towards the pump outlet to generate a flow rate  $Q$ . Part of the fluid's kinetic energy can be converted into potential energy in the form of static pressure to overcome resistance to flow at the pump outlet, e.g. opposed by the vasculature. The difference in static pressure between inlet and outlet is called pressure head  $H$ . At higher resistance more energy is converted to potential energy, resulting in higher  $H$  and lower  $Q$ . The flow rate  $Q$  generated at a given  $H$  increases with the rotational speed of the impeller  $\omega$ . The pumping efficiency  $\eta$  at a specific operating point can be determined as the ratio of hydraulic power  $P_{hydrodynamic}$  generated and mechanical power  $P_{mechanical}$  consumed, with the motor torque  $T_{motor}$ .

$$\eta = \frac{P_{hydrodynamic}}{P_{mechanical}} = \frac{H \cdot Q}{\omega \cdot T_{motor}} \quad (1.1)$$

Both the relation of  $H$  and  $Q$ , as well as  $\eta$  at a given pump speed, depend on the fluid properties as well as the design of the impeller and volute. An important criterion for high values of  $\eta$  is a smooth and stable flow across the impeller blades. Smooth flow requires blades with angles of attack at both the leading and trailing edges matched to the flow streamlines. Adequate blade angles can be calculated using velocity triangles, indicating relative velocities on a single streamline. Figure 1.4 shows the velocity triangle at the leading edge of an impeller blade, where  $\omega$  is the rotational speed of the impeller,  $u$  is the absolute blade speed,  $s$  is the absolute flow speed of the fluid as given

## 1 Introduction

by the momentary flow rate, and  $w$  is the relative flow speed as seen by the blade. The adequate blade angle  $\beta$  is given by the angle of relative to absolute flow. An equivalent calculation can be performed for the blade angle at the trailing edge.

The blade angles can only be designed for one specific operating point. Off-design operation can negatively affect hemocompatibility and decrease hydraulic efficiency. It might also introduce instabilities that cause vibration in the pump system. A deviation of pump speed or flow rate from the design point causes a mismatch of the blade angles and the local flow vectors resulting in wake turbulence and flow vortices. This increases the shear stress on the blood and may promote thrombus formation by the introduction of stagnation zones. Furthermore, local reversion of the flow direction by turbulence and vortices leads to a decrease in the mean flow speed and efficiency. Hence, one goal in pump design is to maximize the tolerance for off-design operation. For example, the shape of the blade tips can positively influence the blades' compliance for high incidence angles and enable a broader range of the allowable operating conditions [15,16].

### 1.1.4 Pre-clinical testing of VAD functionality during development

The development and approval of VADs require extensive testing to verify the performance under various conditions and ensure device safety in clinical use. Clinical trials are the final validation step, but they are contingent on the prior successful demonstration of the new product or feature in live animal models. However, animal trials are associated with high costs and animal sacrifice. Several *in silico* and *in vitro* validation methods are available to develop and test new concepts and prototypes at various fidelity levels. As these methods allow to reduce the number of animal experiments and the risk of failure in clinical use, they are essential for developing any new VAD and subject to continuous development and improvement. The most relevant *in silico* and *in vitro* methods for the technical validation of VADs are briefly presented below, along with the most important optimization criteria in research and pre-clinical development: hydraulic

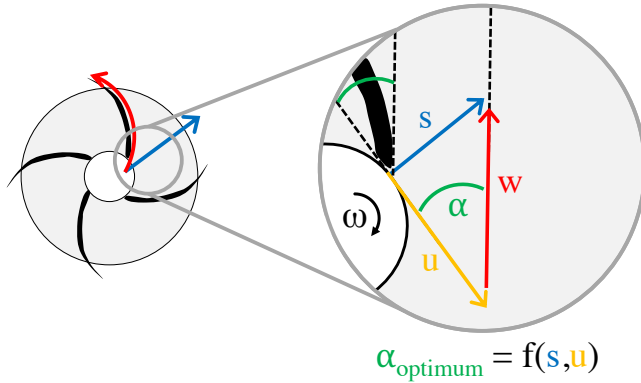


**Figure 1.4:** Velocity triangle at the leading edge of an impeller blade, with the blade speed  $u$ , the absolute fluid velocity  $s$ , the relative fluid velocity as seen by the leading edge  $w$  and the angle of attack at the blade's leading edge  $\alpha$ . The leading edge should ideally be aligned with the relative fluid velocity. The optimum angle of attack hence depends on a specific operating point determined by the blade speed  $u$  and the absolute fluid velocity  $s$ .

performance, flow-field-related hemocompatibility, and the interaction of the system with the cardiovascular system. Additional testing and documentation may be required for regulatory approval, but they are not addressed here.

### Hydraulic performance

Determining the characteristic relationships, such as those among pump speed, pressure head, flow rate, and efficiency, is vital for an understanding of the operational behavior of the VAD. *In silico* methods, such as computational fluid dynamics (CFD) simulations, are one option to determine those characteristics, but their use is usually not feasible due to the high computational cost. It is therefore preferable to perform tests with physical prototypes on hydraulic test setups. In such setups, the VAD under test is connected to a circulatory loop filled with viscosity-matched blood analogs such as glycerol-water mixtures. Automated test benches systematically vary pump speed, pres-

## 1 Introduction

sure head, and flow rate and record the characteristic curves. Such setups can also be used for testing durability or heat generation.

### **Flow-field-related hemocompatibility**

Since VADs are long-term implants with constant blood contact, it is imperative to test the potential blood damage induced. While material-induced blood damage is known from other blood-contacting medical devices and can be addressed by appropriate material selection, the non-physiological flow fields in VADs are a unique feature that must be considered separately. A common representative measure of flow-field-related hemocompatibility is the release of hemoglobin into the blood plasma, termed hemolysis. A variety of VAD design studies applied computational methods to assess hemolysis that derive an index of hemolysis (IH) from integrating shear forces and exposure times present in the VAD [17–19]. However, the computationally determined IH performs poorly in predicting experimentally measured hemolysis [20]. Therefore, experimental hemolysis testing, in which animal or human blood samples are circulated and where the rate of hemoglobin release is determined, remains an important development tool for a hemocompatible VAD design.

Such hemolysis tests are a measure of the accumulated damage to the blood as it passes through the VAD. However, they do not provide any information about local causative phenomena. For a spatially resolved analysis of shear forces, flow velocities, pressures, and the like, CFD simulations are a powerful tool. However, CFD results should be validated by *in vitro* tests, such as analysis of flow patterns visualized by particle image velocimetry [21].

### **Interaction with the cardiovascular system**

Another essential test field is the interaction of VADs with the patient’s systemic circulation. One example is the impact of residual pulsatility of the diseased heart on the hydraulic characteristics of the VAD. Such dynamic conditions can be simulated *in silico*. However, using hybrid mock circulation (HMC) test benches with a physical interface to the VAD and using numerical patient models to mimic the

## 1.2 Clinical need and progress of VAD technology

patient's heart and vasculature is often more efficient. Another example concerns the human body's response to changes in pump output, such as is relevant in the development of physiologically controlled VADs. Such tests can either be performed *in silico* with simulations that comprise a numerical model of the human blood circulation and an analytical model of the hydraulic behavior of the VAD or *in vitro* using prototypes and an HMC test bench.

## 1.2 Clinical need and progress of VAD technology

Even though VAD technology has improved, many adverse events still occur during VAD therapy, leading to severe complications, frequent hospital readmission, or death. Only about 20% of all patients remain free of adverse events two years after implantation, with the most significant risk of death posed by strokes, multiorgan failure, and infections [22]. Engineering-related VAD research nowadays focuses mainly on three fields to achieve a further improvement of the various devices regarding patient survival and quality of life: *improved hemocompatibility*, *full implantability*, and *hemodynamic monitoring and control*.

The following sections address the underlying need for each of these fields, presenting the progress already made, and the building blocks still missing, thus defining the scope for the search of value-adding applications of AM.

### 1.2.1 Improved hemocompatibility

Many adverse events are related to limited hemocompatibility originating from exposure of blood to non-physiological flow fields and non-biological surfaces.

The impeller's high rotational speed, the small clearance from the impeller to stationary parts, and turbulent flow lead to elevated shear stresses on the blood. As a result, the behavior of blood components such as cells and proteins may be changed, e.g., resulting in hemolysis, von Willebrand factor (VWF) degradation, and platelet activation. While triggered chain reactions have not been fully understood,

## 1 Introduction

such shear-related blood damage has often been associated with complications such as gastrointestinal bleedings and clot formation [23]. Furthermore, residual cardiac pulsatility may cause unfavorable flow conditions with stagnant blood in the VAD, promoting blood clots that can block the pump or detach and cause a stroke. The latest generation of VADs uses contactless active magnetic bearings and large-gap designs to reduce shear forces and avoid stagnation. However, success in reducing adverse events thus far has been limited [24]. Hence, understanding the impact of pump design on blood damage remains an important topic of research which has also been pursued within the Zurich Heart Project [25,26].

Another concern is blood contact with artificial materials, which can result in the activation of platelets and coagulation cascades [27]. Therefore, many commercial VADs have incorporated passive coatings with improved hemocompatibility, such as titanium nitride and diamond-like carbon, active coatings like heparin inhibiting fibrin clots, or porous surfaces promoting adhesion of autologous proteins and cells after implantation ("pseudointima"). As a need for further improvement remains, current research is directed at growing a layer of endothelial cells on the VAD's luminal surfaces before implantation [28,29]. However, cellular coatings remain limited to application in low-shear regions of the pumps.

### 1.2.2 Full implantability

The exit site of the driveline is an entry point for pathogens and is responsible for severe infections seen in 20% of VAD patients [30]. Moreover, the driveline is a major disruptor of quality of life. Many patients report concerns about the driveline position during sleep, intercourse, dressing, or showering [31,32].

Concepts for fully implantable VADs have been developed ever since the first VADs, including efforts for nuclear-powered devices [33]. Today's leading concept is to power the VAD via an implanted battery charged using transcutaneous energy transfer systems. Although all the necessary technologies have been available for decades, efforts to bring such a system to market have only recently materialized. For example, both Abbott and Medtronic filed development efforts for a



## 1.2 Clinical need and progress of VAD technology

fully implantable VAD with the Federal Drug Administration (FDA) in 2020 and 2019, respectively [34,35].

Next to advances in battery technology, a reduction of VAD power consumption is essential for extended periods of battery-powered operation. Current VADs have efficiencies of around 30% [36], which is substantially lower than the 89 – 95% achieved by industrial rotary pumps [15]. On the one hand, this is due to leakage flow through large gaps and secondary flow channels, which is deliberately accepted to reduce shear stresses and improve washout. On the other hand, it indicates design potentials that have not yet been fully exploited, even considering the trade-off with hemocompatibility.

### 1.2.3 Hemodynamic monitoring and control

Hemodynamic parameters describe all metrics related to pressures, flow rates, and volumes in the patient’s circulation and the VAD. Continuous hemodynamic monitoring provides information on the patient status and enables informed decision-making by clinicians. For example, pump flow is used by clinicians to adjust pump speed and serves as an indicator of pump thrombosis, right heart failure, and hematocrit changes [37]. Additionally, contractility, suction events, arrhythmias and the status of the aortic valve can be deduced from the flow waveform [37]. With the exception of the aVAD and HeartAssist5 pumps (ReliantHeart, Houston, Texas, US), that include flow probes, to date, no commercially available VAD is capable of monitoring hemodynamic parameters leaving patients unsupervised once they are discharged from the hospital. However, concepts of VAD-integrated hemodynamic monitoring have been researched over the last decades. Among those are concepts for measuring left-ventricular volume [38] and a new concept for the biocompatible integration of a pressure sensor into the inflow cannula [39], developed within the Zurich Heart Project. Other approaches rely on the estimation of hemodynamic parameters from pump-intrinsic signals, such as power consumption. However, the transition to clinical application so far has largely been lacking.

Continuous hemodynamic monitoring could also enable the automatic adaption of the support from the VAD depending on the pa-

## 1 Introduction

tient’s perfusion needs. Currently, the pump speed is set once by the physician before the patient is discharged home. However, depending on the physical activity, the need for support may change. This results in inadequate VAD settings known to cause complications in the long term [40–42] which force patients to limit their range of physical activity. Given the advances in fully implantable devices, this issue is expected to become more pressing as the patients’ mobility, and thus their range of physical activity is likely to increase. Several control algorithms that rely on hemodynamic data have been developed in the past decade. The ability of such controllers to prevent over- and underpumping in various scenarios of physical activity and during pathophysiological events has been shown *in vitro* using a hybrid mock circulation test bench [43].

One challenge of physiological VAD control is a potential increase of off-design operation. As described in Section 1.1.3, the geometries of the pump housing and impeller are optimized for a specific operating point, i.e., an optimal operation with undisturbed flow fields is only given at a specific flow rate and pressure. It has already been observed that off-design operation, e.g., due to HeartMate3’s artificial modulation of pump speed [44] or at reduced flow rates in pediatric patients [45] is associated with disturbed flow fields and adverse outcomes. To prevent permanent off-design operation in future adaptive VADs, new pump designs with operating ranges covering a broader spectrum of support scenarios have to be developed.

In summary, pump design is a critical factor in the important remaining VAD challenges. Therefore, it is subject to several design objectives: hemocompatibility, efficiency for full implantability, and tolerance for off-design operation. In addition, the development of fully hemocompatible surfaces and the integration of sensors to provide data for the physiological control of VADs are fields where further research advances are needed.

## 1.3 Additive manufacturing

Since this work aims to investigate the impact of AM on VADs, the following sections highlight the unique characteristics of AM and outline the potential benefits that the application of AM can offer. The current challenges limiting the use of AM are summarized as well.

### 1.3.1 Unique characteristics of additive manufacturing

AM refers to a vast ecosystem of manufacturing technologies that can transform digital representations of parts into physical objects and create products by adding material rather than subtracting it. Those technologies share two fundamental characteristics – *layer-by-layer building* and *tool-free production*.

#### Layer-by-layer building

First is the ability to build three-dimensional objects through the layer-by-layer addition of material. It enables the production of complex components without additional effort. This is often referred to as complexity advantage. In a first approximation, the manufacturing costs are independent of a component's complexity, whereas in conventional manufacturing, the manufacturing costs usually increase with the complexity of the components. Although AM does not come without limitations, it generally offers greater design freedom than conventional manufacturing and can even enable the production of structures that cannot be manufactured conventionally. Applications that take advantage of this characteristic of AM have been summarized as function-driven applications. Here, AM is used to achieve a functional product improvement by exploiting the full freedom of design offered by AM. A transfer to conventional manufacturing in such cases is not possible without major redesigns. Recent developments in AM technology and the availability of printable materials open the door for the next level of function-driven applications of AM. While common AM processes allow single-material parts production, newer processes allow voxel control of material and composition. This evolution from layer-by-layer to voxel-by-voxel manufacturing adds the

## 1 Introduction

dimension of local material properties to the previously purely geometric complexity advantage. The resulting applications are manifold. A term frequently used in this context is 4D printing. This refers to manufacturing components containing materials such as hydro- and thermal-reactive polymers and magnetic compounds that can be actuated or geometrically changed by external stimuli, thereby adding a temporal dimension.

### **Tool-free production**

The second characteristic of AM is its ability to manufacture various parts with no individual tooling. This enables the elimination of upfront tooling costs when manufacturing a new product. In a first approximation, the manufacturing cost is therefore independent of the lot size. In contrast, in conventional manufacturing, manufacturing costs usually decrease with lot size as the upfront tooling costs can be allocated to a larger number of units. This is often referred to as small-lot-size advantage. Applications that take advantage of this characteristic of AM while maintaining conventional design have been summarized as manufacturing-driven applications. Here AM is used to achieve process improvements in the development, deployment, or provision of products. Since the invention of the first AM process more than 30 years ago, numerous processes for layered manufacturing have been developed. Furthermore, both the machines' productivity and the quality of machined parts have increased by orders of magnitude. Nowadays, it is possible to manufacture components of end-user quality from a wide range of materials, including plastics, metals, ceramics, and biological materials, as well as a wide range of dimensions from micromachines to buildings. This progress has enabled the shift of AM from a sole prototyping technology to a manufacturing technology with industrial relevance. However, while the global market grew annually by 45% from 2017 to 26.5 billion US dollars in 2021 [46], a recent study found that 63% of industrial AM users still use AM for prototyping purposes. Only 21% use AM for items that cannot be otherwise manufactured [47]. To further capitalize on the innovation potential of AM, users need to understand the added value and challenges of using AM and select the right applications. Therefore,

the following sections highlight the typical clusters of the value-adding application of AM and the critical challenges in its use.

#### 1.3.2 Value-adding clusters of AM application

Fontana et al. [48] defined seven clusters of value-adding applications that can help companies identify where the replacement of conventional manufacturing by AM is advantageous.

##### **Prototyping**

Quick iterations over different designs and concepts for early design validation and faster time to market. Leveraging the cost advantage at small lot sizes.

##### **Enhanced designs**

Reduced manufacturing constraints for optimizing product design, e.g. for weight reduction or integration of functions. Leveraging the complexity advantage.

##### **Process concentration**

Simplification and consolidation of designs towards a reduction of process steps, e.g., manual work for assembly. Leveraging the complexity advantage.

##### **Production tools**

Cost-efficient production of molds or tools for indirect processing. Leveraging the cost advantage at small lot sizes or the complexity advantage.

##### **Custom products**

Increasing simplicity of product differentiation for individually customized products without additional retooling. Leveraging the cost advantage at small lot sizes and the complexity advantage.

##### **Incremental product launch**

Flexibility to update the design even after the sale of the first units for easy implementation of customer feedback. Leveraging the cost

## *1 Introduction*

advantage at small lot sizes.

### **Improved delivery**

On-demand manufacturing of different products without tooling change for a reduction of stocks. Leveraging the cost advantage at small lot sizes.

### **1.3.3 Challenges of AM application**

Despite the clear advantages of AM, its application is subject to various challenges. The right application fields must be identified and application-specific obstacles overcome to create economical value. Technical, design-related, economic, and capability challenges are summarized below.

#### **Technical challenges**

Technical challenges exist primarily in the area of materials and manufacturing processes. While there are globally accepted norms and standards for the specification and qualification of conventional manufacturing materials, such standards do not yet exist for the newer AM technology. Additionally, many AM processes struggle with maintaining low tolerances in geometry and surface properties as well as with process stability. Both aspects affect the quality and reproducibility of the parts. This limits the use of AM parts in applications where accuracy is critical or necessitates costly post-processing. Furthermore, the applicability of AM is constrained by limitations in production throughput and build size.

#### **Design challenges**

Product design is determined not only by customer requirements but also by the manufacturing process chosen. As highlighted above, AM can provide process advantages even without deviating from conventional design. However, to leverage the capabilities of AM to improve product function, engineers must let go of established product design principles and rethink the entire product structure. Constraints shift from manufacturing to engineering capabilities, requiring the develop-

ment of new design tools to fully exploit complexity advantage of AM.

#### **Economic challenges**

In addition to the engineering-related implications, the use of AM also has far-reaching influences on product economics. As stated above, AM has a different production cost structure than conventional manufacturing. Furthermore, new product design can enable cost savings in assembly, shorter supply chains, and at the end-user. Developers who have to identify a business case for AM application are challenged to quantify and factor in these implications. With an unclear competitive advantage, investments into a switch to AM will remain to be addressed with caution.

#### **Capability challenges**

Overcoming the above challenges to AM transition will require a workforce with new engineering and management skills. The challenge is to find talent that understands AM's holistic capabilities and can apply them to real-world production.





## 2 Summary of scientific contribution

As outlined in Section 1.2, there is a clinical need to further improve VADs, especially regarding sensor integration and pump design. At the same time, AM has been recognized to have the potential to improve products as well as development and fulfillment processes. The goal of this thesis was to investigate the potential of AM for VAD design and its development process.

To guide the selection of projects pursued within this thesis, a survey on the use of AM in the VAD space was conducted among individuals involved in VAD development. The results are fully presented in Appendix A. They showed that the application of AM in the VAD sector currently is strongly limited to early prototyping, which can be attributed to the perception of a majority of respondents that AM parts are of insufficient quality for functional *in vitro* testing or for use in the final product. The limited use of AM may further be due to the fact that many of the advantages of AM (Section 1.3.2) do not fit the VAD market and its regulatory framework. As described in Section 1.1.4, the development of VADs requires extensive testing for the validation of performance and safety. Every design or material change implies that large parts of the validation required for market approval must be repeated. Therefore, leveraging the freedom AM offers for late or continuous design changes, such as incremental product launch or custom products, is not applicable. Another particularity of the VAD field is that the production and distribution costs of VADs are marginal in relation to their selling price. The economic pressure to cut those costs thus is low, which renders the application of AM for process concentration or improved delivery less relevant.

However, from a business perspective the following prospects of AM application are applicable: gaining a competitive advantage by improving product functionality (function-driven application) and lowering time to market by accelerating product development (manufacturing-driven application). Given its current limited use, it seems that

## 2 Summary of scientific contribution

the potential of AM in the VAD field has not yet been exhausted. Based on these insights and given the open challenges with VADs, the following four objectives were defined for this thesis. The respective approaches are summarized in Sections 2.1 - 2.4:

1. **Integration of pressure sensors into titanium inflow cannula with AM**

Leveraging the complexity advantage of AM to integrate pressure sensors into a commercial VAD for continuous hemodynamic monitoring (function-driven application).

2. **Novel AM process for fully additive-manufactured rotary pump prototype**

Proof-of-principle for novel multi-material, voxel-by-voxel AM process to investigate the feasibility of a fully additively manufactured rotary pump.

3. **Investigation of the applicability of AM parts in functional VAD testing**

Identifying factors relevant to the applicability of AM prototypes in hydraulic and blood damage testing for accelerating pump design validation (manufacturing-driven application).

4. **Improving methods for *in vitro* testing of blood damage**

Investigating potential improvements of the efficiency and reproducibility of blood damage testing *in vitro* to enable large-scale testing with AM prototypes.

### 2.1 Integration of pressure sensors into titanium inflow cannula with AM

One application of AM that is often discussed is the integration of sensors, where the complexity of AM advantage enables or facilitates their integration at poorly accessible locations [49]. In particular, AM's ability of creating internal and curved channels offers multiple

advantages, e.g. for pressure transmission or for cable routing. Such channels offer great freedom in the placement of sensors without introducing further complexity in manufacturing and assembly and while keeping a small footprint. Additionally, the AM's layer-by-layer fabrication characteristic offers full access to the inside of manufactured parts. The manufacturing process of a part can be interrupted to place a sensor inside of a part already during manufacturing, thus further reducing assembly steps and sensor packaging issues.

As described in Section 1.2.3 the integration of sensors in VADs for the continuous monitoring of hemodynamic parameters, especially LV pressure and pump flow, is essential to address clinical needs. A preferred location for sensor integration is the inflow cannula as it reaches into the LV. Here, a space-saving integration is of particular importance as any increase in wall thickness for sensor integration limits the diameter available for blood flow at a given implant size.

As part of the Zurich Heart project, an approach for integrating a pressure sensor in the sidewall of a VAD inflow cannula has been developed and refined [39, 50]. This concept comprises a suspended parylene membrane that provides a hemocompatible interface to the blood and transmits pressure to a silicone oil-filled cavity in which a piezoresistive absolute pressure sensor is located. One challenge of this concept arises from the placement of the sensing interface on the inner wall of the tubular inflow cannula. According to Bernoulli's principle, the static pressure transmitted by such a sensing interface depends on the blood flow rate. For a cannula of 10 mm diameter and peak flows of 10 L/min, the measured pressure would deviate from the total pressure of interest by about 17 mmHg. Simultaneous measurement of the blood flow rate would not only serve several clinical purposes but would help account for this undesired deviation.

In this study, a concept was developed to derive both total pressure and flow rate from two pressure measurement points placed at different flow diameters within a cannula. The HeartMate3 was chosen to demonstrate the transferability of this concept to a commercial VAD, as its cannula is conically shaped and thus offers a varying diameter for the placement of sensing sites. Prototypes were additively manufactured from titanium, which allowed the integration of curved internal oil channels for pressure transmission. This design enabled

## 2 Summary of scientific contribution

the placement of the pressure transmission points in thin-walled areas of the cannula independent of the position of the more sensing elements. Thereby, the size, function, and implantability of the original cannula design was maintained. The prototypes were tested under physiological conditions on a hybrid mock circulation test bench to validate the design concept and the fabrication process.

The study is presented in detail in Chapter 3. It was conducted in collaboration with Matthias Dupuch (Laboratory for Micro- and Nanosystems, Department of Mechanical and Process Engineering, ETH Zürich, Zürich, Switzerland) and greatly supported by the bachelor thesis of Jonas Enke. Individual contributions are detailed at the beginning of Chapter 3. The content of Chapter 3 has been accepted for publication in *IEEE Transactions on Biomedical Engineering*.

- [51] von Petersdorff-Campen, K.<sup>1st</sup>, Dupuch, M.<sup>1st</sup>, Magkoutas, K., Hierold, C., Meboldt, M., and Schmid Daners, M. (2021). Pressure and Bernoulli-based Flow Measurement via a Tapered Inflow VAD Cannula. *IEEE Transactions on Biomedical Engineering*.

## 2.2 Novel AM process for fully additive-manufactured rotary pump prototype

As shown above, some AM processes already have attained a sufficient level of maturity to be usefully applied in the design, testing, and production of VADs. Other AM methods, especially from the field of 4D or voxel-by-voxel printing, are not yet mature enough. For certain components of VADs, such as electronics or magnets, there are no established AM processes as yet. However, the opportunities such AM processes provide to the VAD field are worth exploring as they motivate further development and application of such processes.

Therefore, this part of the thesis aimed at additively manufacturing a functional VAD prototype in one piece. Most rotary VADs include magnets as part of the bearing or drive system. However, to the au-

### 2.3 Investigation of the applicability of AM parts in functional VAD testing

thor's knowledge, only few publications on additive manufacturing of magnets existed at the time of the study, none of which had demonstrated AM of magnets in a multi-material process. In a first step, a material was developed for the AM of polymer-bonded hard magnets of arbitrary shape by fused deposition modeling (FDM). The material developed was then used in combination with other plastic materials on a multi-material printer to embed magnets into plastic parts directly. Finally, a turbodynamic pump prototype with integrated magnets in the impeller and housing was printed in one piece on a low-cost, end-user 3D printer and was tested with water.

That study is presented in detail in Chapter 4 and was published in *Applied Sciences* [52]. It was greatly supported by the semester thesis of Yannick Hauswirth.

- [52] von Petersdorff-Campen, K., Hauswirth, Y., Carpenter, J., Hagmann, A., Boës, S., Schmid Daners, M., Penner, D. and Meboldt, M. (2018). 3D printing of functional assemblies with integrated polymer-bonded magnets demonstrated with a prototype of a rotary blood pump. *Applied Sciences*, 8(8), 1275.

## 2.3 Investigation of the applicability of AM parts in functional VAD testing

As discussed in Section 1.2, pump design is essential for (1) improving hemocompatibility, (2) increasing efficiency for extended battery life in future fully implantable systems, and (3) enabling compliance with varying flows and pressures in future adaptive VADs. AM has the potential to help meeting this variety of design objectives not only as it allows to manufacture highly optimized and complex geometries, but also by providing prototypes for functional testing at low cost and in short lead times. Such manufacturing-oriented use of AM can enable more frequent design iterations, which ultimately promotes design optimization and reduces the likelihood of failure in later stages of development.

## 2 Summary of scientific contribution

Polymer-based AM techniques are already being used sporadically in VAD development. However, the use of AM parts in functional testing is limited due to concerns that a lack of manufacturing quality of AM parts would affect the functioning of parts and the results of tests. One such concern in particular arises when the testing involves blood where disadvantageous flow fields caused by geometric inaccuracies and low surface quality could induce additional blood damage. To extend the applicability of AM parts beyond early prototyping to functional validation methods and later development phases, the potential influence of the manufacturing method on the test results must be investigated.

A study was conducted to compare four commonly used AM processes for polymers with respect to manufacturing accuracy, surface roughness, and shape fidelity in an aqueous environment. Impeller replicas of the CentriMag blood pump were manufactured with each AM process and integrated into original pump housings. The assemblies then were tested for hydraulic properties and hemolysis and compared to the commercially available pump. Computational fluid dynamic simulations were carried out to support the transfer of the results to other applications.

The study is presented in detail in Chapter 5. It was conducted in collaboration with Jonas Abeken (The Interface Group, Institute of Physiology, University of Zürich, Zürich, Switzerland) and greatly supported by the master thesis of Florian Mauz as well as students of the Seminar of Statistics, ETH Zürich (Stanimir Ivanov, Foong Wen Hao, Reto Zihlmann). Individual contributions are detailed at the beginning of Chapter 5. The content of Chapter 5 was published in the *ASAIO Journal* [53].

- [53] von Petersdorff-Campen, K., Abeken, J., De Zélicourt, D., Kurtcuoglu, V., Meboldt, M., and Schmid Daners, M. (2021). *In Vitro* Testing and Comparison of Additively Manufactured Polymer Impellers for the CentriMag Blood Pump. *ASAIO Journal* Vol. 67 No. 3.

## 2.4 Improving methods for *in vitro* testing of blood damage

While AM processes can address the bottleneck of prototype production, they cannot address bottlenecks of test execution. However, the prototyping capabilities of AM can only be useful for improving and accelerating the development process of VADs if the tests performed on these prototypes allow for similarly high throughput.

For the *in vitro* validation of VADs, hemolysis tests are of particular importance as they provide valuable information on the hemocompatibility of prototypes and thus help reduce the number of animal experiments required. Hemolysis testing plays an important role as a research and development tool for relative comparisons of designs and devices and for predicting clinical outcomes. At the same time, hemolysis testing is associated with significant challenges, including the difficulty of obtaining blood, the high experimental workload, and the low reproducibility of test results. These challenges and several potential approaches to overcome them are described in Chapter 6 and was published in the *ASAIO Journal*.

- [54] von Petersdorff-Campen, K., Schmid Daners (2021). Hemolysis testing *in vitro*: A review of challenges and potential improvements. *ASAIO Journal (online first)*.

The approaches proposed included the use of novel sensor technology for the continuous assessment of hemolysis levels, the use of shear-sensitive fluids as standardizable alternatives to blood, and a thorough investigation of the sources of poor reproducibility. The latter was pursued in a further study to improve operating procedures followed in the Zurich Heart blood laboratory and to enable a more reproducible hemocompatibility testing of VADs and other blood-contacting devices in the future.

A hemolysis study with blood from 23 bovine donors was combined with a comprehensive blood analysis, including cell count, plasma composition, and viscosity, to identify factors for the variability in test results and strategies for its mitigation. The effects of three modifications to the standard protocol were investigated, namely the addition

## 2 Summary of scientific contribution

of 0.1 wt.% bovine serum albumin, maintaining glucose concentration, and replacing plasma by a plasma-like buffer.

The study is presented in detail in Chapter 7. It was greatly supported by the bachelor theses of Seraina Saurenmann and Rick Saner. The content of Chapter 7 was published in the *ASAIO Journal*.

- [55] von Petersdorff-Campen, K., Fischer, P., Bogdanova, A., Schmid Daners, M. (2021). Potential factors for poor reproducibility of *in vitro* hemolysis testing. *ASAIO Journal* (*online first*).



# 3 Pressure and Bernoulli-based flow measurement via a tapered inflow VAD cannula

The content of this chapter has been accepted for publication in *IEEE Transactions on biomedical engineering* [51]. The project was conducted in collaboration with Matthias Dupuch (Laboratory for Micro- and Nanosystems, Department of Mechanical and Process Engineering, ETH Zürich, Zürich, Switzerland) and greatly supported by the bachelor thesis of Jonas Enke. The author's contribution to this project was the development of the dual-sensor concept, the characterization of the cannulas under different static and dynamic pressure and flow conditions as well as the data analysis for these experiments. Matthias Dupuch and Jonas Enke transferred the concept to additive manufactured cannulas and developed and conducted all manufacturing steps leading to functional cannula prototypes.

## 3.1 Introduction

The treatment of end-stage heart failure by using continuous flow ventricular assist devices (VADs) has become prevalent over the last decades [22, 56]. In this time, VAD technology has tremendously evolved, allowing for more robust devices that can be used not only as bridge-to-transplantation, but also as destination therapy [12]. Despite this progress, the limits for VAD improvement should be further challenged since heart failure therapy with VADs is still associated with adverse events that either reduce the survival rates, or affect the quality of life of the patients [57]. The majority of these events pertaining to VAD therapy are related to the continuous flow of the VADs that are currently in clinical use. More precisely, the preset speed op-

### 3 Pressure and flow measurement with inflow cannula

eration of the VADs does not allow adaptation of the pump flow to the momentary needs of the body, often resulting in critical conditions such as under- and over pumping causing congestion or ventricular wall collapse, known as ventricular suction, respectively [12, 58, 59].

To alleviate the adverse events, various efforts have been undertaken by different groups to develop physiological control schemes that allow the adjustment of the pump speed to the perfusion needs of the patients. Those control schemes are based on the intrinsic pump signals, such as the pump current and the pump speed, or various hemodynamic signals, such as the left ventricular pressure (LVP) [60–62], the left ventricular volume [63], the heartrate [64, 65], and the aortic pressure (AoP) [66, 67].

Prerequisite for all physiological controllers is the input from either a measured or an estimated signal. However, the only currently available, clinically approved, and implantable pressure sensor is the CardioMEMS (Abbot, Chicago, USA) for implantation in the pulmonary artery. Its use improved the patient outcome and reduced readmission via improved medication control in VAD patients [68]. The passive nature of this sensor makes the system reliant on a large extracorporeal readout station, allowing for periodical measurements only. In an attempt to overcome the lack of clinically available long-term implantable sensor technology, sensorless/non-invasive estimation algorithms have been developed. Frequently, those estimators based on pump speed, current, and/or power, aim to indirectly derive the pump flow [69, 70] and the pump pressure head [71]. Although pump flow provides useful insights about the interaction of the pump with the cardiovascular system, a better understanding can be achieved when the total cardiac output (CO) is known. In this regard, Rüschen et al. [72] developed a method that uses the measured AoP and LVP to estimate the CO, however, the need for two-sensors in different, remote positions, significantly limits the usage of the approach in a clinical setting. Recently, Petrou et al. [73] developed an algorithm to estimate the CO by utilizing only a pump inlet pressure (PIP) sensor and the intrinsic signals of the VAD, resulting in higher accuracy and less system complexity than the one presented in [72].

For PIP measurement in VADs, several active sensing approaches have been explored that use the energy available to drive the VAD

to continuously collect pressure data. All use measurement interfaces that are integrated into the wall of the perfused structure and are therefore parallel to the flow. As such, they measure static pressure and are therefore flow dependent, since static pressure varies with flow at constant total pressure according to the Bernoulli equation.

One category uses the measurement of deformation (strain) of the inflow cannula (IC). Such approaches are either based on local thinning of the cannula wall to the point where physiological pressures result in detectable deformation [74, 75] or replacement of the IC wall with a softer material and detection of its deformation via an implemented optical fiber and Bragg-grating [76]. Another category consists of approaches where the pressure transmission membrane of a compliantly encapsulated sensor is placed in a cut out of the IC's wall [77–79]. Alternatively, a patterned membrane for Fabry-Pérot interferometry has been used [80].

A hybrid approach was investigated by Staufert et al. [28] where the sensing interface is formed by a seamless parylene coating of the inner cannula surface that is suspended over an oil-filled cavity in the cannula wall hosting the pressure sensor. This combines the potential for low drift and high accuracy of the compliant encapsulation with the smooth interface of the cannula deformation approaches, while the use of parylene ensures good hemocompatibility and a biostable barrier for the pressure transmission oil. Durable adhesion of the coating to the substrate under simulated physiological conditions was achieved by a newly developed nanostructure treatment of the substrate.

In this work, we present the compact integration of a two-position pressure sensing system into the conical inlet cannula for a HeartMate 3 (HM3) (Abbott, Abbott Park, IL, USA), based on the hybrid integration approach by Staufert et al. [28]. By implementing two sensing sites at locations with different cannula cross-sections and therefore different local flow velocities, we can determine the flow-independent LVP and the pump flow rate based on the difference of the two sensor readings. This method allows the continuous and accurate measurement of pressure and flow waveforms and enables the acquisition of the critical systolic, diastolic, and mean LVPs. The performance of the proposed integration and the developed model was validated

under physiological conditions using a hybrid mock circulation setup (HMC) [81].

## 3.2 Material and methods

### 3.2.1 Inflow cannula design

This work's design of the cannula that allows the integration of pressure sensors is based on the original tapered cannula of the HM3. All added elements and sensor components are integrated into the 3D printed cannula wall to maintain the flow path of the original device, as well as the compatibility with the pump body and the suturing ring. The placement of the sensing interfaces on the inner wall of the IC aims at preventing damage during implantation and tissue overgrowth by the myocardium after implantation. The sensing sites are placed at different positions along the axis of the cannula (Figure 3.1) to allow for the measurement of  $Q$  and  $P_{tot}$ . The sensors are placed at the bottom of the IC, where the IC's wall is thicker and permits embedding. The smaller diameter sensor (SDS) is placed right behind the sensing interface. For the larger diameter sensors (LDS), a small channel, embedded in the IC's wall and filled with a pressure transmission fluid connects the sensor and the sensing interface. This channel is also connected to the filling port. A similar design was chosen for the SDS (Figure 3.1a). All materials used are either suitable for implantation or adequately encapsulated.

### 3.2.2 Inflow cannula production

A detailed description of the IC production can be found in Appendix B. In short, the IC blanks were produced by selective laser melting to realize the integrated channels for pressure transmission and machine finished. A layer of nanostructures was grown on the surface of the 3D printed IC (Figure 3.2a) to later mechanically anchor the parylene film, as described in detail in [39]. The nanostructures in the membrane bed were etched away to enable the parylene film to delaminate after its deposition. For this, a photolithography step was utilized (Figure 3.2b). The ICs were dip coated in photoresist and the

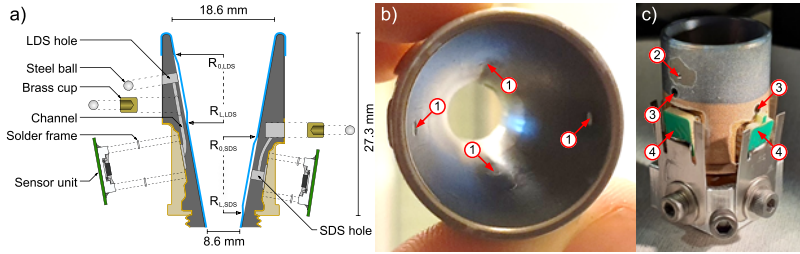


**Figure 3.1:** a) Design of two pressure sensors integrated into the inflow cannula for the HM3. b) Inner wall of the inflow cannula with membranes and access channels (1). c) Cannula during the assembly process with the closed large diameter sensor (2), the open filling port holes for the brass cups (3), and the sensor units (4) fixed by clamps for soldering. SDS, small diameter sensor.

membrane bed area was illuminated using a  $45^\circ$  mirror and a polyimide mask, before etching the exposed nanostructures. A metal layer was evaporated onto the sensor sockets for a later solder-bonding step (Figure 3.2c). The parylene film was evaporated onto the ICs after filling the access-channels with a sacrificial, compressed powder sugar plug (Figure 3.2d). Then the pressure sensor (LPS22HB, STMicroelectronics, Geneva, Switzerland) units were soldered into their sockets (Figure 3.2e) and the filling ports sealed after filling the cavities with the pressure transmission oil (Bluesil FLD 47 V100, Elkem AS, Oslo, Norway, Figure 3.2f).

### 3.2.3 Analytical model for LVP and flow rate estimation

A mathematical model, describing the relation between the flow rate and the measured pressure at two different locations inside a conical cannula has been developed in this study. The flow patterns that develop within the left ventricle (LV) differ from those inside the IC of an implanted VAD, where the reduced flow cross-sectional area and the more confined flow result in increased flow velocities [82]. Assuming laminar, inviscid, and incompressible flow, the total pressure in the LV and in the cannula is equal. Therefore, higher flow velocities in the cannula translate to higher dynamic pressures  $p_{dynamic}$  and lower

### 3 Pressure and flow measurement with inflow cannula

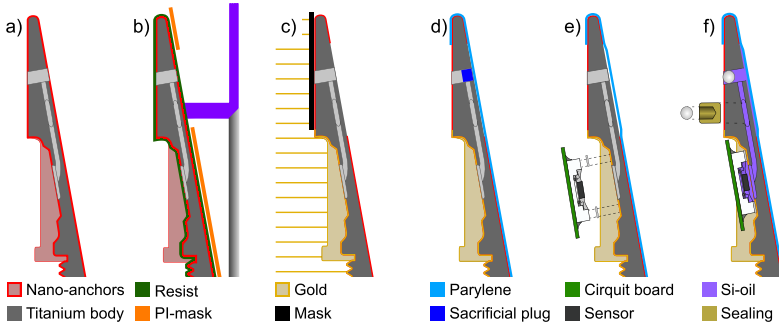


**Figure 3.2:** a) Inflow cannula (IC) surface is nanostructured (red). b) Photoresist (green) is illuminated by reflecting UV-light (purple) onto unmasked areas (orange mask) for later etching the nanostructures in the exposed area. c) Outer IC wall is metalized (gold). d) Parylene (teal) is deposited after filling the sensing hole with sacrificial sugar (blue). e) Membrane is released and sensor unit is soldered to the surface (black sensor). f) The cavity is filled with oil (purple) and sealed with the cup and ball.

static pressures  $p_{static}$  in the cannula than in the LV according to Bernoulli's equation 3.1,

$$p_{total} = p_{static} + p_{dynamic} = p_{static} + \frac{1}{2}\rho v^2 \quad (3.1)$$

, with the total pressure  $p_{total}$ , the density  $\rho$  and the flow velocity  $v$ .

A pressure-sensing interface that is integrated into the surface of the IC's inner wall (Figure 3.1) and that is therefore oriented parallel to the streamlines of the flow, measures only the static pressure component. Based on Equation 3.1, due to the flow through the VAD, the static pressure measured by such an integrated sensor will be lower than the medically relevant left ventricular pressure. Since the sensing interfaces are of finite dimensions along the flow direction, the flow velocity exerting across the sensing interface is not constant. Hence, the transmitted pressure, recorded by the encapsulated sensor, corresponds to the average static pressure acting along the sensing interface. Assuming that the pressure is constant along the circumferen-

tial dimension of the sensing interface, the transmitted static pressure  $p_{static,trans}$  averaged along the sensing surface is given by:

$$\begin{aligned} p_{static,trans} &= \frac{1}{L} \cdot \int_0^L p_{static}(z) dz \\ &= \frac{1}{L} \int_0^L (p_{total} - p_{dynamic}(z)) dz \end{aligned} \quad (3.2)$$

with  $L$  being the axial length of the sensing interface and  $z$  a distance in the direction of flow. The dynamic pressure  $p_{dynamic}$  can be expressed as a function of flow rate  $Q$

$$\begin{aligned} p_{dynamic} &= \frac{\rho}{2} \cdot v^2 \\ &= \frac{\rho}{2} \cdot \left( \frac{Q}{A(z)} \right)^2 \\ &= \frac{\rho \cdot Q^2}{2 \cdot \pi^2} \cdot \frac{1}{R(z)^4} \\ &:= \frac{a \cdot Q^2}{R(z)^4} \end{aligned} \quad (3.3)$$

, with the local cross-sectional area  $A$ , the local cannula radius  $R$  and a density-dependent constant  $a$ . The integration of Equation 3.2 after replacing  $p_{dynamic}$  according to Equation 3.3, and substituting  $R$  using the cannula taper function along the membrane

$$R(z) = \frac{R_L - R_0}{L} \cdot z \quad (3.4)$$

, where  $R_0$  and  $R_L$  are the inner radii of the cannula at the beginning and the end of the individual sensing interface and its derivative  $m$

$$m := \frac{dR(z)}{dz} = \frac{R_L - R_0}{L} \quad (3.5)$$

results in

### 3 Pressure and flow measurement with inflow cannula

$$\begin{aligned}
 p_{static,trans} &= \frac{1}{m \cdot L} \int_{R_0}^{R_L} (p_{total} - p_{dynamic}(R)) \, dR \\
 &= p_{total} - \frac{a \cdot Q^2}{3} \cdot c
 \end{aligned} \tag{3.6}$$

with

$$c = \left[ \frac{1}{R_0 - R_L} \left( \frac{1}{R_L^3} - \frac{1}{R_0^3} \right) \right] \tag{3.7}$$

The decrease of the measured pressure is therefore proportional to  $Q$  square. Additionally, the transmitted pressure depends on the constant geometric factor  $c$  of the sensing interface, namely the radii of the cone at the upstream ( $R_0$ ) and downstream ( $R_L$ ) edge of the sensing interface, as well as a density-dependent term  $a = \frac{\rho}{2 \cdot \pi^2}$ . If the exact geometry of the sensing interface is not known, e.g. due to manufacturing inaccuracies, the geometric factor  $c$  can be determined experimentally as described below (SF experiments). Combining measurements of two sensing interfaces placed at different positions inside the conical cannula (large diameter sensor (LDS) and small diameter sensor (SDS), Figure 3.1a) and assuming a negligible total pressure loss between the two measurement points, allows to deduce both the flow rate and total pressure  $p_{total}$  using Equations 3.8 and 3.9.

$$Q = \sqrt{\frac{3 \cdot (p_{static,trans,LDS} - p_{static,trans,SDS})}{a \cdot (c_{SDS} - c_{LDS})}} \tag{3.8}$$

$$\begin{aligned}
 p_{total} &= p_{static,trans,LDS} \\
 &+ \frac{p_{static,trans,LDS} - p_{static,trans,SDS}}{c_{SDS} - c_{LDS}} \cdot c_{LDS}
 \end{aligned} \tag{3.9}$$

The presented mathematical model requires experimental validation as it is based on two assumptions, which do not hold under real conditions. The first assumption is the validity of Bernoulli's principle, which in theory is only valid for inviscid fluids and along streamlines of laminar flow. However, all fluids relevant to this application have a



non-zero viscosity and the conditions for laminar flow are violated at elevated flow rates. The second assumption is the absence of frictional losses, which is not given in a real system. However, the effect of a violation in the presented application is assumed to be small compared to the flow-induced pressure changes of interest.

### 3.2.4 In vitro testing of the cannula prototypes

To assess the temperature cross-sensitivity (TCS) of each sensor capsule, the ICs were exposed to temperature cycles from 35 °C to 42 °C (Figure 3.3a) in a climate chamber (VCL 4006, Vötsch Industrietechnik, Balingen, Germany). Ambient pressure fluctuations were recorded with an additional unencapsulated pressure sensor and subtracted from the IC's pressure data. The temperature data was acquired individually for each sensor capsule with the integrated temperature module of the pressure sensor.

To test the performance of the assembled prototypes under static and dynamic pressure and flow conditions, a previously presented hybrid mock circulation setup (HMC) [81] was used. The full setup is shown in Figure 3.4. The HMC consisted of two pressure-controlled fluid reservoirs that emulated LVP (inflow reservoir (IR)) and AoP (outflow reservoir (OR)), respectively. The ICs were screwed onto a HM3 pump body (original IC previously removed) and mounted to the IR using a tubular connector. The outlet of the HM3 pump was connected to the OR with PVC tubing (200 mm length, 10 mm inner diameter). The fluid level in the reservoirs was controlled by a bidirectional pump (Water Puppy, Xylem Jabsco, Hoddesdon, UK) serving as a backflow connection between the reservoirs. The temperature of the working fluid (50.8 wt.% glycerol in water) was adjusted to  $37 \pm 1$  °C providing a viscosity of  $3.5 \pm 1$  mPa and a density of  $1.12$  g/cm<sup>3</sup>. The flow rate through the cannulas was measured at the tube between the HM3 pump and OR with a clamp-on flow probe (TS410/ME-11PXL, Transonic Systems, Ithaca, NY, USA). Reference pressure measurements for the emulated ventricular total pressure, were obtained at the bottom of each reservoir (PN2009, IFM Electronic GmbH, Essen, Germany). The head pressure was defined as the pressure difference

### 3 Pressure and flow measurement with inflow cannula

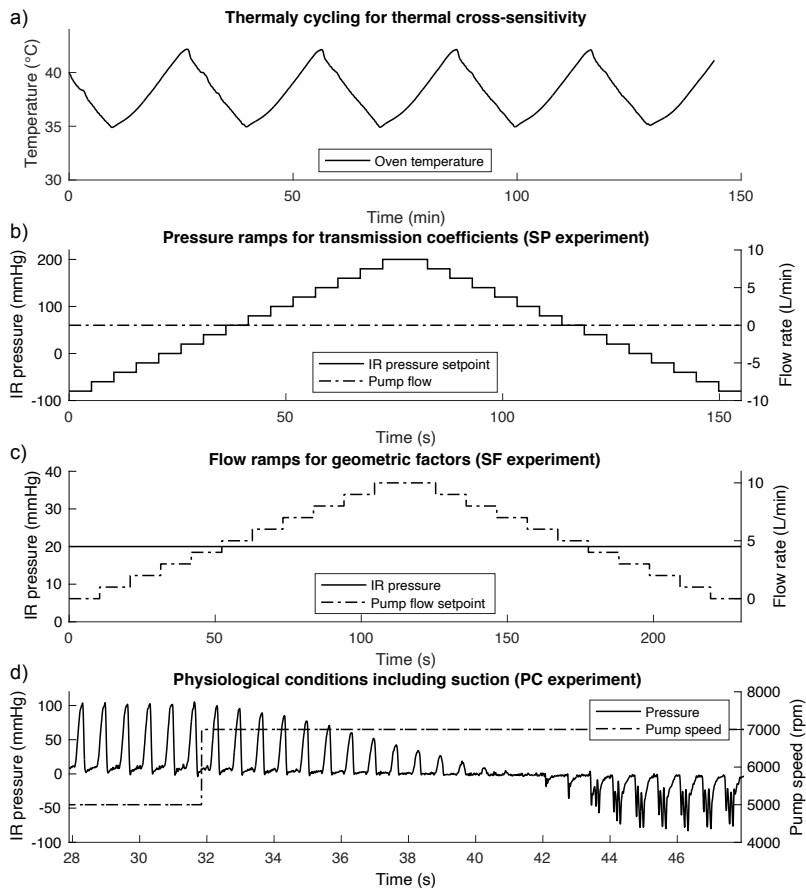


**Figure 3.3:** a) Temperature cycling for determination of the temperature cross sensitivity (TCS), b) Static pressure testing, without flow through the pump, c) Static pressure testing, with flow through the pump, d) Testing under realistic physiological conditions with triggering of a suction event (negative pressures) by increasing pump speed.

between the IR and OR. The sampling rate of the test bench sensors was 1 kHz. The IC pressure sensors were sampled with 200 Hz.

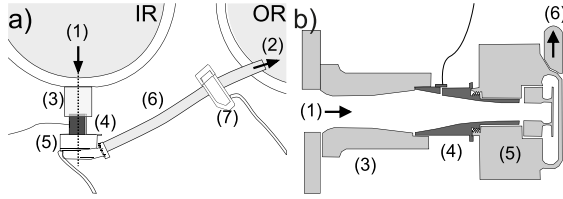


**Figure 3.4:** a) Hybrid mock circulation setup with the inflow reservoir (IR) (1), the outflow reservoir (OR) (2), the tubular connector with outlet to the inlet reference pressure sensor (3), the pressure sensor integrated inflow cannula (4), the HM3 pump (5), the outflow graft (6) and the flow sensor (7). The dashed line in subfigure a) represents the sectional view of subfigure b). The arrows represent the flow direction.

The prototypes were tested in three sets of experiments.

Static pressure testing, without flow through the pump (SP experiment), was performed to assess pressure transmission curves for correction of subsequent measurements. For these experiments, only the IR pressure was controlled. A staircase pressure profile was applied to the IR with increments of 20 mmHg in a range of  $-100$  and 200 mmHg (Figure 3.3b). Each pressure level was held for 5 s to achieve stationary conditions. For each pressure level, the mid 3 s were used to calculate an average value. The pressure-dependent difference of the IC pressure sensors to the reference was approximated as linear. Cannula sensors that showed drift in this experiment were excluded from further analysis.

Static pressure testing, with flow through the pump (SF experiment), was performed to test the proposed analytical model and to assess the geometric factors  $c$  according to Equation 3.6 to estimate the flow rate and the total pressure from the measured static pressure according to Equation 3.8 and 3.9, respectively. For those experiments, a flow rate staircase profile was applied with increments of approximately 1 L/min between 0 to 10 L/min by changing the pump speed of the HM3 pump from 5300 to 9000 rpm (Figure 3.3c). The IR and OR pressures were set to 20 mmHg and 120 mmHg, respectively, to create a pressure head of 100 mmHg. Each flow level was held for 10 s to achieve stationary conditions. The sensor signals were corrected according to the individual pressure transmission curve determined in

### 3 Pressure and flow measurement with inflow cannula

the SP measurement. For each flow level the mid 5 s were used to calculate an average value.

Finally, the prototypes were tested under realistic physiological conditions (PC experiment) to assess their ability to provide accurate data quality both for patient monitoring and VAD control purposes. For this experiment, the HMC was used following the hardware-in-the-loop approach proposed by Ochsner et al. [81]. Specifically, the cardiovascular system was emulated in real time based on the model proposed by Colacino et al. [83]. The flow measured at the outlet of the HM3 pump was fed back to the numerical simulation and the LVP and AoP calculated from the model were pneumatically applied to the IR and OR, respectively. Hence, a realistic interaction of the pump with the cardiovascular system could be achieved. A pathological scenario was emulated for the heart by setting the heart rate at 90 bpm and the LV contractility at 34% (analogous to [43]) The HM3 pump speed was first set to 5300 rpm such that an average flow rate of approximately 5 L/min was achieved. As a next step, the HM3 pump speed was increased to 7300 rpm to trigger over-pumping and consequently suction events.

## 3.3 Results

### 3.3.1 Individual sensor capsule characteristics

The TCS extracted from the temperature cycling experiment is shown in Figure 3.5 in relation to the measured area of the membrane. The LDSs of all three cannulas showed higher TCS coefficients than the SDSs. The theoretically expected TCS (see Appendix B), calculated based on the observed delaminated area is also shown in Figure 3.5. The TCS ranges from 0.9 mmHg/K to 3.3 mmHg/K. A lower area, in general, equals a higher TCS. However, the length to width ratio of the membrane also affects the expected TCS. This can result in a membrane with a smaller area to have a higher TCS coefficient than a membrane with a larger area as can be seen in the case of LDS B/A.

The deviation between the static pressure recorded by three cannulas on the HMC is given in Figure 3.6. With one exception, all sensor capsules showed pressure transfer with an error smaller than 2 mmHg

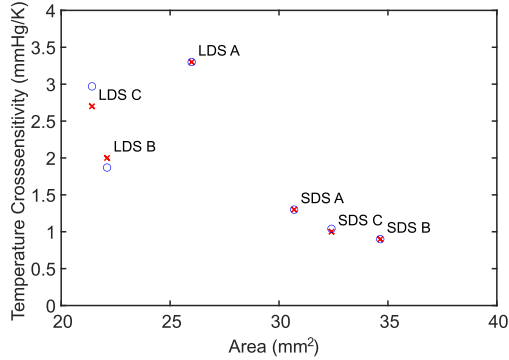


**Figure 3.5:** Measured (x) and calculated (o) linear temperature coefficients of the small diameter sensor (SDS) and large diameter sensor (LDS) capsules in cannulas A, B and C.

in the range from  $-100$  mmHg to  $200$  mmHg, corresponding to an error of less than 1%. The sensor capsule SDS B showed a decreasing pressure transmission with increasing applied pressures, with the largest observed overall error corresponding to  $-0.03$  mmHg/mmHg. The deviation shows a slight nonlinearity with an increase towards higher pressures. A linear regression derived from this data, individually for each sensor capsule, was used to correct the other measurements.

### 3.3.2 Determination of geometric factors

The relation of measured pressure and flow rate for the IC sensors is shown in Figure 3.7, where data from one LDS and one SDS integrated in cannulas A, B and C are provided. All sensors showed a square relationship between flow rate and measured pressure at constant total pressure ( $R^2$  larger than 0.95). At a flow rate of  $10$  L/min, the LDSs and SDSs showed a decrease in measured pressure of up to  $5$  mmHg and  $15$  mmHg, respectively. Accordingly, the geometric factors  $c$  determined as the fitting parameters of the experimental data according to Equation 3.8 ranged between  $12.9$  cm<sup>-4</sup> –  $14.3$  cm<sup>-4</sup> for the  $c_{LDS}$  and  $34.0$  cm<sup>-4</sup> –  $43.68$  cm<sup>-4</sup> for the  $c_{SDS}$ . The geometric factors  $c$

### 3 Pressure and flow measurement with inflow cannula

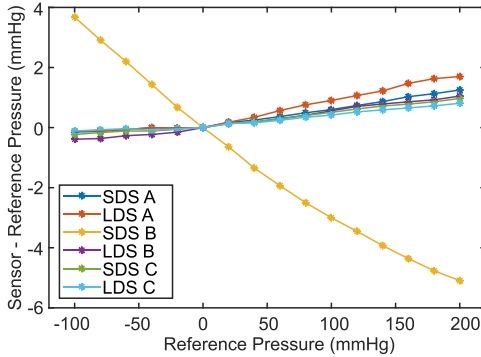


**Figure 3.6:** Pressure deviation between each capsule and the reference sensor at applied pressures between  $-100$  mmHg and  $200$  mmHg. Large diameter sensor, (LDS); Small diameter sensor (SDS); A-C, three cannulas tested.

determined from measured membrane dimensions using Equation 3.7 followed the same trend (Figure 3.7) but were smaller than the experimentally determined factors.

#### 3.3.3 Calculation of flow rate and total pressure under physiological conditions

Figure 3.8 provides a comparison of the measured flow rate to the flow rate calculated using Equation 3.8 from testing under physiological conditions (PC testing). Figure 3.8a shows a section of the PC experiment at the onset of ventricular suction, which was provoked by increasing the pump speed of the HM3 to a level unsuitable for the emulated patient. The increase in pump speed led to an increase in intra-cannula flow by about  $3$  L/min. The resulting emulated depletion of the LV eventually was followed by sudden drops in flow, emulating a collapse of the LV walls. Figure 3.8b shows one cardiac cycle during normal operation without suction. The calculated flow rate appears to be less precise during diastole than during systole. Figure 3.8c shows the accuracy of the calculated flow rate for cannulas A, B and C. The accuracy was determined as the deviation of

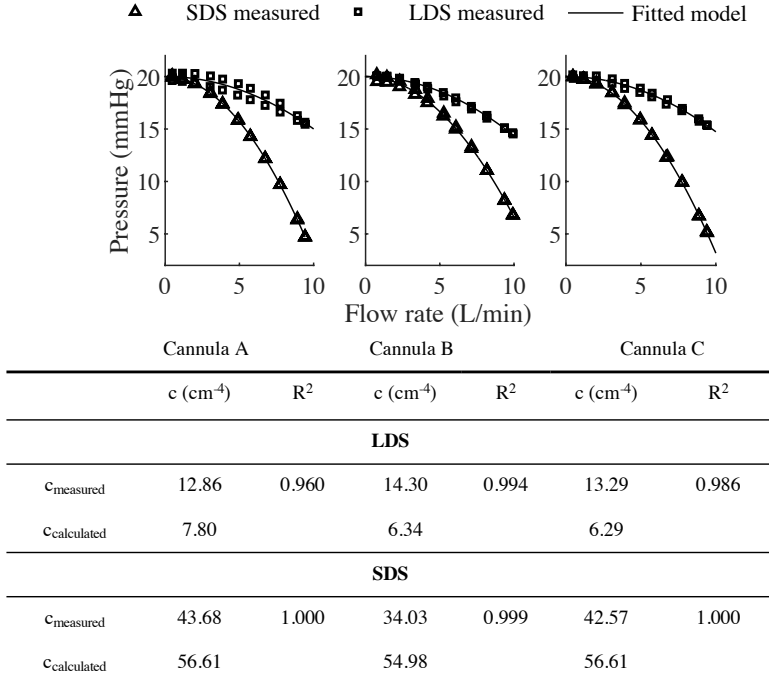


**Figure 3.7:** Pressure measured by large and small diameter sensors (SF experiment) at a total pressure of 20 mmHg and varying flow rates. The geometric parameters  $c_{\text{measured}}$  were determined from the measurements as the fitting parameters of proposed model  $P_{\text{stat}} = f(c_{\text{measured}} \cdot Q_2)$  (Equation 3.6). The model had high explanatory power ( $R^2$  larger than 0.95). For comparison, the geometric factors were additionally calculated from measured membrane dimensions ( $c_{\text{calculated}}$ ).

calculated from the reference cardiac cycle averaged flow rate values. A mean deviation of less than 0.2 L/min was achieved with all cannulas, whereby accuracies of  $-0.14 \pm 0.04$  L/min,  $0.19 \pm 0.12$  L/min and  $0.02 \pm 0.10$  L/min were achieved with cannulas A, B and C, respectively.

Figure 3.9 provides a comparison of the pressures measured by the LDS and SDS to the total pressure calculated using Equation 3.9 dur-

### 3 Pressure and flow measurement with inflow cannula

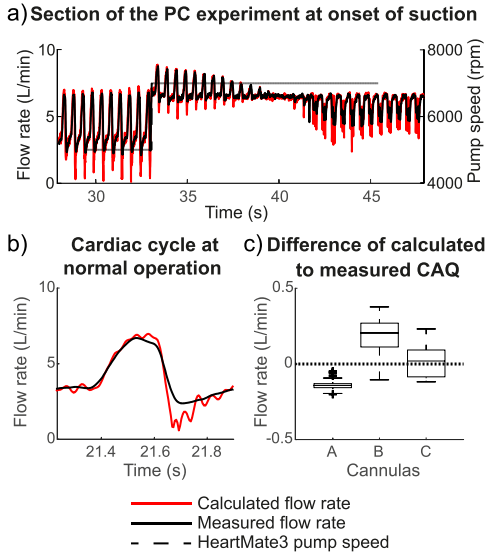


**Figure 3.8:** Example of measured and calculated flow rate acquired at the onset of suction (a) and for one cardiac cycle during non-suction operation (b) with cannula A. The calculated flow rate was determined according to Equation 3.8 using the small diameter sensor (SDS) and large diameter sensor (LDS) readings.

ing the PC experiment. Figure 3.9a shows the section of the PR experiment at the onset of suction. The collapse of the LV during suction was emulated by the HMC as spikes of negative pressure. During the varying conditions emulated in the PC experiment, as it is shown in Figure 3.9a, both sensors provide highly accurate pressure measurements. In the same subfigure, it can be seen that the pressure difference between the LDS and SDS (grey area) depended noticeably on the flow rate. For example, the LDS-SDS difference increased overall with an increase in mean flow through the cannula due to the increase from 5000 rpm to 7000 rpm. Likewise, the LDS-SDS difference changed within each cardiac cycle, showing larger values during systole due to an increase in flow rate compared to diastole.



Figure 3.9b illustrates one cardiac cycle during normal operation of the cardiovascular system and the VAD, without suction events. The pressure measured by the SDS was below the pressure measured by the LDS at high flow rates during systole. At lower flow rates during diastole this difference was noticeably smaller. Additionally, the ESP, EDP and the SSL window that were determined separately for each pressure profile are displayed.

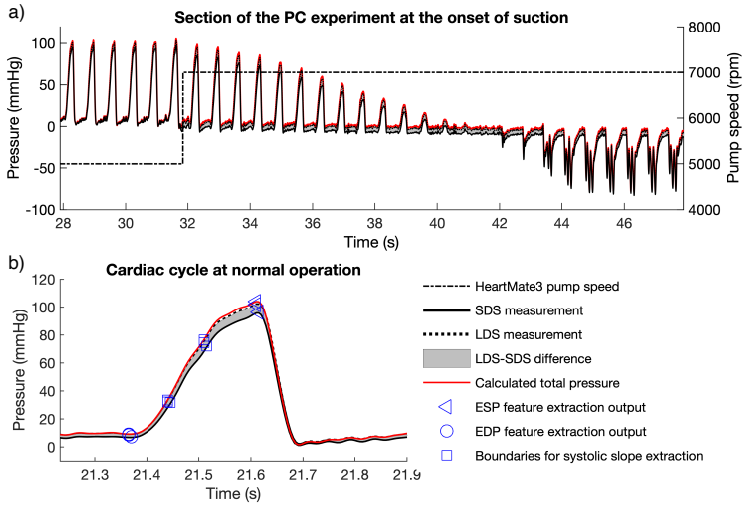


**Figure 3.9:** Example of static pressure measured by the small diameter sensor (SDS) and large diameter sensor (LDS) as well as total pressure calculated from the SDS and LDS readings shown for a section of the PC testing at the onset of suction (a) and for one cardiac cycle during non-suction operation (b) with cannula A. The calculated total pressure was determined according to Equation 3.8 using the SDS and LDS readings and the previously determined geometric factors  $c$ .

Figure 3.10a-d show the accuracy of the calculated total pressure for the CAP, ESP, EDP and SSL features for cannulas A, B and C. Additionally, Figure 3.10a-d show the accuracy of features extracted from the pressure curves measured by the LDS and SDS. The accuracy was determined as the deviation to the features extracted from the reference pressure sensor in the IR. For all pressure features, the

### 3 Pressure and flow measurement with inflow cannula

calculated total pressure provided a closer representation of the reference pressure than the SDS or LDS measurements. This is especially true for the ESP feature, where high flow rates at the end-diastole introduced a larger drop in measured pressure than at the EDP feature. Here the reference pressure was represented with a 7- and 25-times higher accuracy by the calculated total pressure compared to the LDS and SDS measurements, respectively. The mean deviation of the calculated total pressure to the reference ranged from  $-0.3 \pm 0.2$  mmHg to  $-0.1 \pm 0.1$  mmHg for the CAP, from  $-0.3 \pm 0.6$  mmHg to  $-0.2 \pm 0.9$  mmHg at the ESP feature, from  $-0.3 \pm 1.0$  mmHg to  $0.0 \pm 0.5$  mmHg at the EDP feature and from  $-7.2 \pm 19.2$  mmHg/s to  $-0.1 \pm 25.4$  mmHg/s in SSL. In comparison, the mean deviation of the SDS features from the reference ranged from  $-3.6 \pm 0.1$  mmHg to  $-3.1 \pm 0.1$  mmHg for the CAP, from  $-7.6 \pm 0.4$  mmHg to  $-6.1 \pm 1.0$  mmHg at the ESP feature, from  $-2.0 \pm 0.7$  mmHg to  $-1.1 \pm 2.3$  mmHg at the EDP feature and from  $-54.1 \pm 20.4$  mmHg/s to  $-44.4 \pm 24.7$  mmHg/s in SSL. As such the mean deviations of the SDS features were about three time larger than those of the LDS features.

## 3.4 Discussion

### 3.4.1 Manufacturing and calibration

The pressure transmission error was found to be low for all but one sensor capsule. For this sensor capsule, there could be several possible causes provoking its inferior behavior such as a small active membrane area, miscalibration, or supply power issues. However, since the temperature cross sensitivity of that sensor capsule was within the expected values, an issue with the active membrane area can be excluded. The good pressure transmission of the LDSs validates the embedded elongated pressure transmission channels as a tool to measure pressure in areas otherwise inaccessible to the pressure sensor.

The temperature cross sensitivity was higher than desired for all sensor capsules, especially for the LDSs. This is attributed to the incomplete delamination of the membranes. This assumption is supported by the matching of the measured TCSs with the theoretical

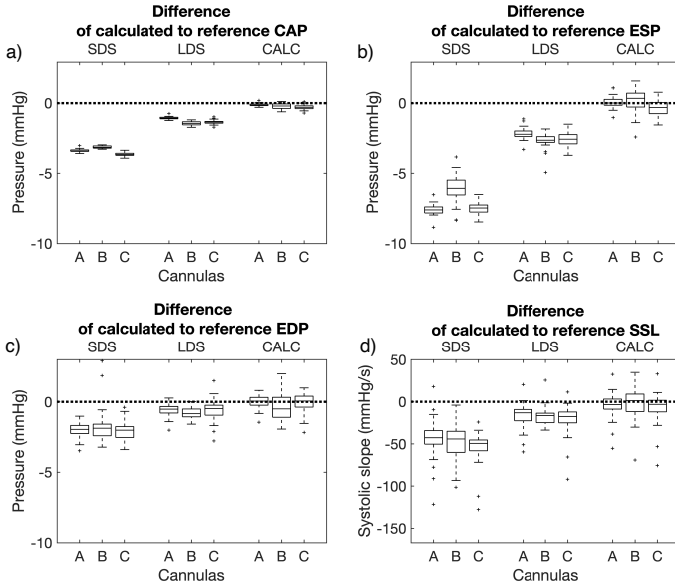


**Figure 3.10:** The differences between the measured and calculated features were extracted from the calculated total pressure and the SDS and LDS measurements during non-suction operation. The cardiac cycle averaged pressure (CAP, Subfigure (a)), the end-systolic pressure (ESP, Subfigure (b)), the end-diastolic pressure (EDP, Subfigure (c)) and the systolic slope (SSL, Subfigure (d)) were determined for 30 cardiac cycles.

TCSs, calculated based on the observed delaminated membrane area (Figure 3.3). The partial delamination can be attributed to insufficient etching times and the resulting nanostructure residues in the membrane bed.

The proposed theoretical model for the geometry-dependent square relation between flow rate and measured pressure (Equation 3.6) is supported by the experimental data. The effect of flow rate on the measured pressure was about three times stronger for the SDSs than for the LDSs thereby enabling the determination of total pressure and flow rate from the difference between SDSs and LDSs measurements. However, the effect of flow rate was stronger for the LDSs and

### 3 Pressure and flow measurement with inflow cannula

weaker for the SDSs than expected from the geometric dimensions of the membranes. This suggests that the conditions accounting for the Bernoulli's principle are partially violated, so that additional effects not covered by the proposed model come into play.

#### 3.4.2 Signal to noise ratio

The signal-to-noise ratio (SNR) is a characteristic for evaluating the precision of a sensor. In this application, the relevant signal is the pressure difference between the LDS and SDS, while the noise magnitude is approximated with the standard deviation of the signal. The aforementioned pressure difference is dependent on the square of the flow rate, as derived from Equation 3.6 and experimentally confirmed (Figure 3.7). A conservative estimation of 1 mmHg noise level can be made from the standard deviation of the extracted physiological characteristics shown in the boxplots of Figure 3.9. The standard deviation of the extracted ESP and EDP characteristics is about the same in magnitude, however the flow rate at these points differs by about 4 L/min, indicating that the noise is, in a first approximation, independent of the flow rate. Consequently, the signal-to-noise ratio (SNR), following the behavior of the signal, decreases quadratically with decreasing flow rate and is, therefore, less favorable when determining ESP than EDP. A direct consequence of this low SNR at low flow rates is the noise in the calculated flow rate in the low-flow, diastolic regimes, as can be seen in Figure 3.8b ( $t > 21.6$  s). At end-systole ( $t = 21.6$ ), the flow rate is about twice as high, which leads to a fourfold increase in the pressure difference signal and a concomitant fourfold improvement in the SNR. According to Equation 3.8, a measurement using sensing interfaces with geometric factors of  $c_{LDS} = 12\text{cm}^{-4}$  and  $c_{SDS} = 40\text{cm}^{-4}$  and a noise of 1 mmHg would exhibit an SNR of 1 at a flow rate of 3 L/min. This means that with such a design the noise would be greater than the signal at flow rates below 3 L/min, reducing the operating range of the sensor. Hence, the critical flow rate at which the SNR falls below 1 is highly affected by the cannula design. A reduction of this critical flow rate could be achieved by increasing the difference between the geometric factors  $c$  of the IC sensors, e.g. by placing the SDS sensor interface at a location with

an even smaller pipe radius. The theoretical improvement of the SNR is proportional to  $(R_{old}/R_{new})^4$ . The associated critical flow rate is reduced by  $1/(R_{old}/R_{new})^2$ . For example, a 50% reduction of the cannula radius at the location of the SDS would reduce the critical flow rate from 3 L/min to 0.75 L/min.

### 3.4.3 Influence of density changes

The method presented for calculating the flow rate necessitates a specification of the density  $\rho$  of the flowing medium (according to Equation 3.8:  $Q = f(\sqrt{1/\rho})$ ). The dominant factor for the density of blood is the hematocrit. Even with extreme changes in hematocrit, the density range of 1040 g/cm<sup>3</sup> – 1060 g/cm<sup>3</sup> is not exceeded [84]. For a significant density change of 10 g/cm<sup>3</sup>, the resulting error of the calculated flow rate would be only 0.5%. Therefore, the effect can be neglected, even if the density of blood of a patient changes, e.g. due to an alteration in hematocrit.

### 3.4.4 Accuracy and applicability

During the in-vitro experiments, the calculated blood flow at the inlet of the pump is in good agreement with the measured flow, resulting in a mean absolute error of  $-0.14 \pm 0.04$  L/min to  $0.19 \pm 0.12$  L/min (Cannula A) that indicates the superiority of the presented approach over existing flow estimators [85, 86]. A fidelity analysis of the calculated flow signal shows the ability to accurately reproduce the real-time waveform of the flow profile, which can considerably advance the monitoring of VAD patients and, hence, improve their treatment. Although the accuracy of the flow estimation reduces in low flow regimes, the accuracy at those regions can be increased by a more appropriate selection of the geometric parameter  $c$ .

When combining the measurements from the two pressure sensor capsules with the mathematical model presented, the calculated total LVP shows excellent agreement with the reference pressure, achieving an approximately zero mean error for the ESP, EDP and CAP. Hence, both the calculated total pressure and the single LDS pressure

### 3 Pressure and flow measurement with inflow cannula

demonstrate an accuracy higher than other existing implantable pressure sensors [87,88], testifying to the ability to be used for monitoring purposes in VAD patients, as well as to provide input parameters that are necessary for the majority of the Starling-like control approaches for VADs [60,61,89]. Additionally, as it can be seen in Figure 3.6, the systolic slope deduced from the pressure waveform of both the LDS signal and the calculated LV pressure shows high agreement with the systolic slope deduced from the reference pressure. The systolic slope can be considered as an important indicator of the remaining contractility of the heart [90], and therefore, accurate extraction of the systolic slope could facilitate a better planning of the treatment and allow for adaptive control approaches. The pressure difference between the LDS and IR remains below 3 mmHg even under high flow during end-systole. This would allow the system to remain operative even after SDS failure, albeit with limited precision.

#### 3.4.5 Conclusion and future work

In this study, a concept for determining the total pressure (i.e. the LVP) and blood flow rate through the VAD, based on two pressure sensors in the VAD's IC was developed. The feasibility of the concept was demonstrated with three prototype ICs compatible with the commercial blood pump HM3 and the viability of the model was verified under simulated physiological pressure and flow conditions. The presented Bernoulli-based calculation of the LVP achieved a deviation from the reference pressure of only 0.6 mmHg compared to 7 mmHg (SDS) and 2.5 mmHg (LDS) when directly using the measured pressure as an approximation of the LVP for the highly flow affected ESP feature. Further, the two-sensor capsule configuration enabled the measurement of the blood flow rate through the VAD with an accuracy better than  $\pm 0.3$  L/min for a cardiac cycle averaged flow rate. Limitations to the flow measurement are the SNR at low flow rates. Maximizing the axial separation of the two sensing sites, and therefore the cannula radius difference, between the LDS and SDS is expected to significantly improve the SNR at these low flow rates. In future works, the long-term stability of the system must be assessed in-vitro

### 3.4 Discussion

and in-vivo. Currently, efforts are being made to implement the sensor system with a control scheme for autonomous pump speed adjustment.





## 4 3D printing of functional assemblies with integrated polymer-bonded magnets demonstrated with a prototype of a rotary blood pump

The content of this chapter has been published in *Applied Sciences* [52]. The study was greatly supported by the semester thesis of Yannick Hauswirth.

### 4.1 Introduction

In iterative product development, conventional manufacturing methods with long lead times are a significant bottleneck for fast testing and validation. This holds true especially for the development of products that use magnets, where the fabrication of custom magnet shapes by e.g. sintering, hot-pressing or injection molding is time- and cost-intensive and requires special tooling [91].

Furthermore, conventional manufacturing techniques restrict the design of new and complex structures not only for magnets but also in product development because the assembly steps necessary to integrate the magnets into parts impose restrictions on design and prolong iteration cycles. The use of rapid manufacturing methods for magnets during prototyping phases could, therefore, be of great benefit.

Recently, studies have applied 3D printing techniques to magnetic materials to produce magnets with complex geometries and tailored magnetic fields. Li et al. [92] used pellets of a NdFeB/Nylon compound to print large magnets with a remanence of 510 mT by big area additive manufacturing. Huber et al. [93,94] used a similar compound to produce filaments with high NdFeB content for printing magnets with a remanence of 314 mT via FDM. While these approaches are

#### 4 3D printing of magnets integrated in a RBP prototype

based on polymer-bonded magnetic compounds, Jaćimović et al. [95] printed purely metallic magnets by the means of selective laser melting of NdFeB powder reaching the maximum remanence measured in any printed permanent magnet of 590 mT. Further approaches for additive manufacturing of magnets include binder jetting [96] and direct ink writing [97,98].

With the exception of Li et al. [99] who demonstrated the use of a printed magnet in a conventional DC motor, the translation of 3D printed magnets to actual use cases has not been made. For printing by FDM [93,94] an inhibiting factor might be the reported use of non-optimized injection molding compounds that result in brittle filaments poorly suited for unsupervised handling on an FDM printer.

Extensive iterative testing is of critical importance especially during the development of biomedical devices to ensure reliable operation and successful approval procedures. Next to heart transplantation, VADs are the only option for patients suffering from end-stage heart failure. VADs that are rotary blood pumps (RBPs) have magnets as critical components in the driving and bearing systems of the impeller. Currently available VADs have the undesired side effects of hemolysis and thrombus formation that have to be addressed in the design and development phase of next-generation devices [100]. Computational fluid dynamics is often used in the early design stage, however, it is imperative to validate computational data experimentally [26]. While standard 3D printing is already partly being applied in VAD development [101–103], to the best of the authors' knowledge, 3D printing of magnets is not yet being used for testing new designs of medical devices.

In this work, a functional pump with a magnetic driving and bearing system is printed in one print to show the feasibility of combining multiple material printing and magnet printing for the rapid development of VADs. For this purpose, a flexible, highly-loaded magnet compound filament (MagFil) is developed that can be processed on a low-cost, end-user multi-material FDM printer. The chosen design exploits the design freedom of additive manufacturing and could not be manufactured conventionally.

**Table 4.1:** Empirically found printer parameters for the developed polymer-bonded compound filament (MagFil).

Parameter	Value
Extruder temperature	220 °C
Layer height	0.15 – 0.25 mm
Printer speed	25 mm/s
Infill density	100%
Infill pattern	Rectilinear
Bed temperature	60 °C

## 4.2 Materials and methods

### 4.2.1 Additive manufacturing

For the printing process a low-cost, end-user FDM printer was chosen (Prusa i3 MK2 with a multi-material upgrade, Prusa Research, Prague, Czech Republic). It is capable of printing up to four different thermoplastic filaments in one print. Four Bowden style dual extruders are attached to the frame of the printer. Flexible tubes guide the filaments from the extruders to a so-called multiplexer on the printer head. The multiplexer joins the four filament channels leading to a 0.6 mm diameter nozzle. All materials are extruded through the same nozzle. During phases in the print job, where a filament is not used, it is retracted into the multiplexer for solidification. The print bed is coated with a polyetherimide sheet. The empirically found printing parameters for the developed MagFil material are presented in Table 4.1.

### 4.2.2 Filament materials

A 5-component polymer-bonded magnetic compound was developed for the fabrication of a filament optimized towards a high powder loading and mechanical flexibility. The components were a magnetically isotropic NdFeB powder, an isotropic NdFeB powder/Polyamide-12 (PA12) compound used in injection molding, polyoxymethylene

#### 4 3D printing of magnets integrated in a RBP prototype

**Table 4.2:** Composition of the developed flexible polymer-bonded compound filament (MagFil).

Ingredient	Type	Weight fraction	Volume fraction
NdFeB powder	MQP-S-11-9 (NdPrFeCoTiZrB), (Magnequench, Tübingen, Germany)	66.03%	42.34%
NdFeB/PA12 compound	BMNPI-60HR (Bomatec Automotive, Höri, Schweiz)	24.46%	23.07%
Polyoxymethylene	Kepital F10-01 (Tekuma Kunststoff, Reinbek, Germany)	7.34%	24.79%
Dispersing agent	Edaplan 935 (Muenzing Chemie, Abstatt, Germany)	1.98%	9.35%
Fumed silica	Aerosil (Evonik, Essen, Germany)	approx. 0.20%	approx. 0.44%
Total magnet powder <sup>1</sup>	-	88.53% <sup>2</sup> /91.40% <sup>3</sup>	56.19% <sup>2</sup>

<sup>1</sup> The total amount of magnetic particles contributed by NdFeB powder as well as NdFeB/PA12 compound. <sup>2</sup> Calculated from amounts used in the composite.

<sup>3</sup> According to thermogravimetric analysis.

(POM) as the main matrix material, a dispersing agent and Aerosil as rheology optimizing additive. Table 4.2 gives details on the materials, manufacturers and the compound composition.

The diameter and shape of the NdFeB powder particles (MQP-S-11-9) were given by the manufacturer as spherical with a diameter of  $42 \pm 13 \mu\text{m}$ . The NdFeB/PA12 compound had a specified magnetic powder filling of 60 vol.%. Details on the size and shape of the compounded magnetic particles were not disclosed by the manufacturer. The remanence, intrinsic coercivity and maximum energy product of the NdFeB powder and the NdFeB/PA12 compound are presented in Table 4.3. Both the NdFeB/PA12 compound and POM were obtained as granules. Both polymers (PA12 and POM) have a high melt flowability and excellent mechanical strength and toughness. Therefore, they are suited for processing as highly-filled plastics. To further reduce the viscosity of the composite and to ensure a homogeneous particle distribution in the matrix, a high molecular weight dispersing agent was used. It was further intended to serve as corrosion protec-

**Table 4.3:** Magnetic properties of the NdFeB powder, the NdFeB/PA12 compound and the MagFil material.

Parameter	NdFeB powder	NdFeB/PA12 compound	MagFil material
Remanence [mT]	730 – 760 <sup>1</sup>	515-575 <sup>2</sup>	353 (SD = 6 %)
Intrinsic coercivity [kA/m]	670 – 750 <sup>1</sup>	620-800 <sup>2</sup>	711 (SD = 0.2 %)

<sup>1</sup> According to the manufacturer Magnequench, USA. <sup>2</sup> According to the manufacturer Bomatec, Switzerland.

tion and for mitigating fire risk of the dry NdFeB powder and was added as 3% of the powder weight. To improve powder flowability and reduce friction between the magnet particles a small amount of fumed silica was added. Initial experiments revealed that the order of mixing influences the processability and homogeneity of the compound. The following order proved to be beneficial: First, mixing the NdFeB and fumed silica powders and, separately, the POM granules with the dispersing agent. Then, combining the two mixtures with the NdFeB/PA12 compound granules, for further processing.

The compounding of the final mixture and filament extrusion was performed on a parallel twin-screw extruder with a nozzle diameter of 2.5 mm (Process 11, ThermoFisher Scientific, Karlsruhe, Germany). The 8 temperature zones Z were set with increasing temperature from 200 °C at the feeder (Z1) to 220 °C at the nozzle (Z8) (Z1/Z2: 200 °C, Z3/Z4: 210 °C, Z5/Z6: 215 °C, Z7/Z8: 220 °C). The extrudate was collected by a conveyer belt and cooled down with an air stream for accelerated solidification. A filament diameter of 1.75 mm was targeted by adjusting the speed of the conveyer belt. Subsequently, the filament was spooled onto a 0.45 m diameter spool using a spooling machine (Belt Take-Off BAW 1300 with Horizontal Winder WR 650, Collin, Ebersberg, Germany) and later transferred to a standard spool with a diameter of 10 cm.

Further materials used for printing of the pump prototype were a polylactide (PLA) filament (PLA silver 1.75 mm, Prusa Research, Prague, Czech Republic) and a butenediol vinyl alcohol copolymer (BVOH) filament (BVOH 1.75 mm, Verbatim, Tokyo, Japan).

### 4.2.3 Magnetization

The printed objects were magnetized with a pulse magnetizer (MC Magnetizer, MAGSYS Magnet Systeme, Dortmund, Germany) using a Bitter electromagnet at Arnold Magnetic Technologies AG, Switzerland with a maximum magnetic flux density of 6 T.

### 4.2.4 Material characterization

Scanning electron microscopy (LEO 1530, Zeiss, Jena, Germany) images were taken to determine the shape, size and distribution of Nd-FeB particles in the polymer matrix. The average particle size was determined by measuring the diameter of 100 particles visible on the fracture surface. To this purpose, a filament was broken manually and the fracture surface coated with 5 nm of Gold (CCU-010 sputter coater, Safematic, Zizers, Switzerland). The gravimetric fraction of NdFeB particles was determined with thermogravimetric analysis (STA 449C, Netzsch, Selb, Germany) in Argon atmosphere by heating to 700 °C at 10 °C/min. The filament density was determined according to Archimedes' principle with water as the immersible phase.

To evaluate the remanence and intrinsic coercivity of printed parts and their variation, the demagnetization curves of ten printed cylinders ( $d = 15$  mm,  $h = 5$  mm) were measured using a permagraph (Permagraph L, Magnet-Physik, Dr. Steingroever, Cologne, Germany). Furthermore, the surface roughness of the cylinders was determined using a laser scanning microscope (VK-X260K, Keyence, Osaka, Japan). The roughness was determined separately for vertical and horizontal surfaces. Ten profile lines per sample with a length of 700  $\mu\text{m}$  were used. The profile lines were aligned parallel to the building direction for vertical surfaces and angularly distributed for horizontal surfaces.

### 4.2.5 Pump demonstrator design and testing

The basic design of the pump prototype is similar to that of conventional RBP designs, however, complicated geometries with inside twists and undercut elements would not allow for conventional manufacturing. The bearing concept for the impeller consists of two passive

magnetic bearings for radial forces and a pivot tip for axial forces. For the radial magnetic bearings, hollow cylinder magnets are integrated into impeller and housing. The impeller comprises four blades with twisted internal blade channels in a helical shape around the inflow axis (Figure 4.1 (a)). In each of the blades, a driving magnet was embedded just above the bottom surface. The shape of the magnet was matched to the blade geometry, thereby maximizing the magnet volume (Figure 4.1 (b)). The impeller is actuated by magnetic coupling to a set of matching non-printed permanent magnets spinning on a servo motor just below the housing. The housing and the impeller were printed in one single print using three different filament materials. The MagFil filament was used for printing the magnetic components, a PLA filament was used as the building material in which the magnets are embedded and a BVOH filament as a water-soluble support material to support overhangs during printing and to separate the impeller and housing (Figure 4.1 (b), MagFil: black, PLA: silver, BVOH: white). After the magnetization step, the major fraction of the support material was dissolved by placing the entire part in water for several hours. As the support material showed insufficient solubility in small gaps, the pump was cut open and glued back together after removal of residual BVOH. The pump prototype was coated with silicone grease from the outside to prevent leakage during testing. The hydraulic performance of the pump was tested with water using an ultrasonic flow probe (TS410/ME-11PXL, Transonic Systems, Ithaca, NY, USA) and pressure sensors (MX960, Smiths Medical, Minneapolis, MN, USA) at the pump in- and outlet.

## 4.3 Results and discussion

### 4.3.1 Material characterization

The extruded filament had sufficient flexibility to be spooled to a conventional filament spool with a diameter of 10 cm and could be processed on a Bowden principle FDM printer, in which filaments undergo significant bending. This is an improvement compared to published polyamide-based compositions (PA11 [3,4], PA12 [5]) that yield brittle filaments processable only with large bending radii. Initial experi-

#### 4 3D printing of magnets integrated in a RBP prototype

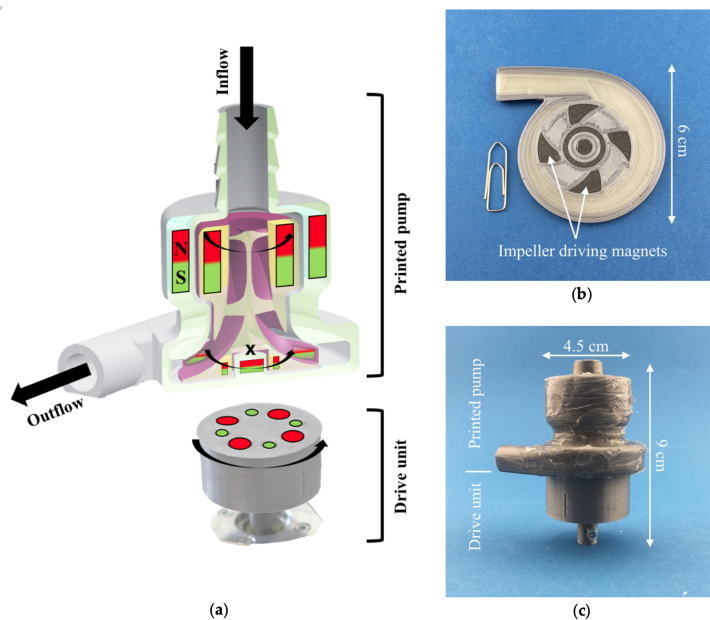


**Figure 4.1:** (a) Design scheme and coupling of the printed pump with integrated driving and bearing magnets in the housing and rotor. (b) Cross-section of the printed pump showing the used materials in different colors (silver: PLA, black: magnetic compound, beige: water-soluble BVOH). (c) Fully printed pump with drive unit after removal of support material (no magnets visible, coated with silicone).

ments with only POM as the matrix phase yielded bendable filaments that were very soft and ground up in the extruder of the printer. The addition of PA12 in the form of NdFeB/PA12 compound increased the resistibility in the extruder of the printer while at the same time maintaining sufficient bendability. A diameter in the range between 1.65 mm and 1.85 mm complying with the required tolerance could be achieved (Figure 4.2 (a)). SEM imaging confirmed the expected spherical morphology and close packing of the NdFeB particles (Figure 4.2 (b)). The average particle size was  $48 \pm 15 \mu\text{m}$ . The residual mass of 91.40 wt.% recorded by TGA analysis was comparable to the amount



### 4.3 Results and discussion

of filler used in the composite (88.53 wt.%, Table 4.2), which indicates that compounding was able to provide good dispersion of the filler within the matrix. The comparison between the measured filament density of  $4.27 \text{ g/cm}^3$  with the theoretical value of  $4.78 \text{ g/cm}^3$  indicates a certain amount of porosity (approx.  $\Phi_{\text{filament}} = 10.6 \text{ vol.}\%$ ).

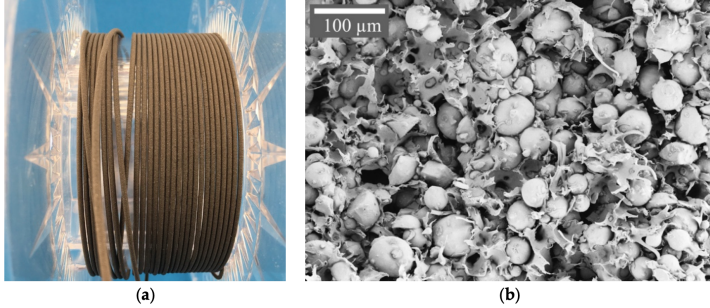


**Figure 4.2:** (a) Polymer-bonded magnetic filament flexible enough to be spooled on a standard filament spool with a diameter of 10 cm. (b) SEM micrograph of the extruded polymer-bonded magnetic compound, NdFeB particles inside the POM/PA12 matrix.

Printing of precise objects with smooth surfaces was achieved. The minimum feature size determined by the extrusion width of a single printed line was approximately  $500 \mu\text{m}$ . The surface of the printed cylinders was smooth with a roughness of on average  $R_a = 23.7 \mu\text{m}$  (SD = 35%) on vertical surfaces and  $R_a = 12.4 \mu\text{m}$  (SD = 17%) on the top surfaces. This surface roughness is well within the range of reported values for standard plastic FDM parts [104–108]. The cylinder size and shape were in very good accordance with the corresponding 3D model (in average 3.5% and 2% larger in diameter and height, respectively). From visual comparison with images of various printed magnets published by Huber et al. [93, 109] it is apparent that the achieved surface quality and geometric precision is equal or better. The density of printed samples  $3.67 \text{ g/cm}^3$  (SD = 7%) indicated a further increase of porosity during printing by approximately 14% to about  $\Phi_{\text{cylinder}} = 24\%$ . This decrease in density due to the printing process was also reported by Huber et al. (15% [94], 22% [93]).

#### 4 3D printing of magnets integrated in a RBP prototype

The remanence of the printed cylinders was  $B_{r,cylinder} = 353$  mT (SD = 6%) which is slightly higher than published values for printable NdFeB compound filaments (314 mT [94] (given), 301 mT [93] (estimated from given compound remanence and density of printed parts)). A theoretical value  $B_{r,th,dense} = 466$  mT can be calculated under the assumption of a dense composite and a linear relation of the volumetric powder filling with the remanence (analog to Huber et al. [94]). Therefore, the measured remanence of the printed cylinders  $B_{r,cylinder}$  exhibits the same deviation of approximately 24% from the theoretical calculation as the porosity  $\phi_{cylinder}$ . Hence, it is likely that the decrease in remanence is mainly caused by porosity and other factors, like oxidation, are not of significance. Figure 4.3 shows the achieved remanences in context of conventionally manufactured and 3D printed magnets as well as theoretical values for the MagFil material based on the volumetric powder filling.

The intrinsic coercivity of the printed cylinders was 711 kA/m (SD = 0.2 %) and seems to be independent of the volumetric powder filling and the porosity of the printed parts, as this lies within the range of the given values of the magnetic starting materials (Table 4.3).

### 4.3.2 Pump demonstrator manufacturing and testing

The aim to fabricate a prototype design of a RBP with magnetic bearing and magnetic drive coupling was achieved. The pump was successfully printed in one print (Figure 4.1 (c)) with a print time of approximately 15 h and tested after support material removal and silicone coating.

During multiple-material printing, the use of a single-nozzle printer is a source for a loss of printing precision and process stability. Occasionally, the MagFil filament is ground up in the extruder due to increased stress during filament changes. The necessity to co-print a wipe-tower to clean the nozzle after each filament change drastically increases the printing time. Contamination of the nozzle with the oily dispersing agent from the MagFil material diminishes proper layer adhesion of the concomitantly printed filaments PLA and BVOH. Furthermore, the feature size for PLA- and BVOH-regions is limited due to the use of a large 0.6 mm diameter nozzle necessary to prevent

### 4.3 Results and discussion

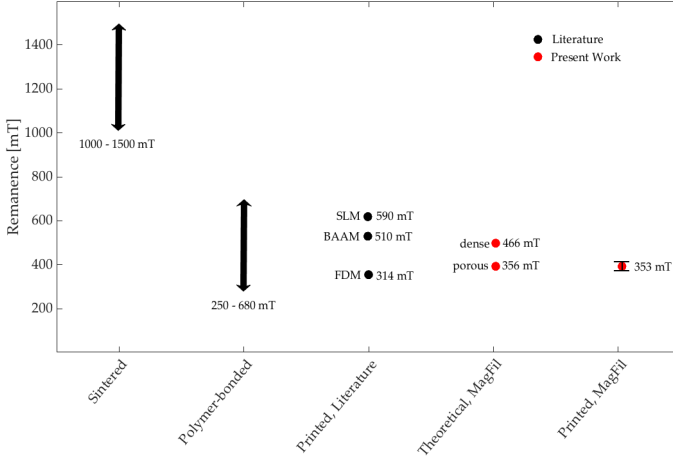


**Figure 4.3:** Comparison of remanences of NdFeB magnets in the form of commercially available sintered magnets [108], polymer-bonded magnets [109], magnets printed by SLM [95], big area additive manufacturing [92], and FDM [94] (Printed, Literature), theoretical remanences of the developed polymer-bonded magnetic compound as dense material and according for a porosity of 24% (Theoretical, MagFil) and the measured remanence of printed MagFil cylinders (Printed, MagFil; SD = 7%).

clogging by NdFeB particles. A simple solution targeting all named problems with low investment costs could be the use of a multi-nozzle printer, that renders filament changes unnecessary and allows to use different nozzle diameters for each material. While this is expected to raise the printing quality to the standard FDM level, the FDM-inherent residual surface roughness will remain and might limit the range of applicability of the present method.

An operation of the pump prototype at a maximum rotational speed of 1000 rpm with a flow of 3 L/min against a pressure head of 6 mmHg was achieved. At higher rotational speeds the magnetic coupling broke off and the delivered flow decreased concomitantly. The pump prototype could therefore not deliver sufficient flow at head pressures that

#### 4 3D printing of magnets integrated in a RBP prototype

are realistic for clinically used VADs. This can be linked to the inferior printing quality caused by the above-described difficulties during multi-material printing. Due to insufficient layer adhesion of the PLA material and subsequent layer delamination, the pump surfaces were rougher and small features less precise compared to usual FDM parts. This caused additional friction and imbalances, for which the strength of the printed magnets was insufficient to compensate. Furthermore, the rough inner surfaces and the material choice render hemocompatibility highly unlikely [110].

The presented method allows only one polarization over all magnetic parts of one print, as a demagnetized powder is used during printing and the magnetic parts are magnetized when already embedded. A possible approach is to use already magnetized hard magnetic particles or to magnetize the particles during the printing process. These particles could then be aligned when exiting the nozzle by magnetic fields as shown by Kim et al. [111] for direct ink writing of magnetic elastomer composites.

## 4.4 Conclusion

A functional prototype of a RBP was 3D printed to demonstrate the effectiveness of all-in-one 3D printing with magnetic materials for rapid prototyping. The presented method allows integrating arbitrarily shaped permanent magnets in a single print. In comparison with similar work, our polymer-bonded magnetic filament could be printed from a standard spool without breaking and is processable on a low-cost Bowden style printer. Furthermore, slightly higher remanences were achieved compared to current magnetic FDM prints.

Beyond the presented case of blood pump development, 3D-printing of integrated magnets allows to increase design complexity early in the product development at low costs and contributes in speeding up the development process of medical devices.

# 5 In vitro testing and comparison of additively manufactured polymer impellers for the CentriMag blood pump

The content of this chapter has been published in the *ASAIO Journal* [53]. The project was conducted in collaboration with Jonas Abeken (The Interface Group, Institute of Physiology, University of Zurich, Zurich, Switzerland), who performed the CFD for this study. Florian Mauz conducted the hydraulic characterization of the assembled blood pumps. The author's contribution is the characterization of the surface roughness and geometric accuracy of the impellers and the hemolysis testing of the pumps. Furthermore, the author conducted data analysis and statistics, in which he was supported by Seminar of Statistics of ETH Zurich and its students Stanimir Ivanov, Foong Wen Hao, Reto Zihlmann.

## 5.1 Introduction

AM has become an indispensable tool in research and development because it offers many advantages e.g. in the production of prototypes [48]. However, the application of AM is only feasible if the results of tests with printed prototypes are not affected by the manufacturing method itself and can be transferred to the final product, for which other materials and manufacturing processes might be used. In addition to the basic mechanical properties and biocompatibility, the limited manufacturing accuracy and generally increased surface roughness of AM parts are of particular concern. In the development of VADs with e.g. complex impeller geometries AM is useful for the

quick validation of computer simulations and extensive testing of design variations [23, 26, 102, 112–114]. Few studies have investigated the applicability of AM in VADs, but deviations in hydraulic properties and increased *in vitro* hemolysis have been observed [101, 103]. However, those studies did not cover the broad range of new and continuously improving AM processes and materials. In this study, we have therefore investigated the applicability of four state-of-the-art AM processes for polymers for *in vitro* testing of hydraulic properties and hemolysis using the CentriMag blood pump impeller as an application example. Associations between the part properties of the additively manufactured impellers with the deviation from the original impeller in hydraulic and hemolysis testing were evaluated.

## 5.2 Material and methods

### 5.2.1 Integration into the CentriMag pump

The CentriMag is a commercial extracorporeal centrifugal blood pump that can operate at pump speeds ( $n$ ) of 1000 to 5500 revolutions per minute (rpm) with flow rates ( $Q$ ) up to 10 L/min. It can therefore be used both as ventricular assist device (pressure head  $H \approx 110$  mmHg,  $Q \approx 5$  L/min,  $n = 2350$  rpm, "VAD-like operating point") and for extracorporeal membrane oxygenation ( $H \approx 360$  mmHg,  $Q \approx 5$  L/min,  $n = 4050$  rpm, "ECMO-like operating point"). It has a magnetically levitated impeller and provides a low blood damage profile that is manifested in very low hemolysis levels (normalized index of hemolysis ( $NIH$ )  $< 3$  mg/100L, [115]). It consists of a control unit, a motor unit and a disposable pump head (Figure 5.1). Its hydraulic characteristics are most commonly described by the relation of  $H$  with  $Q$ , which is represented by performance curves at constant  $n$  in so-called HQ diagrams. The motor current ( $I$ ) needed to achieve a given  $Q$  can similarly be illustrated in so-called IQ diagrams.

The geometry of the impeller body was reconstructed from an optical 3D scan of the CentriMag impeller and additively manufactured by an external supplier (1zu1 Prototypen GmbH & Co KG, Dornbirn, Austria). The ISO 10993 certified biocompatible glue Loctite 4061 (Henkel, Düsseldorf, Germany) was used to assemble the im-

PELLER replicas with additional impeller and housing parts into functional pump heads as shown in Figure 5.1 (parts provided by Thoratec Switzerland GmbH (part of Abbott), Zürich, Switzerland).

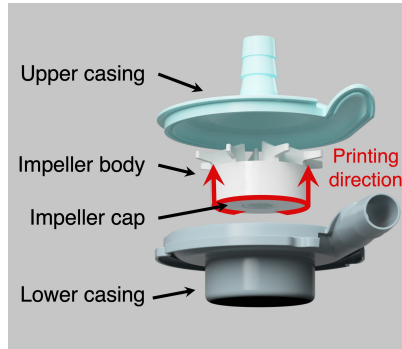


**Figure 5.1:** Schematic of the assembly of the CentriMag pump head. In this study, the impeller body was additively manufactured along its rotation axis ("Printing direction").

### 5.2.2 Fabrication with additive manufacturing processes

Four different AM machines for macroscopic hard-polymer objects were selected for the production of replicas, namely selective laser sintering (SLS), multi-jet fusion (MJF), material jetting (MJ) and stereolithography (SLA). The popular FDM process was not used in this study because the print resolution was insufficient to produce the thin parts ( $< 0.7$  mm) of the CentriMag impeller. Widely used equipment was selected from companies that are among the five largest manufacturers of industrial printers [116] based on the highest printing resolution in their category while striving for coverage of a range of printing approaches. While all machines can process biocompatible materials, standard materials were used for reasons of availability. The AM process and material specifications, shown in Table 5.1, were collected from the manufacturers as well as the literature. A detailed description of the printing processes is provided in the supplementary

## *5 In vitro testing of additively manufactured impellers*

material. The impellers were printed along the axis of rotation (Figure 5.1). Additionally, three disc-shaped specimens for water absorption tests were printed with  $0^\circ$ ,  $45^\circ$  and  $90^\circ$  relative to the printing direction. Only the process-specific minimal post-processing was performed.



**Table 5.1:** Manufacturing processes.

Manufacturing category	Conventional	Powder Bed Fusion	Powder Bed Fusion	Photopolymerization	Photopolymerization
Manufacturing process	Injection Molding (IM)	Selective Laser Sintering (SLS)	Multi Jet Fusion (MJF)	Material jetting (MJ)	Stereolithography (SLA)
Machine	n.a.	Formiga P110 Velocis PA12	Jet Fusion 3D 4200 PA12	Objet Eden 350V	Viper S12
Material	Makrolon 2858 Thoratec Switzerland GmbH, Zurich, Switzerland	EOS, München, Germany	HP, Palo Alto, CA, USA	Fullcure RDG 720	Prototherm
Company				Stratasys, Eden Prairie, MN, USA	3D Systems Rock Hill, SC, USA
Support	n.a.	n.a.	n.a.	Part fully embedded in gel-like support material SUP705	Support rods from build material
Biocompatibility*	USP Class VI	USP Class VI	USP Class VI	n.a.	n.a.
Layer Thickness (mm)*	n.a.	0.1	0.08	0.016	0.05
x-y Resolution (DPI)*	n.a.	n.a.	1200 DPI	600 DPI	n.a.
Laser spot size (µm)*	n.a.	<500	n.a.	n.a.	75 ± 15
Density (g/cm <sup>3</sup> )*	1.02	1	1.01	1.18 – 1.19	1.15
Elastic modulus (MPa)*	2400	1600	1800	2000 – 3000	3500
Tensile strength (MPa)*	66	43	48	50 – 65	70
Elongation at break (%)*	50	14	15 – 20	15 – 25	3
Manufacturing costs per impeller (USD)**	n.a.	30	24	70	235

\* Data provided by manufacturers, \*\*As offered by Izul Prototypen GmbH &amp; Co KG, Dornbirn, Austria

### 5.2.3 Characterization of AM parts

Since pump parts must maintain their shape in an aqueous environment, water absorption tests were carried out on disc-shaped specimens (LxWxT: 20x10x1.5 mm<sup>3</sup>) according to the ASTM D-57098 standard. The dimensions and mass of the specimens were measured before and after submersion in deionized water for a period of 24 h at 37 °C. Following aqueous exposure, the external geometry of the assembled impellers was scanned using a GOM-ATOS compact optical metrology system (GOM UK Ltd, UK) and the generated 3D surfaces were compared to the scan of the reference impeller in the GOM In-spect Professional v7.5 software (GOM UK Ltd, UK). The deviation of the AM impellers from reference was measured at 78,000 – 187,000 surface points per impeller with a resolution of 0.01 mm. Two metrics were used to assess printing accuracy: The fraction of surface points in a  $\pm 0.1$  mm tolerance and the mean deviation of surface points to the reference (mean deviation). For each AM process, the accuracy was determined for three replicas from different printing batches to assess the reproducibility of the AM processes.

The surface roughness of the impellers was measured in twelve separate areas (250x375  $\mu\text{m}^2$ ) at locations both parallel and orthogonal to the printing direction using a laser scanning confocal microscope (VK-X200, Keyence, Osaka, Japan) with a 10x objective and a resolution of 1 nm. The roughness parameters  $S_a$  (arithmetical mean deviation of surface profile) and  $R_z$  (maximum peak-valley distance) were extracted using the Multi-File Analyzer Software (Keyence, Osaka, Japan). Since vertical surfaces make up the largest part of the impeller, only the roughness of these surfaces is considered in the analysis.

### 5.2.4 Hydraulic characterization

The hydraulic measurements of the pump assemblies were performed using a mock circulatory loop for static testing. A 40 wt.% glycerine/water mixture was used as the working fluid, which according to Cheng et al. [117] has a viscosity of 3.5 cP at the working temperature of 23 °C. The flow rate was measured with a clamp-on ultrasonic

flow probe (Sonoflow CO.55, Sonotec Ultraschallsensorik Halle GmbH, Halle, Germany). The pressures were measured directly at the pump inlet and outlet with absolute pressure transducers (Type 528, Huba Control AG, Würenlos, Schweiz). Additionally, the motor current ( $I$ ) was measured. The measurement precision of the test bench was determined by five repeated measurements of the reference assembly at a pump speed of 4000 rpm. Details on the setup can be found in the supplementary information. All parameters were measured at about 180 operating points per impeller for  $n$  and  $Q$  in the range of 1000 – 5500 rpm and 0 – 10 L/min, respectively. All motor current data were normalized by the current of the reference pump at the VAD-like operating point ( $I_{\text{ref,VAD}}$ ).

### 5.2.5 Hemolysis

Fresh bovine blood was collected from the local slaughterhouse and anti-coagulated with 10 vol.% of 0.109 M sodium citrate solution. The hematocrit ( $Ht$ ) was adjusted to  $30 \pm 2\%$  by diluting with phosphate-buffered saline. The pH of the blood was checked to range between 7.4 – 7.6. The diluted blood was filtered using blood filters (Dideco Kids D130, LivaNova PLC, London, UK). Five identical recirculating flow loops were constructed according to the standard of the American Society of Testing and Materials (ASTM) F1841-19 for the *in vitro* hemolysis assessment in continuous flow blood pumps [118]. A detailed description of the setup can be found in the supplementary information.

Each hemolysis test was performed with all five pump assemblies in parallel with 500 mL each of blood from the same animal. Blood samples of 2 mL were collected at hourly intervals for 6 h and the plasma hemoglobin ( $PHb$ ) was measured using the Harboe method [119]. The  $NIH$  was calculated according to Equation 5.1 with the increase of  $PHb$  during one sampling interval  $\Delta PHb$  (mg/L), the remaining circuit volume  $V$  (L), the adjusted hematocrit  $Ht$  (%), the flow rate  $Q$  (L/min) and the sampling time  $t$  (min). The tests were repeated three times with blood from different animals for both the VAD-like and the ECMO-like operating condition resulting in 18  $NIH$  values per replica.

$$NIH\left(\frac{mg}{100L}\right) = \Delta PHb \cdot V \cdot \frac{100 - Ht}{100} \cdot 100/(Q \cdot t) \quad (5.1)$$

### 5.2.6 Computational fluid dynamic simulation

CFD were performed to determine the range of wall shear stresses (WSS) and successively laminar sublayer thickness on the impeller. The simulations were conducted on the original pump geometry assuming smooth no-slip walls. The CFD model was based on a previously described setup [44] and is thus only summarized here. A more detailed description is provided in the supplement. Both VAD- and ECMO-like operating conditions were analyzed by prescribing a pressure head of 105 mmHg at 2350 rpm for VAD operation and 350 mmHg at 4050 rpm for ECMO respectively. WSS histograms were extracted every five time-steps and afterward averaged over 10 impeller rotations. The laminar sublayer height  $\delta_v$  was calculated according to Equation 5.2, with the dimensionless wall distance  $y^+$ , the dynamic viscosity  $\mu$ , the WSS  $\tau_W$  and the density  $\rho$ . The laminar sublayer thickness  $\delta_{v,95}$  corresponding to the 95<sup>th</sup> percentile WSS was chosen as a representative lower limit of sublayer thickness on the impeller.

$$\delta_v = y^+ \cdot \frac{\mu}{\sqrt{\tau_W \cdot \rho}} \quad (5.2)$$

### 5.2.7 Statistical analysis

To model the hydraulic behavior, the general additive model function of the R package `mgcv` [120] and a spline regression model were used. The regression included terms for  $Q$ ,  $n$  and the interaction between these two terms (Equation 5.3). For each impeller, these terms were obtained separately. The models had high explanatory power ( $R^2_{adj} > 0.99$ ).

$$\begin{aligned} Target(HorI) \sim & s(Q) + s(n) + te(Q, n) + s(n, impeller) \\ & + s(Q, impeller) + te(Q, n, impeller) \end{aligned} \quad (5.3)$$

Estimates and confidence intervals for deviations from the reference at specific operating points were calculated using the variance-covariance matrix of the model coefficients. Furthermore, the root mean square error (RMSE) of the deviation at grid points in the entire speed/flow plane was calculated to assess the global deviation from the reference. T-tests were conducted to compare the mean values of hemolysis testing. P-values below 0.05 were considered as indicators of statistical significance unless indicated otherwise.

## 5.3 Results

### 5.3.1 Printing process and manufacturing accuracy

Per manufacturing method three replicas were produced in separate batches. All replicas had sufficient mechanical integrity and accuracy for assembly and pump operation. The analysis of the 3D scans is shown in Figure 5.2 for one set of impellers. The fraction of surface points with a  $\pm 0.1$  mm tolerance and the mean deviation are presented in Table 5.2 as metrics for accuracy and reproducibility. The SLA replica had the smallest mean deviation overall ( $+5 \mu\text{m}$ ), while the SLS and MJ replicas showed a clear tendency to undersize ( $-81 \mu\text{m}$ ) or oversize ( $+57 \mu\text{m}$ ), respectively. The SLA and MJF impeller showed the smallest ( $\pm 0.5\%$ ) and largest ( $\pm 5.6\%$ ) variation in the  $\pm 0.1$  mm tolerance between batches, respectively. The cost of manufacturing was the lowest for the powder-based processes (SLS, MJF) and about ten times higher for SLA (Table 5.1).

## 5 *In vitro* testing of additively manufactured impellers

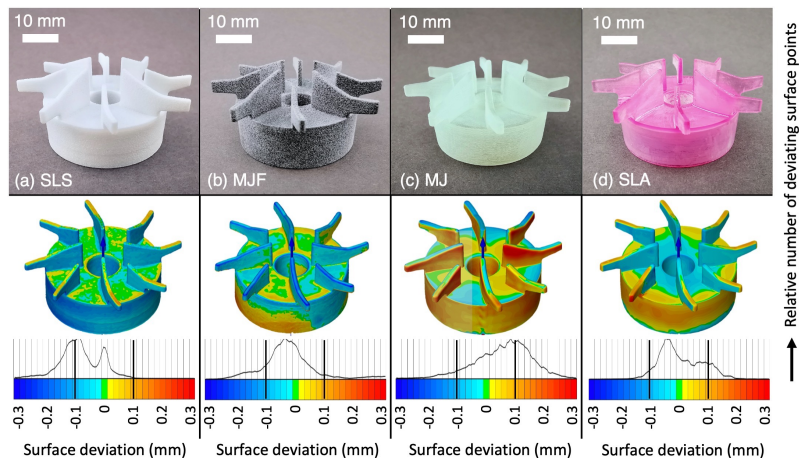


**Figure 5.2:** Photographs (top row) and 3D scans (bottom row) of the replicas manufactured by (a) SLS, (b) MJF, (c) MJ and (d) SLA, see Table 5.1 for details. The 3D scans are colored according to local nominal-actual comparisons with the reference impeller. The degree and distribution of the deviation are shown in histograms, in which the relative number of surface points used for comparison are plotted according to the deviation. The color bars depict the respective surface deviations.

**Table 5.2:** Characterization of additively manufactured specimens.

	Reference	SLS	MJF	MJ	SLA
Fraction of surface points in $\pm 0.1$ mm tolerance (%) <sup>*</sup>	96	65	80	71	92
Reproducibility of $\pm 0.1$ mm tolerance (%) <sup>**</sup>	$\pm 1.3$	$\pm 3.3$	$\pm 5.6$	$\pm 4.2$	$\pm 0.5$
Mean deviation ( $\mu\text{m}$ ) <sup>*</sup>	+13	-81	-18	+57	+5
Surface roughness Sa ( $\mu\text{m}$ ) <sup>***</sup>	$0.8 \pm 0.5$ (1,2)	$7.8 \pm 0.9$ (1,2)	$11.7 \pm 0.5$ (1,2)	$14.1 \pm 1.2$ (1,2)	$5.4 \pm 0.9$ (1,2)
	$0.2 \pm 0.1$ (3)	$5.7 \pm 0.2$ (3)	$12.0 \pm 1.2$ (3)	$4.7 \pm 0.5$ (3)	$0.3 \pm 0.1$ (3)
Surface roughness Rz ( $\mu\text{m}$ ) <sup>***</sup>	$14.5 \pm 5.4$ (1,2)	$67.8 \pm 15.5$ (1,2)	$89.6 \pm 17.8$ (1,2)	$127.2 \pm 13.6$ (1,2)	$26.9 \pm 8.9$ (1,2)
	$4.4 \pm 1.9$ (3)	$59.9 \pm 27.1$ (3)	$109.9 \pm 21.4$ (3)	$72.3 \pm 14.3$ (3)	$5.0 \pm 2.2$ (3)
Water absorption (wt.%)	0.3 <sup>****</sup>	0.56 <sup>*****</sup>	0.71 <sup>*****</sup>	2.5 <sup>*****</sup>	1.13 <sup>*****</sup>

\* Measured for the impeller geometries used for *in vitro* testing as shown in Figure 5.2. \*\* Determined from three impellers per manufacturing method that were printed in different batches \*\*\* Measured on four 250x375  $\mu\text{m}^2$  areas separate on locations (1), (2) and (3) as shown in Fig. 3 (a) and averaged according to the fraction of the respective surface type. \*\*\*\* According to manufacturer. \*\*\*\*\* Measured on disk-shaped specimens.

### 5.3.2 Surface roughness of impellers

Exemplary laser scanning microscopy images and color-coded topography of areas with the surface normal perpendicular to the axis of rotation are shown in Figure 5.3. Surface features resulting from the layer-wise manufacturing can be seen for the SLA and MJ replica. The mean roughness values at different locations of the impellers are given in Table 5.2. All replicas had higher surface roughness than the reference. While the SLA replica had smooth surfaces with a maximum roughness of up to 7 times that of the reference, the other replicas showed 10 – 60 times rougher surfaces than the reference. The roughness of the vertical and horizontal surfaces were similar for the powder-based printing processes (MJF, SLS), while the horizontal surfaces were up to 18 times smoother for the resin-based printing processes (MJ, SLA).

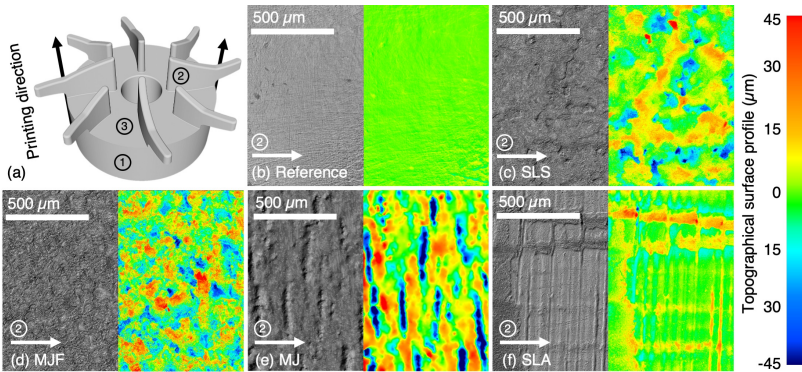


**Figure 5.3:** (a) Illustration of the CentriMag impeller including the indication of the printing direction and the locations of surface roughness measurements (1: sidewall of impeller body, 2: sidewall impeller blade, 3: top side of impeller sidewall impeller blade). (b)-(f) Exemplary laser scanning microscopy images (left) and color-coded topography (right, from blue = lower to red = higher) at the sidewall of an impeller blade of the (b) reference impeller and the replicas manufactured by (c) SLS, (d) MJF, (e) MJ and (f) SLA (Table 5.1).



### 5.3.3 Water absorption

None of the additively manufactured discs showed an water absorption relevant for the application in this study. The largest water uptake was seen for the MJ discs with approximately 2.5 wt.% (Table 5.2). Changes in length, width, thickness or warping could not be observed.

### 5.3.4 Hydraulic characterization

The test bench precision was determined to  $\pm 1.19$  mmHg in  $H$ ,  $\pm 0.15$  L/min in  $Q$  and  $\pm 0.01$  A in  $I$ . A statistical spline regression model was used to analyze the hydraulic behavior of the impellers. The modeled pressure heads of the reference were  $109.8 \pm 1$  mmHg and  $359.5 \pm 1$  mmHg at the VAD-like and ECMO-like operating point, respectively. The modeled relations of  $H$  and normalized motor current ( $I/I_{\text{ref,VAD}}$ ) with  $Q$  are shown in Figure 5.4 in VAD-like and ECMO-like operating conditions.

Apart from an off-set along the  $H$  and  $I$  axis, the curves had the same shape, such that the dependency of  $Q$  was similar for all impellers. The replica assemblies showed an average deviation from the reference of 1.7% and 1.9% in  $H$  and  $I$ , respectively. The local and overall differences between the assemblies are presented in Figure 5.5. Figure 5.6 shows the deviation in  $I$  plotted against the deviations in  $H$  at all measured data points. The MJF impeller showed the largest global deviation in  $H$  and  $I$  with an RMSE of 17 mmHg and 0.065 A, respectively. At the VAD-like operating point, the deviation in  $H$  and  $I$  of the SLS replica was the smallest among all replicas. Interestingly, at the ECMO-like operating point, the SLS impeller generated lower  $H$  over the whole  $Q$  range than the reference (on average  $-5.5$  mmHg, Figure 5.6), while the impellers manufactured by MJ and SLA showed the smallest deviation in  $H$  with less than 1.5 mmHg.

A positive correlation ( $r = 0.88$ ) of  $H$  and  $I/I_{\text{ref,VAD}}$  was found, indicating that impellers generating higher pressure also require higher currents (Figure 5.6).

## 5 In vitro testing of additively manufactured impellers

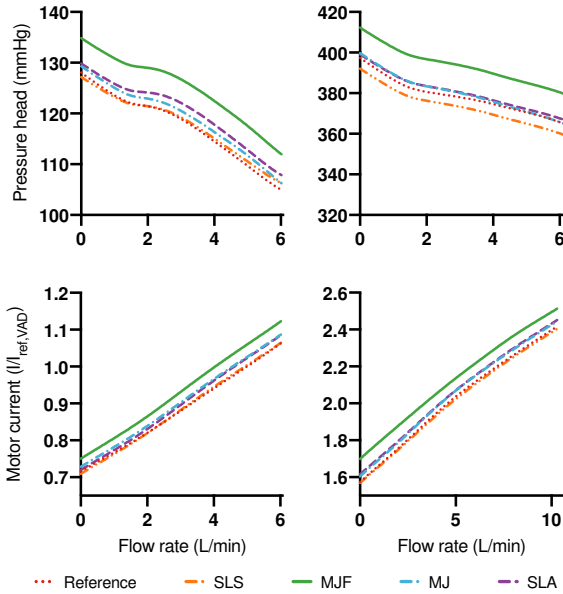


**Figure 5.4:** Relation of pressure head ( $H$ ) and normalized motor current ( $I/I_{ref,VAD}$ ) to flow rate ( $Q$ ) fitted with spline regression models for the CentriMag reference assembly and additively manufactured replica assemblies at stationary conditions of 2350 rpm (VAD-like) and 4050 rpm (ECMO-like).

### 5.3.5 Hemolysis testing results

The results of the hemolysis testing are presented in Figure 5.7. The SLA replica performed closest to the reference with a statistically not significant increase of  $NIH$  of approximately 30% (VAD:  $p = 0.55$ , ECMO:  $p = 0.93$ ). The SLS, MJ and MJF replicas showed significantly higher  $NIH$  values compared to the reference with an increase of up to 500% at the VAD-like ( $p = 7.7 \cdot 10^{-5}$ ,  $p = 0.011$ ,  $p = 0.012$ ) and up to 620% at the ECMO-like operating point ( $p = 3.1 \cdot 10^{-4}$ ,  $p = 1.2 \cdot 10^{-5}$ ,  $p = 5.5 \cdot 10^{-3}$ ). The  $NIH$  showed a positive correlation with the impeller roughness  $S_a$ , with a stronger correlation at the ECMO-like operating point (VAD:  $corr. = 0.72$ , ECMO:  $corr. = 0.84$ ).

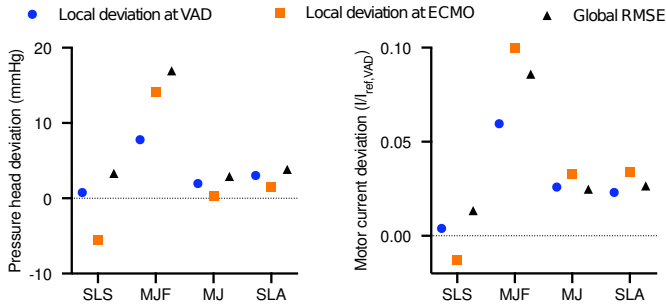


**Figure 5.5:** Comparison of the deviation from the reference in pressure head ( $H$ ) and normalized motor current ( $I/I_{\text{ref,VAD}}$ ) of different replica assemblies. Both the deviation at the VAD-like and ECMO-like operating points as well as the global deviation are shown (represented by the root mean square error (RMSE) of deviations at grid points over the entire  $n$ - $Q$  range).

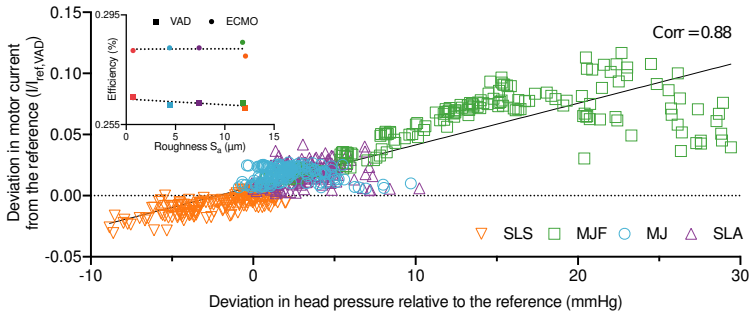


**Figure 5.6:** Deviations from the reference in pressure head ( $H$ ) and normalized motor current ( $I/I_{\text{ref,VAD}}$ ) of the replica assemblies from the reference assembly plotted against each other at all measured data points. The data shows a large positive correlation of  $H$  and  $I/I_{\text{ref,VAD}}$  with a correlation coefficient of 0.88. The subplot illustrates that surface roughness does not have a strong influence on the efficiency.

The generated  $H$  of the reference was  $105 \pm 1$  mmHg and  $350 \pm 1$  mmHg at the VAD-like and ECMO-like operating point, respectively.

## 5 In vitro testing of additively manufactured impellers

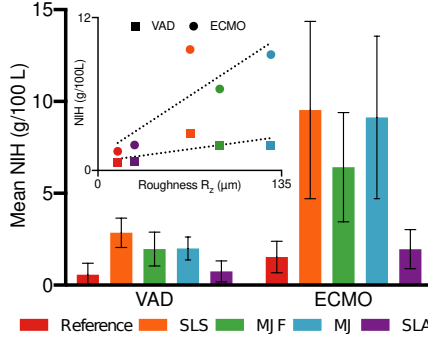


**Figure 5.7:** Comparison of the normalized indices of hemolysis ( $NIH$ ) of the reference and replica assemblies at a VAD-like ( $\approx 105$  mmHg, 5 L/min, 2350 rpm) and ECMO-like ( $\approx 350$  mmHg, 5 L/min, 4050 rpm) operating point. The subplot illustrates the positive correlation between hemolysis and surface roughness with stronger expression at the ECMO-like operating point.

### 5.3.6 CFD simulations

The simulated  $Q$  was 4.96 L/min at the VAD like and 5.00 L/min at the ECMO like operating point. Histograms of WSS acting on the impeller surface are shown in Figure 5.8. At the VAD-like operating point, the average WSS was 47 Pa, and the 95<sup>th</sup> percentile of experienced WSS was 132 Pa. The WSS values at the ECMO-like operating point were about twice as high, with an average of 99 Pa and the 95<sup>th</sup> percentile of 277 Pa. The effect of pressure-induced forces on the calculated rotor torque exceeded the effect of shear-induced forces by an order of magnitude at both the VAD and the ECMO-like operating point. The representative laminar sublayer height at the VAD- and ECMO-like operating condition is calculated to be  $\delta_{v,95,VAD} = 47.0 \mu\text{m}$  and  $\delta_{v,95,ECMO} = 32.5 \mu\text{m}$ , respectively.

## 5.4 Discussion

In this study, four CentriMag impellers were manufactured with different AM processes, characterized with respect to part quality, hydraulic

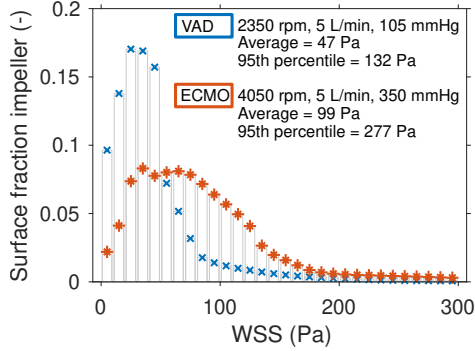


**Figure 5.8:** Simulated wall shear stress (WSS) distribution on the impeller surface during VAD-like and ECMO-like operation of the CentriMag pump. At the VAD-like and ECMO-like operating point the 95th percentile of experienced WSSs is 132 Pa and 277 Pa, respectively.

behavior as well as hemolysis, and compared to each other. We elaborate on the causes for observed deviations from the original injection molded impeller and discuss the transferability of our results to other applications.

### 5.4.1 Manufacturing and pump operation

At the VAD-like operating point, the smallest gap between the cylindrical impeller body and the housing is approximately 550  $\mu\text{m}$ . In comparison, the mean deviations of the replicas from the reference geometry in this gap are considerable at  $-130 \mu\text{m}$  (SLS) and  $+120 \mu\text{m}$  (MJ). As the surface roughness of most replicas was high and potentially relevant for *in vitro* testing, additional post-processing could be considered. The surface of the MJ replica was particularly rough because it had been fully embedded in support material. If the use of support can be avoided, smoother surfaces may be expected. Deformation of replicas with concomitant friction contact, as observed by Nishida et al. [101], was not an issue in the used magnetic levitation system with large gaps, but might become relevant in different applications with smaller tolerances.

### 5.4.2 Hydraulic performance and hemolysis

Since the rotor torque is dominated by pressure-induced and not shear-induced forces, changes in the bulk flow are necessary to produce noticeable deviations in hydraulic performance. Therefore, no influence of near-wall phenomena is expected. Accordingly, the impellers show almost no difference in efficiency despite a drastic difference in surface roughness (Figure 5.6). The more likely cause for changes in bulk flow are larger geometric deviations of the replicas. However, no systematic correlations could be seen between the metrics for manufacturing accuracy applied here and differences in  $H$  and  $I$ . For example, the MJ impeller showed one of the largest mean deviations, but performed closest to the reference among all impellers. A more complex investigation of the influences of geometric deviation at specific locations seems to be required.

The drastically increased  $NIH$  of most replicas is likely to be caused by surface roughness through increased friction and shear at the impeller surface. This is evident in the positive correlation of the  $NIH$  with surface roughness (Figure 5.7). The effect is pronounced at the ECMO-like operating point, which can be explained by the higher pump speed and the concomitant higher WSS at this operating point (Figure 5.8) that at the VAD-like operation. Although the roughness of the SLA replica is already two to seven times higher than that of the reference impeller, a significant increase in hemolysis is only observed in the other replicas, which have more than ten times greater surface roughness than the reference. This may suggest that there is a threshold for surface roughness below which no additional hemolysis is induced, as previously observed by Maruyama et al. [121] One possible explanation for such a threshold value is the transition from a hydraulically smooth to a hydraulically rough boundary layer, caused by a surface roughness that exceeds the flow-dependent height of the laminar sublayer. A surface with an equivalent sand roughness smaller than the laminar sublayer thickness would be assumed to be hydraulically smooth and without influence on the rest of the boundary layer and main flow [122]. Using the results of the CFD analysis, we can compare the computed laminar sublayer thickness with the roughness value  $R_z$  (Table 5.2) as a good approximation for the equivalent sand

roughness [123] and judge whether the surface roughness is expected to impact the main flow and consequently hemolysis. Only the SLA roughness ( $R_z = 26.9 \pm 8.9 \mu\text{m}$ ) remains below the calculated lower limit of the laminar sublayer height  $\delta_{v,95}$ , while all other replicas would exceed the threshold value in both the VAD- ( $\delta_{v,95,\text{VAD}} = 47.0 \mu\text{m}$ ) and ECMO-like ( $\delta_{v,95,\text{ECMO}} = 32.5 \mu\text{m}$ ) operating condition. This is consistent with the observed results. However, it remains unclear why the SLS impeller caused higher or equal hemolysis levels than the MJ and MJF replicas at lower surface roughness. Therefore, additional effects not addressed in this study are likely to play a role, such as particular damaging surface patterns, material properties or the formation of distinct flow fields.

### 5.4.3 Transferability to other applications

When considering transferability to other applications, a distinction must be made between purely hydrodynamic and hemolysis tests. All four AM processes investigated appear to be suitable for hydraulic testing. As the shape of the HQ- and IQ- curves were similar among all impellers, even for the MJF impeller with the biggest discrepancy from the reference of all replicas, a correction for deviations from injection molded parts could be performed by off-setting the respective curve in H or I. As also stated by Chan et al. SLS provides a good trade-off between manufacturing costs and performance in hydraulic testing [103]. For hemolysis testing, however, SLA seems to be the only suitable method, possibly because only this method can produce surfaces that can be considered hydraulically smooth under the given conditions.

Considering the manufacturing costs, it seems reasonable to use the low-cost SLS process for the production of hydraulic prototypes and to use the more expensive SLA processes for the production of selected designs for hemolysis tests. The presented results apply only to the investigated combinations of AM processes and materials and might not hold if other materials are processed on the same printers.

According to boundary layer theory, the height of the laminar sublayer is inversely proportional to the square-root of the WSS. Given our previously stated hypothesis on the sublayer-dependent impact of

## 5 *In vitro* testing of additively manufactured impellers

surface roughness, we expect our results to be transferable to other applications as long as the WSSs are of a similar magnitude to the present study. A change in sublayer thickness with different WSSs or fluids could render the surfaces of the SLA method hydraulically rough or, vice-versa, make other methods such as SLS usable for hemolysis tests.

### 5.4.4 Experimental limitations

The *in vitro* characterization of the replicas was performed on one impeller of each AM process. However, we have shown that the deviation in manufacturing accuracy between replicas of the same AM process is small compared to the process differences, which suggests replicability of the experiments. By the nature of the experiments, the impeller design and the printing method were confounded. In statistical terms, a different behavior of another design manufactured with the same process cannot be excluded.

## 5.5 Conclusion

The use of additively manufactured parts for *in vitro* testing of blood pumps is feasible but manufacturing inaccuracy and surface roughness have to be considered. Non-systematic manufacturing inaccuracies were identified as a major factor before the surface roughness for deviation of AM replicates in hydraulic performance. In contrast, surface roughness appeared to have a substantial influence on the results when testing hemolysis. The AM parts did not show any deformation or disintegration when exposed to an aqueous environment. It was concluded that all AM processes considered here can be used to manufacture prototypes for purely hydrodynamic testing, while only the SLA process is capable of manufacturing parts that perform similar as injection molded parts in hemolysis testing. The use of AM parts in a different pump system, might require additional validation, especially if the range of WSSs present in the CentriMag pump is exceeded.



# 6 Hemolysis testing in vitro: A review of challenges and potential improvements

The content of this chapter has been published in the *ASAIO Journal* [54].

## 6.1 Introduction

Many medical devices, such as cardiopulmonary bypass systems, mechanical heart valves or endovascular grafts contact blood during use. These devices are associated with the risk of blood trauma induced by non-physiological flow conditions caused by design or manufacturing deficiencies, such as narrow gaps or rough surfaces [121,124]. Damage to blood cells and proteins by elevated shear stress and turbulent flow can have serious consequences for patients, ranging from thrombosis or intestinal bleeding to device failure by clogging [11].

Since medical devices are developed in a regulated environment to minimize the risks to patients, developers test and document the performance of a product to meet the respective safety and efficacy standards prior to market launch. Part of this validation process often involves testing products *in vitro*. For blood-contacting medical devices, this includes the *in vitro* validation of the degree of blood damage caused as defined by the international organization for standardization (ISO) in norm ISO 0993-4 (Biological evaluation of medical devices — Part 4: Selection of tests for interactions with blood).

While blood trauma can manifest itself in various ways, such as platelet activation or degradation of the von Willebrand factor [125], the degree of hemolysis caused by a device is one of the most popular measures due to its relatively simple assessment [126] and the general-

## 6 Hemolysis testing review

izable indication of the mechanical stress on the blood. The hemolytic potential of a device can be tested *in vitro* by assessing the rate of increase of PHb in dynamic models, for example, in recirculating flow loops with human or animal blood samples (Figure 6.1). Such tests can provide valuable information about the hemocompatibility of prototypes and help reduce the number of animal experiments required. They play an important role as research and development tools for a relative comparison of prototypes and devices [112,127], as well as for the extrapolation of the results to clinical outcomes [128].

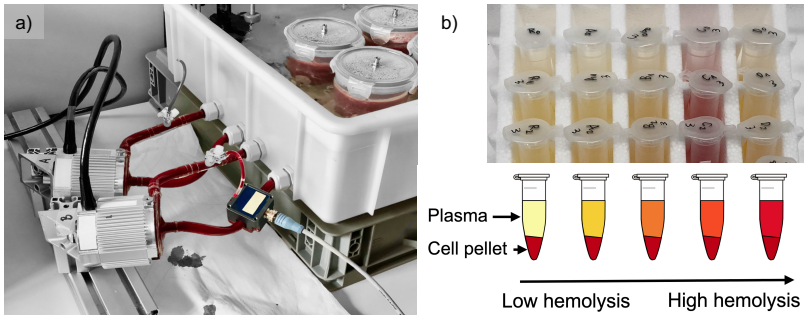


**Figure 6.1:** a) Exemplary test setup for the investigation of the hemolytic potential of CentriMag blood pumps (Thoratec Switzerland AG (part of Abbott), Zurich, Switzerland). The cylindrical reservoirs are immersed in a temperature-controlled water bath [53]. b) Exemplary plasma samples from a hemolysis test and illustration of different degrees of hemolysis. The amounts of hemoglobin concentration released by hemolysis are evidenced by an increase of reddish coloration.

However, the interpretation and comparison of the results are sometimes difficult, as the challenges of blood handling and blood variability persist [129,130]. Therefore, the exploration of new ways to improve current practices remains important for enhancing the quality and comparability of results as well as for reducing the cost and time required for testing. Improving the efficiency and effectiveness of this critical part of the validation chain can serve to accelerate product development, increase the rate of innovation, and provide better and faster treatment to patients in need. Along similar lines, there have been numerous efforts to predict the hemolytic potential of a device through computer-based simulations [17–20].

## 6.2 Challenges of *in vitro* testing of hemolysis

While such simulations have the potential to expedite the evaluation of a design or even to enable an automatic design optimization based on hemocompatibility, they still cannot replace experimental tests thus far. The computational prediction of hemolysis strongly depends on the mathematical modeling and its implementation of the shear force and shear time dependent behavior of erythrocytes [131]. Furthermore, the ability of current models to take into account surface properties and manufacturing inaccuracies still requires a disproportionate computing effort [132]. Therefore, a need for experimental validation remains, as also stated in the international standard for cardiovascular implants ISO 5840-3.

Hence, the aim of the present manuscript is to identify opportunities to improve the current methodology of experimental hemolytic validation. Three challenges that we have identified with *in vitro* hemolysis testing are discussed, along with potential, partly unconventional measures to address these challenges, which are depicted in Figure 6.2.

## 6.2 Challenges of *in vitro* testing of hemolysis

Hemolysis refers to the release of intracellular hemoglobin (Hb) into the blood plasma due to damage of the red blood cells (RBCs). The release of Hb can occur by leaking through the RBC membrane or by a complete destruction of RBCs. In the context of blood contacting medical devices, the focus is on damage caused by mechanical stress, for example, in the form of shearing on rough surfaces or turbulent flow. However, there are also non-mechanical factors that can cause or facilitate hemolysis.

One product category in which *in vitro* hemolysis tests are particularly common are blood pumps for use as ventricular assist devices or in extracorporeal membrane oxygenation. The typical operating procedure is briefly summarized here to serve as a basis for the subsequent discussions.

Hemolysis tests determine the rate of Hb release over several hours under constant conditions. In the case of blood pumps, 450 mL of blood is circulated by the device to be tested, and operating conditions such as flow resistance and flow rate are set according to the final

## 6 Hemolysis testing review

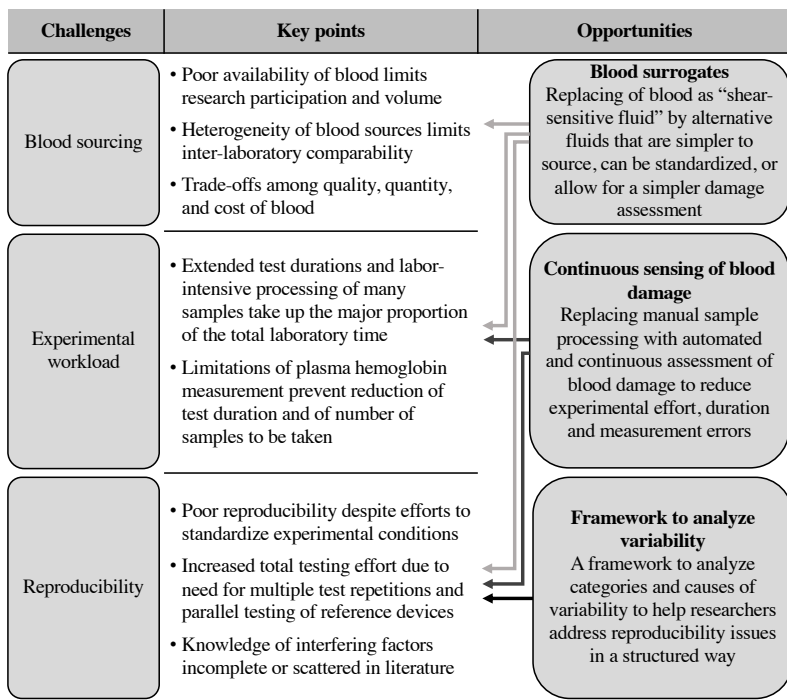


**Figure 6.2:** Overview of the challenges identified and the proposed entry points for alleviating measures. The arrows indicate what challenges are addressed by which measure.

application. While human, porcine, bovine, or ovine blood can be used for testing, obtaining blood is often difficult. We will therefore discuss the challenge of blood sourcing.

The amount of PHb is determined in one-hour intervals for six hours by photo spectroscopic analysis of the blood plasma (Figure 6.3). The rate of PHb increase is calculated from a linear regression over the measurement series. The long experiment time and the measurement of multiple samples entails a considerable effort. We will therefore discuss the challenge of experimental workload.

## 6.2 Challenges of *in vitro* testing of hemolysis

The amount of hemoglobin released depends not only on the device under investigation, but also on the test conditions and blood properties. While this challenge is partly addressed by the standard operating procedure, for example by a normalization of the PHb increase to the hematocrit (Ht) [118,133], it remains a cause of variability between repeated experiments or for a lack of comparability of results reported by different investigators. We will therefore discuss the challenge of reproducibility.

### 6.2.1 The blood sourcing challenge

#### Key Points

- Poor availability of blood limits research participation and volume.
- Heterogeneity of blood sources limits inter-laboratory comparability.
- Trade-offs among quality, quantity, and cost of blood.

The sourcing of blood for *in vitro* hemolysis experiments is subject to two central conditions: (1) Blood must be available in sufficient quantities and (2) it must be used for testing within a short time after collection. Often, blood volumes of several hundred milliliters to several liters are required. This is especially true if several devices are to be tested simultaneously with the blood of a single donor for the purpose of comparability. It is a well-known fact that blood characteristics are subject to significant changes after collection; however, a local sourcing for a short-term use of the blood for the tests is not possible for all researchers. Obtaining large quantities with a short transport time is a challenge and thus not only limits the number of possible experiments that can be carried out, but it also potentially excludes researchers from contributing to this field at all.

The typical sources of human and animal blood and the respective advantages and disadvantages are summarized in Table 6.1. In summary, there is no ideal source due to trade-offs among procurement costs, volume and quality. At one end of these trade-offs, there are

## 6 Hemolysis testing review

fresh human blood samples with the advantages of a potential *in vivo* extrapolation and the disadvantages of small available volumes and ethical concerns. At the other end, there is abattoir blood with the advantage of a reliable and large volume source and the disadvantages of possible pre-damage due to uncontrolled conditions during blood collection and possibly long transport times.

The heterogeneity of blood sources significantly contributes to the poor comparability of hemolysis test results among groups, as it introduces interfering factors affecting, for example, the fragility of erythrocytes. Some aspects, such as the differences between the species, the relevance of the fasting state and the collection method, and the effects of storage conditions have been investigated. However, a comprehensive understanding of the multifactorial causes of hemolysis in *in vitro* experiments is still missing.

## 6.2 Challenges of *in vitro* testing of hemolysis

**Table 6.1:** Advantages and disadvantages of blood sources for *in vitro* hemolysis testing.

	Human		Animal
Source	Volunteers	Expired Donor Blood	Abattoir
Accessibility	Generally available	Limited availability	Location dependent availability
Collection frequency	Limited due to donor recovery time	Limited due to fluctuation in availability	Steady supply strut
Cost	Medium cost for donor compensation	Low cost (clinical waste)	Low cost (waste product in meat production)
Ethical approval	Approval required	No approval required	No approval required
Fasting control	Fasting control possible	No control of fasting state	No control of fasting state (less relevant for ruminants)
Collection	Collection under clinical conditions	Collection under clinical conditions	Collection under uncontrolled conditions, increased fragility possible
Single donor volume	<500 mL	<500 mL	up to 5 – 10 L
Pooling	Pooling not possible	Pooling not possible	Species dependent
Blood age	<several hours	Several weeks	Hours to days
Repeated collection	Repeated collection possible	No repeated collection	No repeated collection
Significance	<i>In vitro</i> extrapolation	Limited <i>in vitro</i> extrapolation	Relative comparison

## 6.2.2 The workload challenge

### Key Points

- Extended test durations and labor-intensive processing of many samples take up the major proportion of the total laboratory time.
- Limitations of measurement technology for the concentration of PHb prevent reduction of the test duration and of the number of samples to be taken.

Hemolysis tests take up to 13 hours to complete. About three hours are needed just for blood collection and preparation (in our lab, collecting and processing blood from the abattoir) and for preparing the test setup. According to ASTM standard F1841 for the assessment of hemolysis in continuous flow blood pumps [118], the actual time of damage testing is six hours (Figure 6.3). If multiple devices are tested in parallel, the tests have to be started sequentially, which increases the test time to seven hours. During this time, samples are taken in hourly intervals and are processed. In addition, certain parameters such as flow rate, temperature or glucose content must be maintained. Finally, up to three hours are required to clean the test setup and complete the sample processing. Timing is crucial in some of these steps. In particular, the time between blood collection and processing must be as short as possible. With repeated centrifugation necessary, the processing of a single sample may take up to 45 min; therefore, several people are usually involved.

The standard protocol described above, involving repeated sampling over several hours, ultimately serves only to determine the rate of increase of PHb. From a fundamental point of view, this rate of increase could also be determined from only two measuring points at the start and end of a much shorter interval. Limited measurement precision requires the collection of many data points to obtain a mean value with statistical validity. Limited accuracy requires longer test periods, during which RBC damage can accumulate and cause larger variations in PHb, which can then be resolved. Thus, the workload described is mainly due to measures taken to compensate for the shortcomings of the PHb measurement technology.



## 6.2 Challenges of *in vitro* testing of hemolysis

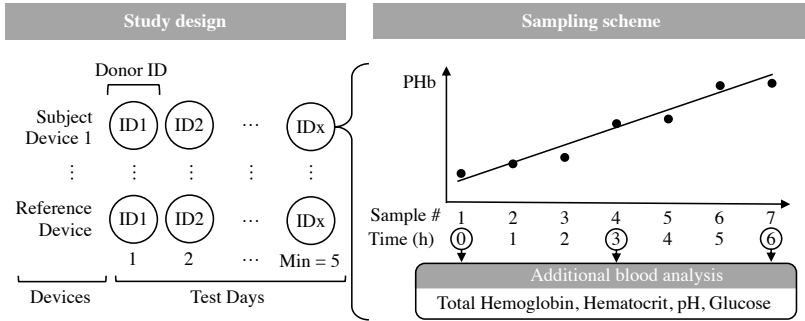


**Figure 6.3:** Exemplary study design and sampling scheme for the evaluation of the hemolytic potential of a blood pump according to ASTM F1841. A minimum of five paired pump tests of the device under investigation and of a commercially available reference device are required, using blood from the same donor per test. A complex sampling scheme is prescribed for each test and device.

### 6.2.3 The reproducibility challenge

#### Key Points

- Poor reproducibility despite efforts to standardize experimental conditions.
- Increased total testing effort due to need for multiple test repetitions and parallel testing of reference devices.
- Knowledge of interfering factors incomplete or scattered in the literature.

Reproducibility, both inter- and intra-laboratory, is a challenge when *in vitro* hemolysis experiments are performed. There is extensive literature that seeks to address this problem by proposing standardization of test setups and test protocols [129, 130, 133–138]. Of particular note are the ASTM standard F1841 on the standard practice for assessment of hemolysis in continuous flow blood pumps and the ASTM standard F1830 on the selection of blood for *in vitro* evaluation of blood pumps, which were first approved in 1997 and last updated in 2019 and 2005, respectively, to incorporate new findings [118, 139].

## 6 Hemolysis testing review

Intra-laboratory reproducibility is the prerequisite for inter-laboratory reproducibility. Therefore, we have performed a meta-analysis using Google Scholar to quantify the intra-laboratory reproducibility in the field of ventricular assist devices in the year 2020. The analysis was limited to publications from 2020 showing hits for the search terms “ventricular assist device + index of hemolysis + *in vitro*”. Of these publications, only primary sources of experimental hemolysis were included ( $n = 9$ ) [45, 53, 140–146]. As a common comparative measure for reproducibility, the absolute coefficient of variation ( $CV$ ) was calculated, which is the ratio of the standard deviation to the mean value of a series of measurements. The  $CV$  was calculated separately for all reported test conditions, totaling 31 collected measurement series with an average of  $51 \pm 3\%$ . Only in one test series, the  $CV$  was less than 10%, while the maximum was 150%. Repeated measurements in the same laboratory on average thus fluctuate by 51% around the mean value, which indicates a rather poor reproducibility.

Many factors are known to influence hemolysis *in vitro* and to interfere with the test of flow-induced damage including blood properties, such as RBC characteristics, plasma composition and donor species [125, 147], as well as blood management, such as transport conditions [148] and methods for hemodilution [149]. Further factors are the test setup for example by the means of tubing length, reservoir type and their surface roughness, as well as inaccuracy or human error in setting the test conditions and measurement of PHb. While such factors have been addressed in literature, they are not sufficiently accounted for in test procedures.

Natural variations in blood characteristics among and within donors are difficult to address. Therefore, the hemolytic potential of devices can typically only be evaluated relative to reference devices, such as established commercial products that are tested in parallel with blood from the same donor. On the contrary, all causes of poor reproducibility that originate in the test setup or in test protocols can in fundamental terms be eliminated by technical development and standardization. However, it is evident that despite efforts to standardize, the value of *in vitro* hemolysis tests for comparable evaluation of blood contacting medical devices *in vitro* and the extrapolation of their performance *in vivo* remains restricted. More experimental studies are needed to

### 6.3 Potential approaches for improving *in vitro* testing of hemolysis

identify the sources of variability, and targeted mitigation strategies and protocols are to be developed.

## 6.3 Potential approaches for improving in vitro testing of hemolysis

Given the importance of hemolysis testing for research and development, it is essential to address the challenges identified. In the following, we provide an overview of promising approaches for researchers who want to improve the validation possibilities of medical device testing. We elaborate on potential approaches and refer to existing literature.

### 6.3.1 Blood surrogates

**Addressed challenges:** Blood sourcing, Workload, Reproducibility

**Fundamental insight:** Blood in hemolysis tests basically acts as an indicator of shear stresses experienced by blood cells as they pass through the device.

**Value proposition:** Replacement of blood as “shear-sensitive fluid” by alternative fluids that are simpler to source, that can be standardized, or that allow for a simpler “hemocompatibility” assessment.

**Limitations:** Reproducing the complex and time-dependent mechanical behavior of RBCs.

As discussed above, the extrapolation of *in vitro* hemolysis testing to clinical outcomes is very limited. Primarily, it is a tool for early assessment of hemocompatibility and relative comparison of devices to each other. In addition, little information is gained in hemolysis testing about the specific causes or mechanisms of the respective blood damage observed. The complexity of the full system is reduced to a one-dimensional metric that serves as a measure of the mechanical

stress on the blood. The driving idea of this section is that the same information content could be obtained with alternative shear-sensitive fluids (Figure 6.4).

At the same time, many of the disadvantages of blood described, such as limited access and lack of availability, delicate handling and storage, heterogeneity of sources, and natural variation among donors could be alleviated. In the quest for alternatives to animal testing, similar concepts for alternative *in vitro* models have already been gathered by Doke et al. [150], such as animal cell cultures or microorganisms like yeast, that can serve as inspiration. In addition, replacing blood to evaluate shear stress also offers the opportunity to simplify the assessment of hemocompatibility compared to the measurement of Hb release from RBCs.

Empirical studies have shown that flow-induced hemolysis is a complex function of both shear stress and exposure time. The mechanisms of hemolysis are not well understood, but it is believed that hemoglobin release occurs either following cell destruction when the time-dependent critical shear stress is exceeded, or by release through the cell membrane following subcritical damage [151–153]. In addition, blood shows a non-trivial shear-thinning behavior, which is a relevant property change of blood in response to shear stress. The main challenge in replacing blood may therefore be to remodel these properties sufficiently accurately in blood surrogates, especially because precise baselines of reported blood properties are lacking.

### **Suspensions of synthetic microcapsules**

In a very simplified description, RBCs are natural microparticles that transport hemoglobin in their lumen. Similarly, there exists a range of synthetic microparticles that can hold cargo substance in a lumen called microcapsules (Figure 6.4b and 6.4c). These microcapsules include liposomes, polymersomes, and other polymeric capsules. They vary in size, shell composition, and manufacturing technique.

Dispersions of artificial microcapsules hold great promise for providing a standardized system for early hemocompatibility evaluation. Such particles might not be able to simulate the biological properties

### 6.3 Potential approaches for improving *in vitro* testing of hemolysis

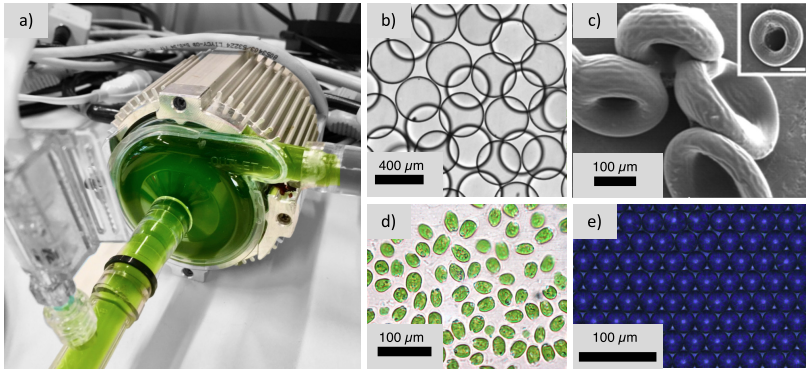


**Figure 6.4:** a) Preliminary study on the use of the unicellular algae *Chlorella vulgaris* for the assessment of the hemolytic potential of blood pumps (here CentriMag, Thoratec Switzerland AG, Zürich, Switzerland); b) Microcapsules with ultra-thin polydimethylsiloxane shell. Reprinted from Guo et al. [154] under the CC BY 4.0, 2020 Micromachines; c) Red blood cell-mimicking synthetic biomaterial particles. Reprinted from Doshi et al. [155], 2009 Proceedings of the National Academy of Sciences; d) Microscopic image of the unicellular algae *Chlamydomonas* © 2020 University of Wisconsin Board of Regents; e) Monodisperse water-in-decan emulsion produced by high-throughput microfluidic device (courtesy of Microcaps GmbH, Zürich, Switzerland).

of blood, but they may offer an opportunity to achieve adequate simulation of the RBC mechanical and fatigue properties. An example for tailoring the mechanical properties of microcapsules is the development of shear-stress sensitive liposomes for targeted drug delivery in atherosclerosis patients [156].

Another advantage is the wide range of options for selecting a cargo substance that is released from the microcapsules upon destruction, such as dyes that change color [157] or develop fluorescence [158], as well as substances that change the conductivity or pH of the immersion medium.

Several studies have been published investigating the use of dye-filled microcapsules for relative comparisons of hemolytic properties of blood pumps [159–162]. They used polyurethane-based particles manufactured by interfacial polycondensation and compared their damage profile against those of bovine blood in tests with several centrifugal

ventricular assist devices. Although the mechanical properties and the size of the particles were drastically different from RBCs, their applicability for relative comparisons of the hemolytic potential of medical devices was clearly shown. Other studies pursued the production of artificial RBCs for use in blood surrogates for transfusion [163] and drug delivery [155].

One of the core challenges in providing synthetic cell suspensions could be a cost-effective and large-scale production. For instance, very expensive phospholipids [156] and block-co-polymers [164] are required for the fabrication of liposomes and polymersomes, respectively. The production of microcapsules from standard polymers could therefore be more promising, especially given the recent development of high-throughput microfluidic devices for the production of polymeric microcapsules [165].

### **Polymer solutions**

Pohl et al. [166–168] investigated dilute solutions of long-chain polymers such as polyacrylamide, polyethylene oxide or xanthan gum as a model for flow-induced blood damage in artificial organs. These polymer solutions are easily available in large quantities and they are unproblematic to store making them a particularly attractive alternative to blood. Pohl and coworkers showed that these polymer solutions show a shear-thinning behavior similar to blood and that the polymer molecules are degraded by shear stresses similar to RBCs. Difficulties in the transferability of results could arise in the degradation of polymer molecules as degradation is accompanied by a reduced viscosity, which is not necessarily the case for moderately hemolyzed blood. Furthermore, the properties of the polymers strongly depend on the molecular weight, which can show production-related variations.

### **Suspension of unicellular, cultivatable cells**

In nature, there exist countless unicellular organisms that have a globular shape and are similar in size to RBCs. These include unicellular

### 6.3 Potential approaches for improving *in vitro* testing of hemolysis

algae (Figure 6.4d), which have already raised interest as model organisms for numerous biological fluid dynamics problems because they can be easily cultured on-demand and exhibit a narrow distribution of properties [169]. Algae have also been considered for a large-scale industrial production of nutrients. In this context, damage-free pumping and mixing of aqueous cultures during cultivation and targeted cell disruption for nutrient extraction after cultivation are important. Therefore, there is a rich body of literature on the behavior of algae under shear forces [170] and the measurement methods for the degree of cell damage [171]. In contrast to RBCs, the cell wall of unicellular algae is not composed of phospholipids but of cellulose and peptidoglycan.

An overview of the shear tolerance of different microalgal species is provided by Wang et al. [170]. The critical shear stress of algae is highly diverse and typically orders of magnitude lower than that of RBCs for which values between 125 – 425 Pa were observed depending on the exposure time [151, 172, 173]. However, exceptions exist, for example, with the species *Tetraselmis suecica*, for which a critical shear stress of 88 Pa is reported [170]. In addition, the size and properties of cells may depend on cell division and growth phases. Upon cell damage, chlorophyll and other cellular components are released into the medium. As with hemoglobin, this can be determined by photospectrometric analysis of the supernatant or by measuring turbidity. Other unicellular organisms include yeast cells and bacteria; however, they show critical shear stresses of more than 2770 Pa and 1810 Pa, respectively, and would therefore not be impacted by shear stress usually occurring in biomedical devices [174, 175].

### Emulsions

Emulsions are finely dispersed mixtures of two immiscible liquids, e.g., water droplets in oil or oil droplets in water (Figure 6.4e). In the food and cosmetics industries, customized emulsions are produced by high shear mixing. Conversely, this means that the size distribution of droplets in emulsions can also be used to draw conclusions about the shear forces acting on the emulsion [176]. For example, the degree of

mixing can be assessed by the time needed for complete demixing by coalescence of the droplets [177]. Although no studies are available on the applicability of emulsions as test fluids for hemolysis testing, this option is worth investigating due to the ubiquitous availability of the required materials.

### 6.3.2 Continuous sensing of blood damage

**Addressed challenges:** Workload, Reproducibility

**Fundamental insight:** Limitations of the current PHb measurement technology are core reasons for the high number of experiment days.

**Value proposition:** Replacement of sparse sampling and manual measurement of PHb by an automated and continuous assessment of blood damage, thus reducing experimental effort, experiment duration and measurement errors.

**Limitations:** Capability of alternative technologies is possibly still insufficient.

As discussed above, a large part of the workload is due to three factors: (1) labor-intensive steps from sample collection to measurement, (2) additional effort for multiple sampling required due to limited PHb measurement accuracy and (3) extended experimental duration.

With sensor technologies that would reduce the effort of PHb measurement through automation, the sparse manual sampling could be replaced by continuous data acquisition. This would save researchers time and reduce the risk of measurement errors by eliminating manual steps. In addition, the achievable data density would be orders of magnitude higher, allowing sufficient data confidence to be achieved in reduced experimental time.

#### **Inline plasma separation for continuous PHb assessment**

A promising entry point for the methods mentioned above are technologies with the capability to separate plasma inline and in parallel



### 6.3 Potential approaches for improving *in vitro* testing of hemolysis

to analyze the data spectroscopically. Zhou et al. [178,179] developed a novel sensor for hemolysis detection in whole blood for Point-of-Care measurements in blood gas analyzers (Figure 6.5a). It is produced using the photolithography technique and comprises a combined pattern of nanometer-sized recesses for exclusion of RBCs and other cells, as well as an optical waveguide for the spectral analysis of the separated plasma within the recesses. Although the sensor is designed for application with static samples, it should be applicable as a continuous hemolysis sensor in flowing blood for the following reasons:

(1) The separation of RBCs is based on diffusion and should therefore work independently of flow. (2) The time for diffusion of PHb into the recesses is in the range of milliseconds. This should allow any changes in PHb concentration to be measure without any significant delay. (3) The separation of plasma is achieved without retaining RBCs, which should prevent any clogging. Adaption of the recess pattern design should allow for the improvement of the reported PHb detection limit of 20 mg/dL. The use of additional wavelengths for spectroscopic analysis, as is common in Hb measurement [126], should allow for an improvement in PHb selectivity.

Next to this highly integrated solution, there exists a wide range of active and other passive separation technologies for blood plasma that are based on microfluidics; a comprehensive summary is provided by Kersaudy-Kerhoas et al. [180] Such separators suited for non-clogging operation under continuous flow could be implemented as PHb sensors when integrated in low-flow bypasses to the test loop and combined with a spectral analysis of the separated plasma.

Matthiae et al. [181] demonstrated a combination of passive microfluidic plasma fractionation and Raman spectroscopic analysis of the plasma (Figure 6.5b). The flow rate required was  $<100 \mu\text{L}/\text{h}$  and the PHb detection limit achieved was 22 mg/dL. The microfluidic device used was simple in design and utilized a step-like broadening of a microfluidic channel to increase the natural cell-free plasma layer on walls of microfluidic systems (Fahraeus effect). The cell-free plasma region was stable under flow and sufficiently large to locally perform Raman spectroscopy there.

## 6 Hemolysis testing review

Tripathi et al. [182] developed a passive microfluidic device for clog-free continuous plasma separation (Figure 6.5c). They achieved a separation efficiency at hematocrits of up to 62% and flow rates of up to 0.5 mL/min. This was enabled by leveraging the Fahraeus and the Zweifach-Fung effects, which describe the fact that blood flow through an asymmetric bifurcation leads to higher RBC concentrations in the high-flow branch and the centrifugal force in bend flow channels result in lower RBC concentration at the inner radius.

Other groups have built similar passive setups, however, high separation efficiency was only demonstrated with strongly diluted blood [183–185]. It is therefore unclear whether such setups can be applied in hemolysis tests where blood with physiological hematocrits is used.

Suitable active microfluidic separation techniques include separation by external acoustic [186] and electric fields [187]. Several efforts have been made to simplify the development of such microfluidic devices, for example, through additive manufacturing [188] or laser cutting [189,190], which could lower the entry barrier for the use in hemolysis testing.

### **Alternatives to PHb as metrics for blood damage**

An alternative approach for assessing the level of blood damage is to find metrics that are concurrent to hemolysis but can be measured more precisely. This could allow the determination of hemolytic potential of devices in a shortened testing time.

One promising approach is the assessment of the electric properties of the blood by electrical impedance spectroscopy. It entails the measurement of the impedance at various frequencies with simple electrodes and is a common method for the study of biological systems, such as for the determination of the number and shape of suspended cells. The interpretation of a measured impedance spectrum is often carried out by means of an equivalent circuit diagram, which represents the presumed chemical and physical relationships relevant to the investigation. For example, intracellular and extracellular conductivities can be determined without any physical separation of the two media.

### 6.3 Potential approaches for improving *in vitro* testing of hemolysis

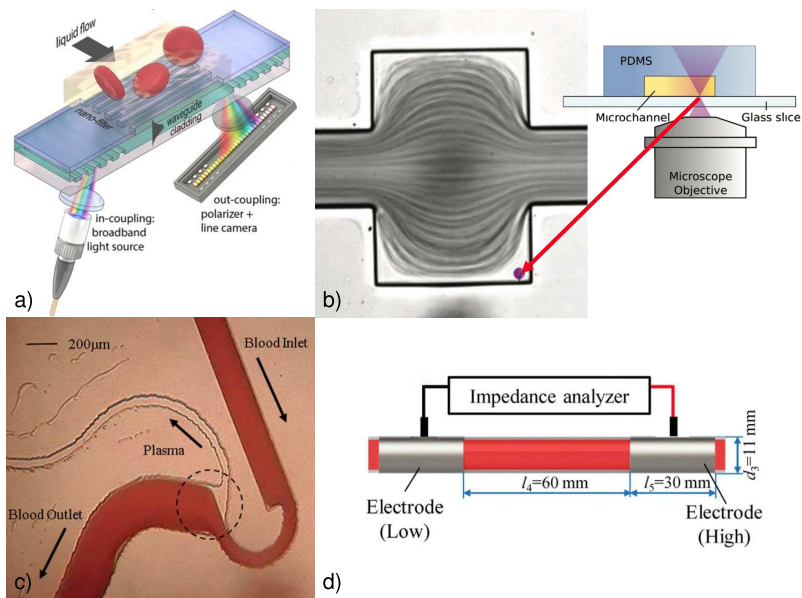


**Figure 6.5:** a) Sensor for measurement of plasma hemoglobin from whole blood sample using cross-filtration for plasma separation and waveguide for spectroscopic analysis of the plasma. Reprinted from Zhou et al. [179] under the ACS AuthorsChoice usage agreement, 2018 ACS Sensors. b) Illustration of a microfluidic device for plasma separation by sudden expansion of the microfluidic channel combined with Raman spectroscopy in plasma region for composition analysis. Reprinted and modified from Matthiae et al. [181] under CC BY-NC 3.0, 2019 Analyst. c) Microfluidic device for continuous, clog-free plasma separation from whole blood using multiple microfluidic effects. Reprinted from Tripathi et al. [182] under a CC BY 4.0, 2016 Scientific Reports. d) Illustration of a measurement setup for impedance measurement of blood under flow through a tube. Reprinted from Li et al. [99], Copyright 2018, with permission from Elsevier.

Using this method, Tran et al. [191] demonstrated a hemolysis detection method for sample rejection prior to blood analysis based on an eight-parameter equivalent model. They applied frequencies from 0.1 – 100 MHz and found a correlation between the PHb concentration and a corresponding model parameter. However, the levels and increments of PHb investigated were high (0 – 480 mg/dL in steps of

## 6 Hemolysis testing review

approximately 100 mg/dL) compared to values typically observed in hemolysis testing.

Destruction of RBCs by hemolysis is also accompanied by a change in hematocrit, as a measure of the volumetric proportion of RBCs in whole blood. Reliable and accurate estimations of hematocrit have been demonstrated by several groups [192–195]. One challenge for translation for an application in hemolysis testing loops could be the fact that electrical parameters of blood are deeply impacted by flow due to orientation and deformation of cells as well as a modification of the electrical double-layer thickness [99]. An illustration of an impedance measurement setup with blood flowing through a tube is shown in Figure 6.5d.

A more selective approach less impacted by secondary effects would be the measurement of single ion species that are involved in RBC damage. A wide variety of ion-selective electrodes are available that could be integrated into test circuits and take continuous measurements in whole blood. One phenomenon that could be leveraged for this concept is the Gárdos effect [196]. The author discovered the efflux of potassium from RBCs upon mechanical stimuli. This phenomenon, however, is mediated by calcium and would not occur in the presence of anticoagulants such as sodium citrate that bind ionized calcium.

### 6.3.3 Framework to analyze variability

**Addressed challenges:** Reproducibility

**Fundamental insight:** Factors for poor reproducibility are extremely diverse and are not sufficiently covered by current standards.

**Value proposition:** A framework for structuring the approach to solving the reproducibility challenge.

**Limitations:** While the framework helps researchers address the issue of reproducibility in a structured way, it does not identify any factors that offer progress in the field.

### 6.3 Potential approaches for improving *in vitro* testing of hemolysis

As discussed above, the factors for poor reproducibility of hemolysis tests are extremely diverse. Also, intra-laboratory variability remains an unresolved challenge. To improve reproducibility, it is essential that the relevant factors are identified and addressed by implementing updates to the current standards. While standardization has begun to enter the field, the information is still scattered, dispersed or hidden. In order to solve the problem in a targeted manner, it is necessary to collect the comprehensive knowledge of possible factors and conduct experimental studies to confirm or reject potential confounding factors. The purpose of this section is to contribute to this effort by proposing a simple overview of categories and causes of variability as a framework for future studies. An overview is provided in Figure 6.6.

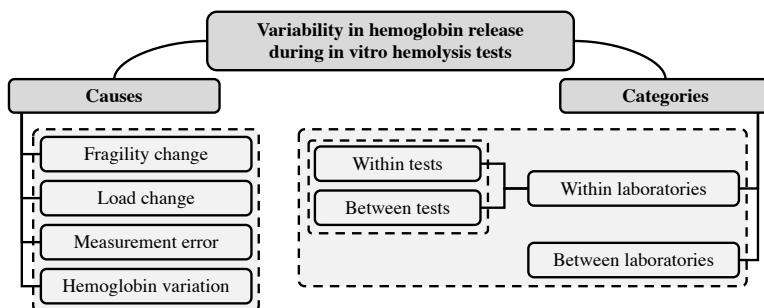


**Figure 6.6:** Graphical representation of categories and causes of variability in *in vitro* hemolysis tests using blood.

For illustration, we suppose that investigators A and B at two different laboratories on Days 1 and 2 each perform a hemolysis test with two perfect replicates of the same medical device. One hemolysis test consists of two measurements of the rate of PHb increase at different times  $t_1$  and  $t_2$ . In this scenario, different variability categories may cause poor reproducibility:

#### **Within-test variability:**

## 6 Hemolysis testing review

Researcher A measures a higher damage rate at time  $t_2$  than at time  $t_1$  and determines a mean value as the daily result. A random cause explanation could be that a thrombus formed halfway through the test, which led to higher damage. A systematic cause explanation could be that glucose consumption during the measurement led to increased cell fragility.

### **Between-test variability:**

Researcher A determines a higher mean value on Day 1 than on Day 2. Using the results of both test days, the hemolytic potential of the device is evaluated. This overall result is subject to uncertainty. A random cause explanation would be that it took more time to bring the blood from the abattoir to the lab on Day 1 than on Day 2. A systematic cause explanation would be that a protective protein layer was deposited due to a lack of cleaning of the test setup.

### **Within-laboratory variability:**

Researcher A publishes the evaluation of the hemolytic potential with an uncertainty. The origin of this uncertainty could be exclusively in the within-test variability or in the between-test variability. A mixed origin is also possible.

### **Between-laboratory variability:**

Researcher A measures a higher overall injury than Researcher B. The random cause explanation would be that at least one of the researchers has a high within-group variability, which by chance led to this overall difference. A systematic cause explanation would be that researcher A uses tubing that causes additional hemolysis.

The origin of a variability is not directly evident from the overall result; however, all types of variability have different causes. It is therefore central to the derivation of appropriate measures to analyze from which category of variability the problem arises. Regardless of the category of variability, the cause of a variation in the result can always be assigned to one of the following four.

### 6.3 Potential approaches for improving *in vitro* testing of hemolysis

#### **Fragility change:**

A change in RBC fragility results in a change in the release rate of PHb. The change of fragility during a test, such as by cell fatigue, would lead to a within-test variability. Different fragility levels between two test days, for example, due to different transport temperatures, would lead to between-test variability. Different fragility levels between laboratories, for example, by using blood of different species, would also lead to a between-laboratory variability.

#### **Load change:**

A change in RBC loading leads to a change in the release rate of PHb. Changing the load during a test such as by changing the viscosity with increasing damage would lead to a within-test variability. Different loading between two test days, for example, due to one-time contamination of the test setup, would lead to a between-test variability. Different loading between laboratories, for example, by using different chokes would lead to a between-laboratory variability.

#### **Hemoglobin variation:**

Hematocrit and intracellular hemoglobin content vary between donors. The higher the hematocrit, the more cells can be damaged, and the higher the intracellular hemoglobin content, the more hemoglobin is released per damaged cell. Both lead to higher PHb increase rates. To account for this fact, various indices for hemolysis have been introduced. The normalized index of hemolysis (*NIH*) normalizes the damage observed to the hematocrit while the modified index of hemolysis (*MIH*) additionally normalizes to the hemoglobin content.

#### **Measurement errors:**

The determination of PHb requires several centrifugation and pipetting steps, during which additional hemolysis or errors may be introduced. Additional sources of errors are the measurements of hematocrit and total hemoglobin for the determination of *NIH* and *MIH*.

## 6.4 Conclusion

We have identified the potential for improving and standardizing the current hemolysis testing. The challenges of experimental workload, hemoglobin sensing, and reproducibility were discussed. In addition, we have proposed several approaches to address these challenges and collected supporting literature. For hemolysis testing to continue to improve as a valuable research and development tool, we call for consideration and further exploration of the approaches developed here.

First is the replacement of blood in its role as a shear-sensitive fluid by alternative fluids as standardized systems for early assessment of hemocompatibility. However, none of the described approaches is already sufficiently established and there is therefore a need for further characterization of the mechanisms of shear-induced damage in the respective systems.

Second is the continuous and automated monitoring of hemoglobin content in plasma instead of sparse, manual sampling and measurement. Promising technologies have been presented here, but these technologies need to be refined and made commercially available.

Finally, this is a review of the categories and causes of variability in test results. In future studies, it may be used as a structural template and for clarifying their contributions to the issue of reproducibility of hemolysis tests. Further research is to expand the potential of *in vitro* validation by improved and standardized hemolysis testing and will help make the next generation of promising medical devices safer and available sooner.



## 7 Potential factors for poor reproducibility of *in vitro* hemolysis testing

The content of this chapter has been accepted for publication in the *ASAIO Journal* [55]. The execution of the experiments conducted for this study was supported by Seraina Saurenmann and Rick Saner.

### 7.1 Introduction

Along with heart transplantation, implantation of mechanical circulatory assist devices (MCS) is the predominant treatment for end-stage heart failure patients. Despite continuous improvements, therapies with such blood pumps are associated with an increased risk of adverse events [197]. These adverse events are often associated with blood damage resulting from the supraphysiological stress exerted by the devices.

Hemolytic activity induced by mechanical trauma of red blood cells (RBCs) when passing through the pump poses multiple pathological complications associated with release of hemoglobin and potassium ions ( $K^+$ ) from the cells [198]. Transient increase in plasma  $K^+$  may interfere with the heart and brain function [199, 200]. *PHb* damages vascular walls [201], causes vasoconstriction and renal tubule injury. Furthermore, there is evidence that hemolysis contributes to clot formation by blocking von Willebrand factor degradation [202] and activating platelets [203].

Testing hemolysis *in vitro* has become a standard measure to assess the hemolytic potential of devices, for example, during MCS development or to demonstrate device safety before introduction to the market. While the extrapolation of *in vitro* results to *in vivo* outcomes

## 7 Reproducibility of hemolysis testing

is difficult [128], it is useful for relative comparison to established reference devices. The implementation of such tests is described in the ASTM standards F1841 and F1830 [118,139]. It involves blood collection from human or animal donors and a flow- and pressure-controlled recirculation of the blood for several hours through the device being tested.

Despite efforts toward standardization, a low reproducibility of the test results due to inter- and intra-laboratory variance remains a challenge [54,129]. Efforts to address the problem are complicated by the fact that many factors, such as the use of blood from different species and sources or variations in test setups and blood management, can influence hemolysis. As a result, tests must be conducted multiple times to enable robust statistical analyses and, additionally, parallel testing of reference devices is necessary.

The issue of reproducibility has been recognized for more than 20 years. Naito et al. [133] and Mizuguchi et al. [134] advocated the introduction of standardized indices for hemolysis that consider that the amount of released hemoglobin depends on the number of cells that can be damaged, and the amount of hemoglobin released per cell. Mueller et al. [136] published a comprehensive review of factors that may affect the reproducibility of test results. One recommendation by Mueller et al. later adopted by ASTM Standard F1841, is to maintain a physiological level of glucose during testing. This is justified by the dependence of the RBC deformability on glucose availability. However, to our knowledge, no studies have investigated the benefit of this measure to improve the reproducibility of *in vitro* hemolysis tests.

ASTM standard F1841 further specifies that the hematocrit (Ht) of the test blood be adjusted to a standardized level by dilution with phosphate buffered saline (PBS) to reduce inter-donor variability. Sargent et al. [149] have recently raised concerns that this practice is counterproductive because PBS decreases cell stability [204] and that the varying degrees of dilution required thus increase inter-donor variability. They furthermore proposed that the addition of bovine serum albumin (BSA) could protect RBCs against the effect of PBS; however, the results they presented were inconclusive.

A recurrent rationale for the variability among tests repeated with blood from various donors is natural variation of RBC stability [129,

130, 147]. Simple rocker bead tests have been used in attempts to provide a standardizable measure for the RBC stability and to use the results to explain the variability between hemolysis tests. However, the variability of the rocker bead test results was significantly lower than the variability of hemolysis test results, and no correlation was found between the stability assessed in the rocker bead tests and the hemolysis induced by the devices being tested [129, 130]. This lack of correlation suggests that hemolysis test results cannot be calibrated to the donor-specific stability when stability is determined in a different system with deviating flow conditions.

Because the factors contributing to variability in hemolysis tests remain poorly understood, studies are highly laborious and often lead to inconclusive results, slowing down product development and delaying the delivery of better therapies. In this study, we performed repeated generic hemolysis tests on five parallel identical test setups using bovine blood from 23 animals to promote the understanding of factors contributing to variability in hemolysis testing and to identify areas that require further investigation.

Our goals were to investigate (1) the contribution of between- and within-test variability to total variability, (2) the variability in donor and blood characteristics and their implications for between-test variability, (3) changes in blood characteristics during testing and the implications for within-test variability, and (4) the effectiveness of several measures to reduce variability by maintaining glucose levels during testing, adding BSA for RBC protection, and replacing native plasma by washing blood with an artificial plasma.

## 7.2 Material and methods

### 7.2.1 Blood sourcing and ambient conditions

One-liter polyethylene containers were rinsed with 0.9 wt.% sodium chloride solution and prepared with 1.2 mL of heparin solution (6000 IU) to prevent coagulation. Donor animals at the local abattoir (SBZ Schlachtbetrieb Zürich AG, Switzerland) were randomly selected by the attending veterinarian and evaluated as healthy according to the Swiss food standards (VSFK Bundesrat, 2016). Fresh bovine

## 7 Reproducibility of hemolysis testing

blood was gravity collected directly into the containers at exsanguination after severing the neck blood vessels as hemolysis produced during such blood collection does not exceed that obtained after venipuncture using a large-bore needle [152]. Blood was transferred to the laboratory within 30 min and immediately filtered through a nylon mesh (20DEN). Experiments were started no later than 3 hours post-mortem. The average transport temperature was  $20.3 \pm 2.1$  °C with a minimum of 16 °C and a maximum of 23 °C.

### 7.2.2 Blood preparation

Four treatments were applied and compared in this study. First, the benchmark treatment entailed adjusting the  $Ht$  to  $29 \pm 1\%$  using PBS (0.01 M phosphate buffer, 0.0027 M potassium chloride, 0.137 M sodium chloride). Second, by the albumin treatment, 0.1 wt.% of BSA was added to the blood pool. Third, the glucose treatment entailed adjustment of the glucose level to 8 mmol/L at baseline and every 30 min during testing in addition to the benchmark treatment. Fourth, the artificial plasma treatment entailed washing the RBCs three times using a plasma-like buffer (PLB, modification of buffer presented by Makhro et al. [148], 140 mmol/L sodium chloride, 4 mmol/L potassium chloride, 0.8 mmol/L magnesium sulfate, 10 mmol/L glucose, 0.1 wt.% albumin, 20 mmol/L HEPES, 1.2 mmol/L calcium chloride, pH adjusted to 7.4 at 37 °C using imidazole) and adjusting the  $Ht$  to  $29 \pm 1\%$  using PLB. Each washing cycle included a 10 min centrifugation at 10600 g (9000 rpm,  $r = 117$  mm), aspiration of the separated plasma and the white blood cell pellet and resolution of the RBC pellet in PLB.

### 7.2.3 Test setup

The test setup with five identical circulatory flow loops has been previously described [53] and is shown in Figure 7.1. Each loop consists of a CentriMag™ blood pump (Thoratec Switzerland AG (part of Abbott), Zurich, Switzerland) to recirculate the blood and induce hemolysis. In this work, the pump operated at 4050 RPM producing a flow rate of 5.0 L/min at a pressure head of approximately 350 mmHg. A total of

## 7.2 Material and methods

50 cm of polyvinyl chloride tubing connected the pump to a cylindrical polypropylene reservoir (600 mL), which was immersed in a 37 °C water bath. Both the pump inlet and outlet comprised luer-lock connectors to attach pressure transducers (DTXPlusArgon Medical Devices Inc., Frisco, TX, USA). The reservoir was designed to promote blood mixing and to allow pipetting sampling to avoid hemolysis or contamination introduced by sampling through sampling ports. The flow rate was measured on a straight section of the inflow tube using a clamp-on ultrasonic flowmeter (Sonoflow CO.55/120, Sonotec Ultraschallsensorik Halle GmbH, Halle, Germany) regularly calibrated on site with a 40 wt.% glycerol/water mixture. Adjustable pinch clamps were used to change the flow resistance and adjust the flow. The temperature of the entire test setup was monitored using a thermal camera (optris PI 450, Optris GmbH, Berlin, Deutschland). Test loops were rinsed with 0.9 wt.% NaCl solution shortly before each filling with blood. After each experiment, the test loops and pumps were checked for thrombi. Subsequently, the systems were thoroughly cleaned by circulating a 0.1 wt.% sodium dodecyl sulphate solution for several hours before rinsing them with deionized water.

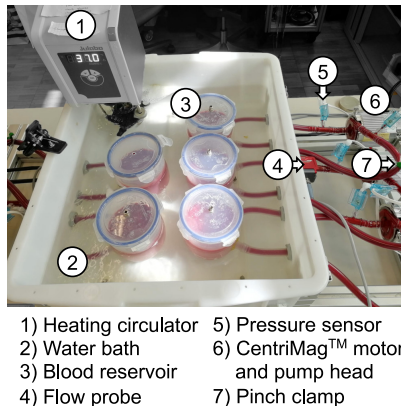


**Figure 7.1:** Overview of the test setup with five identical test loops using CentriMag™ blood pumps.

### 7.2.4 Blood analysis

The  $Ht$  was measured using microcapillary centrifugation for 13 min at 7700 g (9000 rpm,  $r = 85$  mm, Universal 320 & Hematocrit Rotor, Hettich AG, Bach, Switzerland). The  $PHb$  was determined with separated plasma (2x centrifugation at 10 min, 6250 rcf (7000 rpm,  $r = 85$  mm)) with a photometer (Photometer 4040, Robert Riele GmbH & Co. KG, Berlin, Germany) using the Harboe method [119]. The glucose concentration in blood was measured using a glucose meter (Accu-Chek Aviva, Roche Diagnostics, IN, USA). The volume and number of blood cells were determined using a hematology analyzer (Vetscan<sup>®</sup> HM5, Abaxis Inc., Union City, CA, USA). Further blood analysis, including the measurement of blood gases, pH,  $Ht$  as well as ion, glucose, lactate and creatinine concentrations, was performed using an EPOC<sup>®</sup> blood analysis system (Siemens Healthineers AG, Erlangen, Germany). Whole-blood viscosity was determined using a double-gap cylinder measuring system (DG 26.7, Anton Paar, Graz, Austria) on a rotational rheometer (MCR 502, Anton Paar, Graz, Austria). Measurements were performed on a sample volume of 3.6 mL at a temperature of 37 °C at a shear rate of 1000 s<sup>-1</sup>.

### 7.2.5 Study design

A graphical representation of the study design and sampling scheme is given in Figure 7.2. For each hemolysis test, 500 mL of blood was used and circulated in the test loop for 4 hours. For determination of  $PHb$ , 1 mL of blood was taken every 30 min. In addition, a full blood analysis was performed at baseline and end-point, which included measurement of cell volume and number, blood gases, pH, glucose level, and viscosity. Blood from two animals was used per experimental day (12 days). Blood from the first animal was subjected to the benchmark treatment only. Blood from the second animal was subjected to the benchmark, albumin, glucose, and artificial plasma treatments, and a static reference was kept at 37 °C.

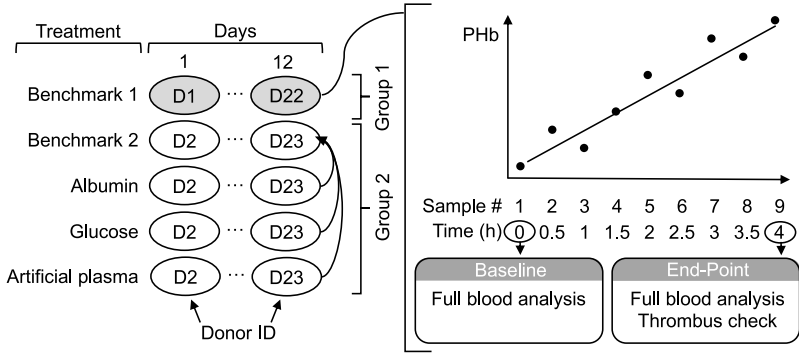


**Figure 7.2:** Overview of the study design showing the allocation of treatments to blood from individual donors over the twelve test days (left) and a sample scheme for blood analysis for a single test day (right). Blood from two animals was used per day; blood from one animal was used for the benchmark treatment only (Benchmark 1), while blood from the other was used for all four treatments. Thus, Benchmark 2 served as reference for the albumin, glucose and artificial plasma treatments.

## 7.2.6 Index of hemolysis

The *NIH* (Equation 7.1) and the *MIH* (Equation 7.2) normalize the rate of *PHb* increase to measures of *Hb* availability, namely *Ht* (%) and total hemoglobin *tHb* (g/dL), as well as blood volume *V* (L) and flow rate *Q* (L/min). The slope of *PHb* increase was determined by linear least-squares regression.

$$NIH(mg/100L) = Slope(PHb(t)) \cdot \frac{100-Ht}{100} \cdot \frac{V}{Q} \quad (7.1)$$

$$MIH(1) = Slope(PHb(t)) \cdot \frac{100-Ht}{100} \cdot \frac{V}{Q} \cdot \frac{1000}{tHb} \quad (7.2)$$

## 7.2.7 Statistical analysis

Statistical analysis was performed using R Statistical Software (version 4.0.3, R Foundation for Statistical Computing, Vienna, Austria) and SPSS Statistics (version 25, IBM, Armonk, NY, USA). Normal

## 7 Reproducibility of hemolysis testing

distribution was evaluated using the Shapiro-Wilk test. Baseline and end-point measurements were compared using a dependent samples t-test, or a Wilcoxon test when the requirements for a dependent samples t-test were not met. Independent groups were compared using an independent sample t-test; a Mann-Whitney U test was used if the requirements for the independent sample t-test were not met. Bivariate and partial linear correlations were tested according to Bravais-Person or using Spearman's rank correlation analysis if the conditions for a Bravais-Person test were not met. Linear mixed-effect models were used to analyze the sources of variance on the standard treatment tests (Equation 7.3) and the effect of the treatments (Equation 7.4). P-values below 0.05 were considered significant. The coefficient of variation (CV) was used as a standardized measure for dispersion of data and calculated as the standard deviation divided by the mean.

$$PHb \sim time + (1|day) + (1 + time|animalID) \quad (7.3)$$

$$PHb \sim time + treatment + (1|day) + (1 + time|animalID) \quad (7.4)$$

## 7.3 Results

Tests were performed with blood from 23 bovine donors. On Day 4, blood from only one animal was used. The increase in hemoglobin over time is shown separately for all twelve test days and different treatments (Figure 7.3). The *PHb*-time slope was extracted for each test series by linear regression and was further analyzed as a measure for hemolysis in each specific test. The assumption of linearity ( $r^2 > 0.95$ ) was found to be valid with few exceptions ( $r^2 < 0.95$ : 4/23 benchmark treatments (both 1 and 2), 1/12 albumin treatment, 2/12 glucose treatment, 4/11 artificial plasma treatment).

### 7.3.1 Sources of variability

A linear mixed-effect model was used to analyze the sources of variability in the *PHb*—time slopes (Equation 7.3). Only data from both



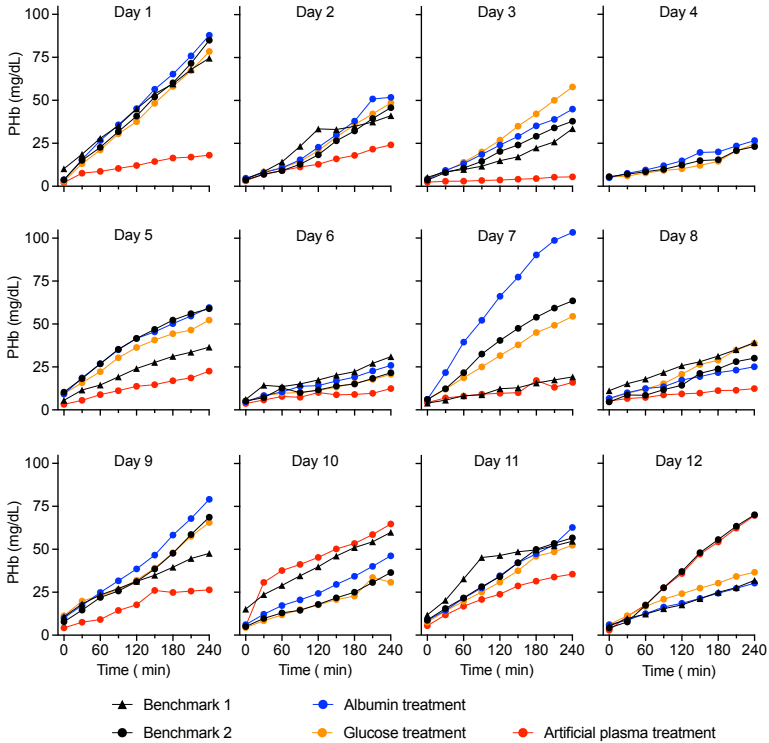


**Figure 7.3:** Increase of plasma hemoglobin (*PHb*) during the 4 hour hemolysis tests plotted separately for all twelve test days and treatments. Please note that no data was available for Benchmark 1 and artificial plasma treatment on Day 4.

benchmark treatment tests was used (23 tests). The other treatments were excluded from this analysis because the treatments themselves introduce between-test variance. The model revealed that the standard deviation (SD) in slope between animals ( $15.50 \text{ mg}/(\text{dL}\cdot 240\text{-min})$ ) was larger than the SD in slope between days ( $9.07 \text{ mg}/(\text{dL}\cdot 240\text{-min})$ ). The residual SD for this model ( $2.35 \text{ mg}/\text{dL}$ ) is a measure of the average deviation from the individual linear models by within-test variability and was small compared to the variability in slope between animals

## 7 Reproducibility of hemolysis testing

or days. A similar result is obtained when the mean within-test  $CV$  (29%) is compared to the between-test  $CV$  (44%). The effect of the test loop on which a test was performed was not significant, indicating that all five loops used in this study caused comparable blood damage and did not add to the variance in hemolysis.

### 7.3.2 Variability in donor and blood characteristics

The donor characteristics (breed, utilization, sex, age and weight) are given in Table 7.1. Animals with blood used only for the Benchmark 1 treatment were assigned to Donor Group 1. Animals with blood used for Benchmark 2, albumin, glucose and artificial plasma treatment were assigned to Donor Group 2. Blood from 23 animals was used (11 female, 12 male). The majority of females was dairy cattle and all males were beef cattle. The mean age was  $32.8 \pm 26.3$  months, while the mean weight was  $310 \pm 43$  kg.

The baseline and end-point blood characteristics, as well as significance tests for differences between them, are shown in Table 7.2. Except for the native hematocrit  $Ht_{native}$  ( $36.75 \pm 4.75\%$ , min. 24%, max. 44%), all blood characteristics were measured after standardizing  $Ht$  with PBS.

### 7.3 Results

**Table 7.1:** Characteristics of the 23 bovine donors (11 female, 12 male) used in this study. Please note that on Day 4 blood from only one animal was collected. (d – dairy, b – beef, du – dual)

Day	Donor Group	Breed	Sex	Age (months)	Weight (kg)
1	1	Braunvieh (d)	female	90.9	337
	2	Holstein (d)	female	46.5	290
2	1	Crossbreed	male	13.7	304
	2	Crossbreed	male	11.3	285
3	1	Limousin (b)	male	14.7	306
	2	Red Holstein (d)	female	74.8	407
4	2	Red Holstein (d)	female	48.5	308
5	1	Crossbreed	male	12.9	310
	2	Simmental (b)	male	13.7	323
6	1	Crossbreed	female	22.3	282
	2	Crossbreed	male	14.5	336
7	1	Simmental (b)	male	13.1	246
	2	Braunvieh (d)	male	12.9	290
8	1	Swiss Fleckvieh (du)	female	92.2	382
	2	Red Holstein (d)	female	58.4	240
9	1	Angus (b)	male	11.5	272
	2	Crossbreed	male	10.7	252
10	1	Charolais (b)	female	47.6	372
	2	Charolais (b)	female	38.9	354
11	1	Holstein (d)	female	33.0	278
	2	Braunvieh (d)	female	48.5	352
12	1	Crossbreed	male	12.3	299
	2	Swiss Fleckvieh (du)	male	12.3	313
Mean ± SD			-	32.8 ± 26.3	310 ± 43

## 7 Reproducibility of hemolysis testing

**Table 7.2:** Summary of blood characteristics at baseline and end-point of all hemolysis tests with both benchmark treatments and significance tests for differences between baseline and end-point measurements.

Parameter (unit)	Baseline (mean±SD)	End-point (mean±SD)	Delta (mean±SD)	N	p	Statistics
Native hematocrit (%)	36.75±4.75	-	-	-	-	-
Adjusted hematocrit (%)	29.04±1.40	-	-	-	-	-
Hemoglobin (g/dL)	8.98±0.53	-	-	-	-	-
Red blood cell count (10 <sup>12</sup> /L)	6.69±0.63	-	-	-	-	-
White blood cell count (10 <sup>9</sup> /L)	7.19±2.94	-	-	-	-	-
Platelet count (10 <sup>9</sup> /L)	106.62±28.68	-	-	-	-	-
Glucose (mmol/L)	3.70±0.77	2.35±0.85	-1.39±0.34	21	0.0001 <sup>t</sup>	0.97
pH	7.37±0.04	7.54±0.08	0.17±0.06	19	0.0001 <sup>t</sup>	0.95
Ca <sup>2+</sup> (mmol/L)	0.93±0.12	0.88±0.10	-0.04±0.02	17	0.0001 <sup>t</sup>	0.90
pCO <sub>2</sub> (kPa)	4.74±0.66	2.28±0.44	-2.46±0.58	19	0.0001 <sup>w</sup>	0.88
pO <sub>2</sub> (kPa)	10.92±7.39	20.22±6.08	9.30±6.21	19	0.0001 <sup>w</sup>	0.88
Plasma hemoglobin (mg/dL)	6.87±3.20	46.39±18.17	39.52±17.37	23	0.0001 <sup>w</sup>	0.88
Lactate (mmol/L)	4.67±1.28	6.57±2.01	1.89±1.32	19	0.0001 <sup>t</sup>	0.83
Mean corpuscular volume (fL)	44.29±4.36	44.76±4.38	0.48±1.03	21	0.0047 <sup>t</sup>	0.43
Cl <sup>-</sup> (mmol/L)	112.32±5.19	113.84±3.70	1.53±3.72	19	0.09 <sup>t</sup>	0.39
K <sup>+</sup> (mmol/L)	5.32±2.37	4.55±2.29	-0.76±2.41	19	0.19 <sup>t</sup>	0.31
Na <sup>+</sup> (mmol/L)	142.95±4.35	144.32±2.11	1.37±4.78	19	0.23 <sup>t</sup>	0.28
Viscosity (1000 s <sup>-1</sup> ) (cP, mPa·s)	2.58±0.37	2.59±0.38	0.01±0.05	21	0.34 <sup>t</sup>	0.21
Creatinine (mg/dL)	1.03±0.21	1.03±0.21	0.06±0.22	18	0.59 <sup>t</sup>	0.13
Plasma protein (g/dL)	4.81±1.47	4.83±1.52	0.02±0.21	23	0.62 <sup>t</sup>	0.11
Mean platelet volume (fL)	6.27±0.49	6.27±0.42	0.00±0.43	21	0.96 <sup>t</sup>	0.01

<sup>t</sup> dependent sample t-test for normally distributed data, <sup>w</sup> Wilcoxon test for non-parametric data

Male donors had higher native *Ht* than female donors (Figure 7.4a, male median = 39.6%, female median = 36%,  $U = 28.000$ ,  $p = 0.005$ ,  $r = 0.54$ ). Male donors were also significantly younger than female donors (Figure 7.4b, male median = 12.9 months, female median = 48.5 months,  $U = 12.000$ ,  $p < 0.0001$ ,  $r = 0.72$ ). There was a negative Spearman rank correlation between age and native *Ht* (Figure 7.4c,  $r_s = -0.530$ ,  $p = 0.006$ ). A nonparametric partial correlation analysis of age and native *Ht* controlling for sex ( $r_s = 0.327$ ,  $p = 0.138$ ) and of sex and native *Ht* controlling for age ( $r_s = -0.598$ ,  $p = 0.003$ ) revealed that the *Ht* difference between donors was due to sex rather than age.

The broad distribution of native *Ht* required a corresponding dilution with different amounts of PBS to standardize the hematocrit. It is reasonable that dilution would lead to a decrease in the concentration of cells and plasma components. Significant correlations between this hematocrit dilution were found with calcium concentration ( $r_s = -0.837$ ,  $p < 0.0001$ ),  $CO_2$  partial pressure ( $r_s = -0.665$ ,  $p = 0.0004$ ), platelet count ( $r_s = -0.523$ ,  $p = 0.0093$ ), protein concentration ( $r_s = -0.801$ ,  $p < 0.0001$ ), and viscosity ( $r_s = -0.770$ ,  $p = 0.0004$ ), as shown in Figure 7.4d-h. In addition, a strong correlation was found between protein concentration and viscosity ( $r_s = 0.933$ ,  $p < 0.0001$ ). The correlation between dilution and viscosity was therefore likely due to a reduction in protein concentrations in plasma.

None of the above blood characteristics correlated with sex when controlling for dilution. However, correlations of sex with RBC volume (mean corpuscular volume, *MCV*) ( $r_s = -0.801$ ,  $p = 0.01$ ) and platelet volume (mean platelet volume (*MPV*)) ( $r_s = -0.626$ ,  $p = 0.022$ ) were found to be significant even when controlling for differences in dilution. The difference in cell sizes between sexes was significant (Mann-Whitney U tests, *MCV*:  $p = 0.0075$ , *MPV*:  $p = 0.0097$ ) and is shown in Figure 7.4j-k. In addition, a positive correlation was found between *MCV* and *MPV* (Figure 7.4l,  $r_s = 0.729$ ,  $p = 0.0008$ ). No correlations were found between individual donor or blood characteristics and susceptibility to hemolysis.

7 Reproducibility of hemolysis testing

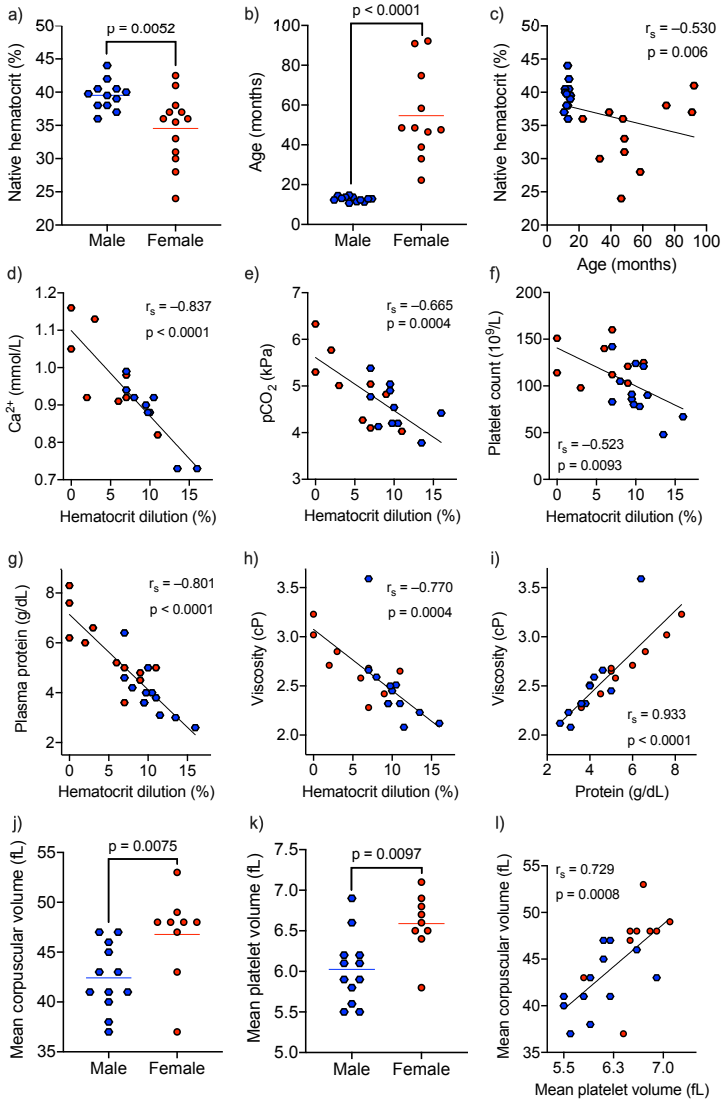


**Figure 7.4:** Analysis of potential factors for within- and between-test variances measured after dilution and remaining significant when controlled for dilution: (a-c) significant sex differences in native hematocrit and age, (d-i) significant changes in blood composition and properties due to hematocrit dilution with PBS, and (j-l) sex differences in red blood cell and platelet size.

### 7.3.3 Changes of blood characteristics during testing

Significant changes in blood properties during testing with the standard treatment pools are listed in Table 7.2 sorted by effect size. Most noticeable was a decrease of glucose by  $1.39 \pm 0.34$  mmol/L, accompanied by an increase in the glucose metabolite lactate by  $1.89 \pm 1.32$  mmol/L. Oxygen partial pressure increased by  $9.30 \pm 6.21$  kPa, indicating an exchange with ambient air. Correspondingly, the CO<sub>2</sub> partial pressure decreased by  $-2.46 \pm 0.58$  kPa, moving toward the low ambient CO<sub>2</sub> partial pressure and causing an increase of pH by  $0.17 \pm 0.06$  units within the bicarbonate buffer system. Alkalosis shifted oxygen dissociation curve of hemoglobin to the left, and contributed to the increase in oxygen saturation due to the Bohr effect. Furthermore, the calcium ion concentration decreased by  $-0.04 \pm 0.02$  mmol/L, while the *MCV* increased by  $0.48 \pm 1.03$  fL. No other correlations of intra-test changes of blood properties with hemolysis were found.

In almost half of all tests (28/58), varying degrees of white, fibrous clot formation were observed (Figure 7.5a-b). We could not determine whether these thrombi formed during testing or during cleaning of the loops. The tests in which clot formation were observed did not show any significantly different hemolysis levels (Figure 7.5c). No test with the artificial plasma treatment showed any clot formation (11 tests).

### 7.3.4 Effect of blood treatments

Artificial plasma treatment significantly reduced blood viscosity by approximately 1 cP (1 mPa·s) compared with the benchmark treatment (Figure 7.6a,  $p < 0.0001$ ). Furthermore, the artificial plasma treatment reduced the variation in viscosity by about 3 %*CV* (Figure 7.6b). Albumin and glucose supplementation of bovine blood in which the Ht was adjusted with PBS had no significant effect on viscosity. However, both albumin and glucose supplementation slightly increased the variation in viscosity between donors.

The effect of the treatment on hemolysis is shown in Figure 7.6c-d. Albumin and glucose treatment had no significant effect on the mean susceptibility of RBCs to pump-induced hemolysis. A slight increase

## 7 Reproducibility of hemolysis testing

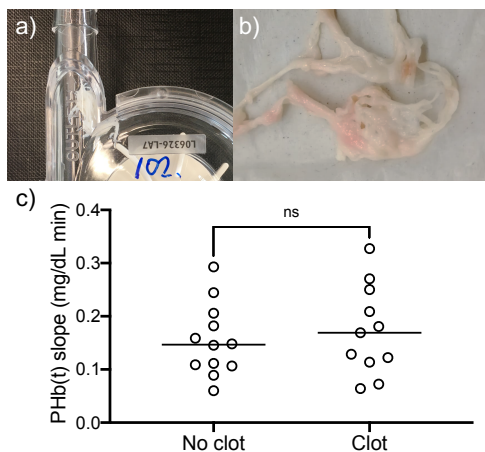


**Figure 7.5:** Exemplary images of a clot formed during the 4 hour hemolysis test (a) caught on the volute tongue of the CentriMag™ pump head and (b) after removal from the pump. (c) Comparison of the hemolysis levels of benchmark tests with and without clot formation.

of +8.5 %CV and slight decrease of -3.9 %CV in between-test variability was seen for the albumin and glucose treatments, respectively. While the artificial plasma treatment led to a reduction in mean *PHb* slope of 0.1 mg/(dL·min), the dispersion of the test results remained at a similarly high level compared to the benchmark treatment. The between-test CV of the artificial plasma treatment was increased substantially, i.e. by +40.6%.

## 7.4 Discussion

As hemolysis tests are subject to limited reproducibility, we performed a hemolysis study with blood from 23 donor animals to identify potential factors for within- and between-test variability as well as to test potential mitigation strategies. The results suggest that inherent differences between animals contributed more to the overall variability (approximately 63%) than differences in blood management



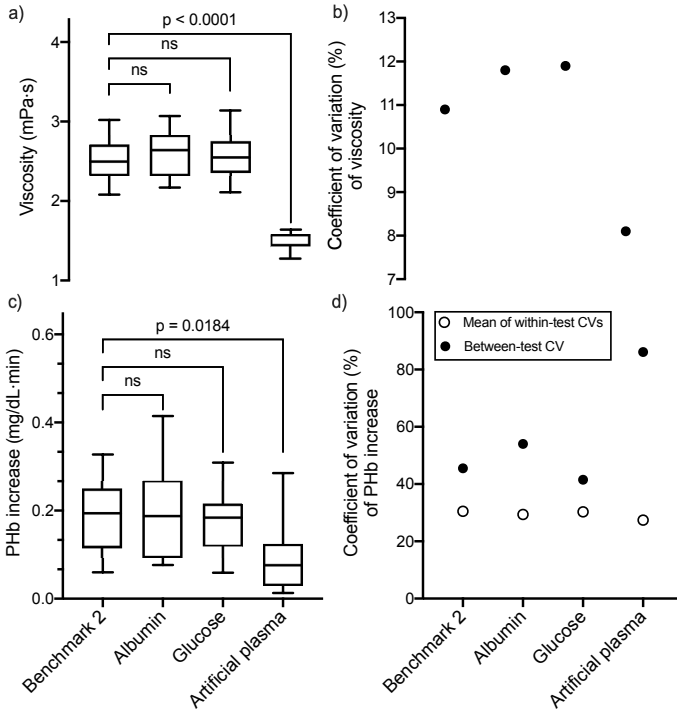


**Figure 7.6:** Comparison of benchmark with the albumin, glucose, and artificial plasma treatments pertaining to mean viscosity and hemolysis and corresponding coefficients of variation (ns, not significant; *PHb*, plasma hemoglobin; *CV*, coefficient of variation).

conditions between test days, possibly caused by transport time or transport temperature (approximately 37%). In comparison, the contribution of within-test variance, for example, by measurement error or changes in RBC stability during the test, was substantially smaller, as also observed by Herbertson et al. [129]. It is, therefore, particularly relevant to investigate what might cause differences in susceptibility to hemolysis between donors.

## 7 Reproducibility of hemolysis testing

Cattle of both sexes were included in this study. Male animals, unlike milk-producing females, are raised for meat production and slaughtered as soon as they reach a certain target weight. Male animals therefore had a significantly lower age and a very narrow age distribution compared to female animals. Differences in hematocrit between sexes as well as between donors of the same sex required varying degrees of dilution with PBS to standardize hematocrit. Although PBS is known to increase the susceptibility of RBC to mechanical load [204], this study did not show any correlation between the degree of dilution and hemolytic activity. However, it was evident that the standardization of hematocrit came at the cost of introducing differences between donors in other blood characteristics. One of these was viscosity, which as a result directly affected the shear forces acting on RBCs. In agreement with the previous findings [149], the results of this study thus give reason to question the common practice of dilution, especially since the effect of hematocrit on test results is usually accounted for by reporting hemolysis as *NIH*, in which the amount of hemoglobin released is normalized to the hematocrit.

None of the factors examined in this study significantly correlated with hemolysis and, by themselves, could explain the variance observed, indicating an interdependence between and counteraction of diverse factors. However, in this study the animals were randomly selected from the abattoir by the attending veterinarian, which resulted in a wide distribution of donor and blood characteristics that are likely to contribute to variability in hemolysis. In previous studies quite a broad range of RBC indices such as Ht, hemoglobin, RBC count and MCV, as well as RBC distribution width used as a marker of inter-cellular heterogeneity were shown for cattle [205–209]. Those depend on the breed, age, sex, lactation, physical activity and diet, exposure to high altitude, time of the year, environmental temperature and other environmental factors [207, 210]. Bulls, for example, have greater RBC counts than cows [211]. Furthermore, beef cattle (to which all bulls and steers included in this study belong) has higher red blood cell counts and Ht than dairy cattle (to which most of the older cows included in this study belong) and lactating dairy cows have a lower Ht than non-lactating dairy cows [211]. Therefore, it seems likely that an improved reproducibility could be achieved by

a careful selection of the donor animals, for example, by choosing a specific farmer, breed, sex, and approximate age, or by repeated blood collections from the same donor during the same season or the year and lactation period. The addition of albumin had no effect on mean hemolysis, and increased the variability compared to the benchmark. The increase in variability could be due to the varying degrees of dilution between tests, as Sargent et al. [149] observed that the addition of albumin either inhibited or promoted hemolysis depending on the amount of PBS added to blood.

While significant differences in baseline glucose concentrations among donors, as well as a significant consumption of glucose were observed during tests, no relationship was found between glucose levels and within- or between-test variability. Maintaining a constant glucose concentration had no effect on mean hemolysis or the variability of test results. While ASTM F1841 recommends maintaining glucose concentration, these results suggest that the related additional workload is not justified.

Artificial plasma treatment resulted in significantly reduced hemolysis. This indicates that RBCs in the PLB medium are less susceptible to mechanical stress than those in PBS-diluted native plasma. Further mitigation of damage may have resulted from the reduction in viscosity and inhibition of clot formation due to the removal of white blood cells, platelets, and plasma proteins by that treatment. This method allows a homogenization of the plasma composition and hematocrit of blood from different donors, and subsequently standardizes viscosity without diminishing RBC stability. Despite this standardization, the variability of the test results was comparable to that of the benchmarks, causing an increase in *CV* due to reduced mean hemolysis. Possible disadvantages of using such RBC suspensions include the elimination of possible RBC interactions with other blood components and the high effort required for their preparation.

## 7.5 Conclusion

This study showed that differences in the susceptibility to hemolysis between blood samples of different donors are the major cause of poor

## 7 Reproducibility of hemolysis testing

reproducibility in *in vitro* hemolysis testing. A comprehensive analysis was conducted on blood samples from 23 animals randomly selected at the local abattoir. Native hematocrit varied strongly between donors; the varying dilution required for hematocrit adjustment artificially introduced between-donor variations of blood properties, such as plasma protein concentration and viscosity.

Furthermore, the analysis showed that the recirculation of blood in hemolysis testing resulted not only in the release of hemoglobin, but in other changes to blood composition, such as a reduction in glucose and an increase in pH due to the release of CO<sub>2</sub>. Three adaptations to the benchmark test protocol were made to test their effects on mean hemolysis and its variability among different donors.

As many interdependent factors can influence hemolysis, no direct correlation of the blood characteristics analyzed or on the adaptations tested with the variability in hemolytic susceptibility could be established. However, it seems likely that a narrower selection of donors, for example, with respect to breed, sex, and age, or the repeated blood collection from the same donor could improve reproducibility. This study contributes to the development of strategies for more efficient *in vitro* validation of ventricular assist devices and prompt further investigations of the potential factors identified in more specifically designed studies.

# 8 Conclusion and Outlook

## 8.1 Conclusion

This thesis has both short-term and long-term implications on the use of AM for making better VADs and accelerating their development.

The first focus was on the potential of AM to enable novel solutions for clinical VAD challenges due to its unique ability to efficiently fabricate complex objects in terms of geometry and composition.

Addressing the need for VAD-integrated sensors for continuous monitoring, AM of titanium was used to fabricate curved microchannels which enabled the integration of pressure and flow measurement capabilities into a VAD inflow cannula. The prototypes measured total pressure and flow rate with the required temporal resolution and precision to resolve the cardiac cycle waveforms. The proof-of-concept for the design concept and its fabrication with AM thus has been achieved. This lays the foundation for additional *in vivo* tests and a further refinement of the design and manufacturing process for future commercialization.

The research described here furthermore explored how of novel AM technologies might enable VAD innovation in the long term. Novel multi-material, voxel-by-voxel AM was applied to build a functional pump prototype that was fully additive-manufactured in one process step. To integrate drive and bearing magnets a printable magnetic polymer compound was developed. Despite the fact that the manufacture of a functional pump was successful, the quality and performance of the device was insufficient for longer operation or for use as a VAD. The magnet printing technology developed, while currently not mature enough for the VAD field, might already be useful in other applications with less strict requirements regarding magnetic properties. As such, it could help to postpone the shift to conventional manu-

## 8 Conclusion and Outlook

facturing methods in the development of products that use magnets. Leveraging the complexity advantage of AM for arbitrary shapes or magnetic gradients this technology might further enable applications with specifically designed magnetic fields.

The second field in the focus of this thesis was the acceleration of VAD development by increasing both prototyping and testing capabilities. Additive manufacturing is an ideal prototyping technology due to cost and lead time advantages in the production of a small number of parts compared to conventional manufacturing. However, due to concerns about insufficient quality of AM parts for functional testing, AM was found to be mainly restricted still to early development phases.

To investigate the applicability of different AM processes for fabrication of polymeric prototypes for functional testing, impellers of a blood pump were fabricated using these processes and their hydraulic and hemolytic properties were tested. Particularly in hemolysis testing, a high surface quality was found to be essential in order to prevent any negative influence on the test results. For the pump and operating conditions investigated, this could only be achieved by the AM process stereolithography. These findings have an immediate value for VAD research and development in that they guide the selection of AM technologies for manufacturing functional prototypes. However, the transfer of the findings presented to other pump systems or operating conditions should be implemented with care. The properties of AM parts not only depend on the AM process, but also on the component's geometry and orientation during manufacture. In addition, the effect of geometric or surface defects not only depends on the size of the defect, but also on local flow fields determined by the operating point and fluid properties. Therefore, an application-specific revalidation of the applicability of AM parts has to be performed in any future study.

In the long-term, VAD development can benefit from rapid prototyping, only if rapid testing is available as well. As discussed in this thesis, hemolysis tests are an essential part of VAD validation and are currently without a viable alternative. However, testing dozens of design variations in a short time is currently infeasible. Therefore,

this thesis contributes both suggestions for the improvement of current practices with short-term applicability as well as a review of more explorative approaches that need to be further investigated. The poor reproducibility of hemolysis tests requires a high number of test repetitions and limits the informative value of results. Hence, this thesis investigated potential factors for poor reproducibility and found that the major causes are differences in the susceptibility to hemolysis between blood of different donors. The findings indicate that a more uniform selection of donors is required and the introduction of additional intra-donor variation has to be avoided, for instance by adjusting the hematocrit to a standard value by hemodilution as required by current standard test protocols. To further simplify hemolysis testing and reduce the workload associated, other approaches have been reviewed, such as the replacement of blood by standardized shear-sensitive fluids and the use of novel sensors for the simplified measurement of hemoglobin concentrations. Although the majority of the technologies involved are not yet mature, in the long-term they should allow a drastic increase in testing throughput and, combined with AM prototyping and computer simulations, enable new development methodologies for faster development of next-generation VADs.

## 8.2 Outlook

The extent of the future use of AM in the VAD field depends on whether key challenges can be successfully addressed. This thesis highlights several domains where further research is necessary. Those are summarized in this section.

The failure rate in the production of pressure-sensing inflow cannulas (Chapter 3) was high at around 50%. However, this was not due to AM of the blank cannula body, but rather to subsequent process steps such as soldering of electronics and sealing the pressure transmission fluid. Addressing these sources of error should be the primary focus in the continued development of the integration of pressure sensor into VADs. Furthermore, the dependence of the signal-to-noise ratio on the flow rate limits the measurement accuracy at low flow rates. This limit

## 8 Conclusion and Outlook

should be addressed in future iterations by increasing the difference in the flow diameters between the points of pressure measurement. An additional limitation of the current concept is its inability to assess the direction of flow. An investigation of whether harmful backflow events can be detected from backflow-specific features from the flow rate or pressure waveform thus should be conducted.

Further attention should also be given to the potential impact of changes in the viscosity and density of the blood that might occur in patients as well as to the effect of more disturbed flow fields that might occur after implantation of the VAD into the LV. Finally, real-time signal readout must be implemented for integration with control algorithms and pump speed control.

In the manufacturing-driven use of AM, the necessary steps are relatively easy to identify. First, the capacity of AM to replace conventional manufacturing must be expanded. For that purpose, the technical challenges of AM relevant to VADs, primarily part accuracy and surface properties, need to be addressed by further developing AM processes and post-processing methods. Those improvements could gradually postpone the transition from AM to conventional manufacturing in later development phases with more stringent requirements. With future high-resolution AM techniques, it may even become possible to engineer surfaces for increased biocompatibility.

In addition, high-throughput test methods are to be developed to match the manufacturing capacity of AM. Short-term efforts should focus on improving the currently low reproducibility of *in vitro* blood tests to reduce the number of test replicates required. The potential factors for the variation in test results identified in this thesis should be further investigated in isolated studies. Potentially more disruptive approaches for improving the assessment of hemolytic activity of pumps were presented in Chapter 6. The feasibility of those ideas should be investigated as well.

Third, new development strategies should be established to effectively leverage the combined prototyping and testing capacity. Such strategies could include the synergetic combination of large-scale *in vitro* tests with increasingly powerful computational development methods. For example, genetic algorithms could be employed that are pro-



vided by *in vitro* test results and that compute improved designs for the next iteration of AM prototypes and *in vitro* testing.

To extend the applicability of AM magnets, future studies should focus on increasing their remanence. One potential approach is to use of anisotropic magnet powders and control the orientation of the magnetic particles during the build process. Another approach could be the AM of polymer-bound green bodies, which are subsequently debonded and sintered to increase the volume fraction of magnetic particles.



# Appendix



# **A Survey on the current use of AM in VADs**

## **A.1 Summary of the survey results**

An online survey was designed to map the current use of AM in the VAD space and to understand how the typical benefits and challenges of AM apply to the VAD niche. It was conducted among twenty individuals involved in VAD development recruited at the Gordon Research Conference on Assisted Circulation 2019 (Castelldefels, Spain) and the conference of the American Society of Artificial Internal Organs 2019 (San Francisco, CA, USA). The survey questionnaire contained both open-ended and close-ended questions on the participants' involvement in VAD development and the VAD development process as well as their institution's interest and engagement in AM. Additionally, the participants were asked to rate the relevance of AM benefits in the field of VADs based on the categories presented in Section 1.3.2. The perceived relevance was rated using the following scores: 2, very relevant; 1, relevant; 0, neutral; -1, irrelevant; -2, very irrelevant. Last, the participants were asked to name circumstances that limit their use of AM. The complete survey is provided below in Section A.2.

All respondents reported being actively involved in developing a VAD, but the majority (17/20) had not yet taken it to market. The average estimate of time to design freeze five years, while a market launch was on average expected ten years after the start of development. Prototyping lead time was reported by 18/20 respondents as a relevant factor for time to market. Likewise, 18/20 respondents rated prototyping costs as a relevant factor for total development costs. More than half of the respondents considered the final product's manufacturing costs to be determinant for the sales price (13/20).

## A Survey: AM in VADs

Eighteen of the participants reported actively using AM. Statements included:

*“Our organization has used 3D printing for about a decade. We have two 3D printers: a fused deposition modelling (FDM) [printer] and a PolyJet printer. We 3D print for R&D purposes on a daily basis.”*

*“We have purchased two 3D printers and they are in almost continuous use. We order 3D-printed parts from external vendors frequently. I believe our use will continue to increase.”*

*“We have and are continuing to explore the possibilities of using 3D printed components in our products. Recent advances in the resolution, accuracy, and surface finish make it a more viable option.”*

Only one respondent reported to be no longer using AM.

*“We try to distance ourselves from 3D-printed parts and transition into injection molded parts.”*

The reported use of AM was strongly focused on early development phases, for example with the purpose of visual design validation or show&tell prototypes for marketing purposes.

*“We use 3D printing for concept design and to get a feel for components and to get a better idea of how components might fit together.”*

*“We are using it if we have time problems or to have a first try of how the parts look and work to each other.”*

*“We have used 3d printed parts in early prototypes purely for visual purpose (not functional).”*

*“We use it as much as is feasible within the tolerance and material constraints of the printed components. Design, testing, anatomic fit,*

## A.1 Summary of the survey results

*assembly method testing, etc.”*

*“Pump prototype parts, sizing models, test setup components, functional prototypes of ancillary tools and components.”*

*“Prototyping for show and tell, e.g., for marketing purposes and usability studies.”*

Some respondents explicitly stated that they had not used AM parts in any functional parts.

*“Very rarely have we used 3D printing for functional prototypes. One exception is a titanium antikink ring that was going to be difficult to manufacture, so we had it printed by direct laser metal sintering.”*

*“[We] use 3D [printing] only for test rigs, but never for final pump and never for blood exposure.”*

Others reported being actively using AM to manufacture functional prototypes for the development and validation of hydraulic characteristics.

*“[We use additive manufacturing for] hydraulic test rigs to test different pump geometries (volute/gaps).”*

*“[We use additive manufacturing for] pump and impeller design, test rig design and modification, prototyping of peripherals, molding, bespoke tools, modelling.”*

Two respondents even reported the use of AM parts in *in vitro* blood testing and *in vivo* testing.

*“[We use additive manufacturing for] rigid steady bodies in contact with blood and in vitro testing. Show and tell prototypes. Feasibility studies.”*

## A Survey: AM in VADs

“[We] use [additive manufactured parts] as functional part. As a solid chamber for the pump. In blood and tissue contact. Subjected to physiological blood pressure.”

Overall, 15/17 respondents reported using AM in the design and prototyping phases, while only three respondents confirmed its use in long-term animal trials. None of the respondents reported the use or intention to use AM parts in clinical trials or final products (Figure A.1). Only about half of the participants reported using additively manufactured components in functional pumps (8/17) as well as with contact to the flow path (10/16) or blood (9/17).

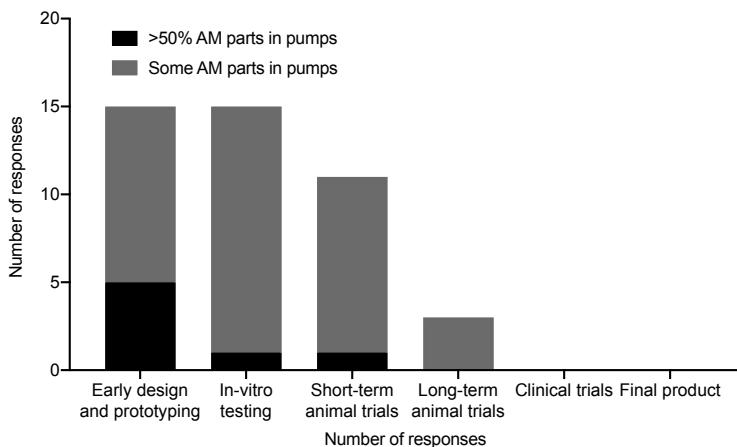


**Figure A.1:** Use of additive manufactured parts in VADs over different development stages based on a survey among twenty individuals involved in the development of VADs.

In line with the reported predominant use of AM in early product development phases, “Prototyping” was the only among the value-adding clusters presented in Section 1.3.2, that was rated close to “very relevant”. The clusters “Production tools”, “Enhanced designs” and “Process concentration” were approximately rated as relevant.



## A.1 Summary of the survey results

“Custom products”, “Improved delivery” and “Incremental product launch” were rated neutral (Figure A.2).

Statements about advances of AM technology required for more extensive use in VADs, focused on technical challenges. A particular concern was insufficient surface quality and related issues with blood exposure:

*“Continued improvement in surface finish, density, and geometrical accuracy.”*

*“3D printed PEEK with fine surface finish would help with blood exposure issues.”*

*“Surface finish, material type, and tolerances are critical, but are all difficult with 3D printing.”*

*“Materials or Processes which guarantee a quality comparable to conventionally manufactured parts.”*

*“Improvements in surface finish, biocompatibility, and precision.”*

*“Better ways to improve surface finish without hand polishing or other labor-intensive methods.”*

Titanium was mentioned several times as a material where a quality improvement and cost reduction of AM would be desirable:

*“Titanium printing at lower cost.”*

*“Cheap, accurate, solid, and fast medical-grade Titanium alloy 3D printing.”*

One respondent mentioned that *“some companies will provide [AM] prototypes but are not prepared to supply [AM] parts [qualified] for implant[ation]”*. This points to the challenge of using new technologies in the highly regulated medical domain and a missing framework for qualifying AM parts for use in final VAD products.

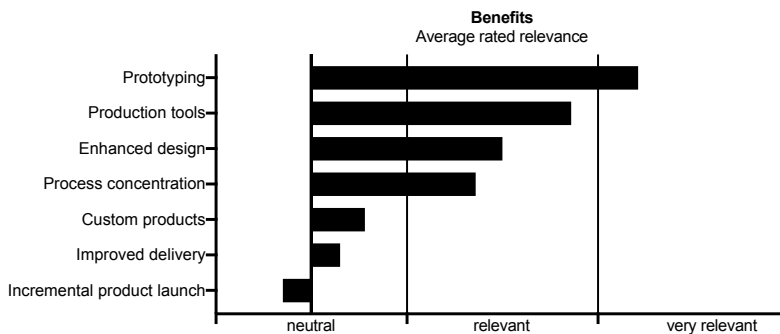


**Figure A.2:** Relevance of different benefits of additive manufacturing in the VAD space rated by twenty individuals involved in the development of VADs.

In summary, the application of AM in the VAD sector is exclusively manufacturing-driven. No respondent reported the function-driven application of AM to achieve product improvement. In addition, the use of AM is strongly limited to early prototyping, which can be attributed to the perception that AM parts are of insufficient quality for later development phases or use in the final product.

## A.2 Questionnaire

Below is the full questionnaire from the survey presented above.

### A.2.1 Questionnaire Section 1 - Background

- In which of the following functional areas in the VAD field are you currently working or have you already worked?
  - Management
  - Research & Development
  - Production
  - Quality engineering and regulator matters
  - Sales & Marketing

- Other, please specify.
- How well is your organization established on the market and what are the R&D efforts?
  - Product(s) on the market and further product development ongoing.
  - Product(s) on the market. No further product development.
  - No product(s) on the market. Development ongoing.
  - No market entry planned. Research only.
  - I do not know / confidential
- How many employees work in your organization?
  - 1 - 20
  - 20 - 100
  - 100 - 1k
  - 1k - 10k
  - <10k
- How many employees in your organization's R&D department work on VADs?
  - 1 - 20
  - 20 - 100
  - 100 - 1k
  - 1k - 10k
  - >10k

## **A.2.2 Questionnaire Section 2 - Product development process**

- Below you will find typical VAD development phases and milestones. Estimate how much time your organization has spent or plans to spend (average for a single product).
  - Design and computer simulation
  - In-vitro testing phase

## *A Survey: AM in VADs*

- Animal trial phase
- Clinical trial phase
- Time to design freeze
- Time to market entry
- Is the time for the production of prototypes and devices (manufacturing lead time) a relevant factor in terms of time to market?
  - Very relevant.
  - Relevant.
  - Neutral.
  - Irrelevant.
  - Very irrelevant.
- Are the manufacturing costs of prototypes and devices a relevant factor in terms of total R&D costs?
  - Very relevant.
  - Relevant.
  - Neutral.
  - Irrelevant.
  - Very irrelevant.
- Are the production costs of the final devices a relevant determinant in terms of selling price?
  - Very relevant.
  - Relevant.
  - Neutral.
  - Irrelevant.
  - Very irrelevant.

### **A.2.3 Questionnaire Section 3 - Interest and engagement in AM**

- To what extent have you already dealt with AM?
  - I am not familiar with any details of AM.

- I know about AM, but do not have detailed knowledge about AM technologies and materials.
- I am familiar with the application of different AM technologies and materials.
- Is your organization interested in or using AM in development and/or production of VAD products?
  - Yes, we are using AM (in product development and/or production).
  - Yes, we are interested in AM and plan to use it in the near future.
  - We have used AM in the past, but are not interested anymore.
  - No, we are not interested in AM.

#### **A.2.4 Section 4 - Application of AM in your organization**

- In which of the following development phases has/is/will your organization used/(be) using AM parts in pumps and to which extent?
  - Design and early prototyping
  - In-vitro testing
  - Short-term animal trials
  - Long-term animal trials
  - Clinical trials
  - Final production in AM.
- What was/is/will (be) the integration level of the AM parts in your organization's pump prototypes and devices?
  - Used in a functional pump
  - Exposed to flow path
  - Exposed to blood

- Please briefly describe and explain how your organization's interest in AM has evolved in the past 5 years. (increasing, declining, purchase of a 3D printer, ...)
- Please briefly describe your organization's application of AM in VAD devices.

### **A.2.5 Questionnaire Section 5 - Benefits and challenges of AM adoption**

- Please read carefully how companies can take advantage of AM in product development and production. Which of these could provide a benefit for an organization in the field of VAD? (very relevant, relevant, neutral, irrelevant, very irrelevant)

#### **Prototyping**

Quick iterations over different designs and concepts for early design validation and faster time to market.

#### **Enhanced, complex designs**

Reduced manufacturing constraints for designing site-specific material properties (e.g. porosity gradient) or direct integration of features (e.g. cooling channels)

#### **Custom products**

Increasing simplicity of manufacturing patient-specific designs.

#### **Process concentration**

Reduction of process steps and manual work such as assembly.

#### **Incremental product launch**

Flexibility to update the design even after selling of the first unit for learning from customer feedback.

#### **Improved delivery**

Cost efficiency for small lot sizes for e.g. a larger variety of products (sizes, types).

**Production tools**

Cost-efficient production of molds or tools for indirect processing.

- Are there other ways your organization can benefit from using AM?
- Please read carefully the general AM challenges companies face. How relevant are those challenges with AM for your organization? (very relevant, relevant, neutral, irrelevant, very irrelevant)

**Technological challenges**, as for example:

- Insufficient material properties, geometrical accuracy or surface quality
- Insufficient longevity
- Unclear or negative effect on hemolysis, thrombogenicity or cytotoxicity.

**Organizational challenges**, as for example:

- Difficulties identifying components where AM could provide a benefit
- Difficulties selecting the right materials and processes
- Unclear integration of AM into existing processes.

**Industrial challenges**, as for example:

- No use for late flexibility through AM, because an early freeze of the design and manufacturing technology is required to start approval process
- Missing regulatory framework for AM in VAD

**Business challenges**, as for example:

- Too little information to estimate the necessary investment and return
- Customer benefit and competitive advantage unclear
- Are there other circumstances that prevent your organization from using AM?





## **B Pressure and Bernoulli-based flow measurement via a tapered inflow VAD cannula**

The following sections provide supporting information for Chapter 3. Sections B.2 and B.3 were provided by the author's collaborator in this project Matthias Dupuch (Laboratory for Micro- and Nanosystems, Department of Mechanical and Process Engineering, ETH Zurich, Zurich, Switzerland).

### **B.1 Manufacturing of cannula blanks**

The cannula blanks were additively manufactured using Ti6Al4V alloy powder (CL 41Ti ELI, Concept Laser GmbH, Lichtenfels, Germany) on an Mlab cusing R selective laser melting (SLM) machine (Concept Laser GmbH, Lichtenfels, Germany). The cannulas were printed along their axis of rotation from the leading to the trailing edge. More detailed machine settings are provided in Table B.1. All faces were recessed from the target by 0.15 mm to compensate for part enlargement introduced by the printing process. Additional offsets and features were added to simplify post-processing of critical surfaces by CNC milling. Those surfaces were the inner conical surface, the interface to the HeartMate3 pump and the soldering pads for the sensor electronics. Residues of metal powder in the microchannels (diameter 0.5 mm) were pushed out with a fine steel wire.

### **B.2 Production of functional cannulas**

Nanostructures to later mechanically anchor the parylene membranes were grown on the surface of the cannulas as described elsewhere [39].

## B

**Table B.1:** Additive manufacturing machine parameters for Ti6Al4V (CL41) on a Mlab cusing R, Concept Laser GmbH, Lichtenfels Germany

Parameter	Power (W)	Laser scanning speed (mm/s)
Support structures	95	900
Areas	95	900
Contours	95	400

Then the cannulas were dip-coated in AZ 4562 photoresist, prebaked for 2 h at 80 °C. Illumination of the membrane-bed was executed in a UV mask aligner (MABA6, Suess Microtec, Garching, Germany), using a polyimide mask and a 45° mirror for 60 seconds and development was done in AZ 400K (1 to 3 parts water) for 2 min 30 sec. After drying, the photoresist was post baked at 110 °C for 2h. The etching of the developed areas was performed in HF (48% Sigma-Aldrich, St. Louis, USA), diluted 1 to 99 parts water. The etching time was not measured starting from submersion of the cannulas, but from the start of the appearance of bubbles on the exposed surface. After 105 second the cannulas were removed from the HF solution and cleaned in 2 Di-Water baths subsequently, before activating the quick-dump-rinser and drying in air. Stripping was executed in acetone for 10 min in an ultrasonication bath and subsequently washed in IPA and DI-Water. The outer side of the ICs was coated with 30 nm Ti, 100 nm Ni, 300 nm Cu, and 150 nm Au for the later soldering step. The access hole to the membrane area (Figure B.1, LDS/SDS hole) was filled by pressing powder sugar into the hole (500 N, 30 s). The cannulas were then coated with Parylene-C (P6 and Parylene-C precursor, Diener Electronic, Ebhausen, Germany) at 0.03 mbar and 40°C resulting in a  $22 \pm 2 \mu\text{m}$  thick layer. After removing unwanted parylene and dissolving the sugar, the membranes were forced to delaminate by applying air pressure at up to 1 bar to the cavity. Preassembled printed circuit boards with a package (P18LCC120S1, Kyocera, Kyoto, Japan) containing a pressure sensor (LPS22HB, STMicroelectronics, Geneva, Switzerland) each were then soldered to the cannulas using a precut In48Sn solder frame (Indalloy 1E, Indium, Clinton, NY, USA) at 150

### B.3 Thermal sensitivity calculation

°C for 10 min. The resulting cavities were filled with silicone oil (Blue-sil 47V50, Elkem, Oslo, Norway) by submersion of the cannulas and application of vacuum. After inserting the cups, the release of excess oil was accelerated by applying pressure on the bloated membranes by inserting a matching cone into the cannula. The sealing was then finished by pressing the balls into the cups. Finally the sensor unit's outer side, including the printed circuit board and connection to the package seat were coated in a layer of medical grade epoxy before filling the sensor seats with silicone.

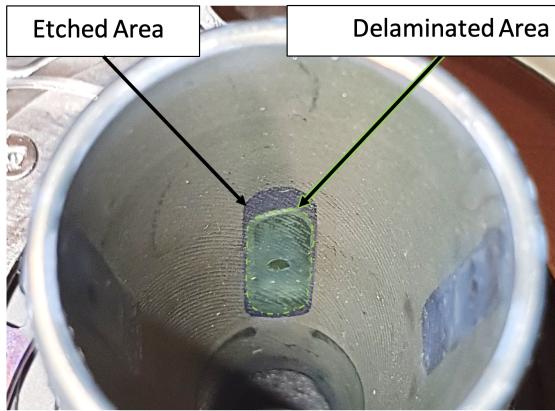


**Figure B.1:** Etched area and area where the membrane delaminated from the membrane bed (green).

### B.3 Thermal sensitivity calculation

For the calculated values, the encapsulated oil volume was extracted from the CAD model and the delaminated membrane length and width was measured on pictures taken in relation to the etched area (Figure B.1). The formula used is based the assumption of two half circles at each end and a straight part in between, which was assumed to deform uniformly. The relation between pressure and center deflection is given by [212] (Figure B.2):

B

$$\Delta p = \left( \frac{16 \cdot y}{3 \cdot h \cdot (1 - \mu^2)} + \frac{(7 - h) \cdot y^3}{3 \cdot h^3 \cdot (1 - \mu)} \right) \cdot \left( h^4 \cdot \frac{E}{r^4} \right) \quad (\text{B.1})$$

The volume under the membrane assuming small deflection is given by:

$$\Delta V = (\pi \cdot r^2 + l \cdot 2 \cdot r) \cdot 0.5 \cdot y \quad (\text{B.2})$$

The additional volume due to thermal expansion of the oil is given by:

$$\Delta V = V_0 \cdot CTE_{oil} \cdot \Delta T \quad (\text{B.3})$$

With

$\Delta p$ : pressure difference between the two sides of the membrane;

$y$ : center deflection of the membrane;

$h$ : thickness of the membrane;

$\mu$ : Poission's ratio;

$E$ : Young's Modulus;

$r$ : radius of the membrane (half the width of the straight part);

$\Delta V$ : the volume under the membrane;

$l$ : length of the straight part;

$V_0$ : volume in the cavity at room temperature;

$CTE_{oil}$ : the volumetric thermal expansion coefficient of silicone oil;

$\Delta T$ : the temperature difference relative to the assembly temperature

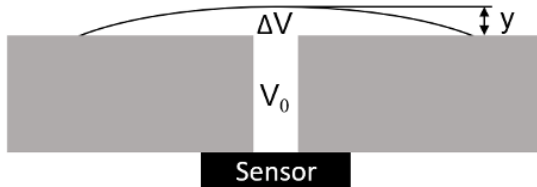


**Figure B.2:** Schematic of a deflected membrane cross section.

## **B.4 Algorithm for extraction of physiological features**

The algorithms implemented to extract features of the pressure and flow waveforms were based on the following principles. These are only suited for postprocessing of simulated physiological data, where the heart rate is known and constant. In the final application other algorithms need to be used to extract those features from live data.

### **End-systolic pressure (ESP)**

Using the known and fixed heart rate of the simulated patient, we manually defined time windows of about 50% of the cardiac cycle around the ESP point. Within those windows the local maximum was extracted and used as ESP.

### **End-diastolic pressure (EDP)**

The extraction of EDP was implemented based on extracted ESPs. The last local minimum between two consecutive ESP points was extracted and used as EDP.

### **Systolic slope (SSL)**

The SSL describes the slope of pressure increase when the heart contracts. The SSL extraction was based on previously extracted ESPs and EDPs. It was calculated by averaging the first derivative of a pressure signal in the time window between  $t_{EDP} + 0.3 \cdot (t_{ESP} - t_{EDP})$  and  $t_{EDP} + 0.7 \cdot (t_{ESP} - t_{EDP})$ .

### **Cardiac cycle averaged flow rate (CAQ)**

The CAQ was determined by averaging the calculated flow rate over one cardiac cycle. The time windows were set manually based on the known and fixed heart rate of the simulated patient.

B

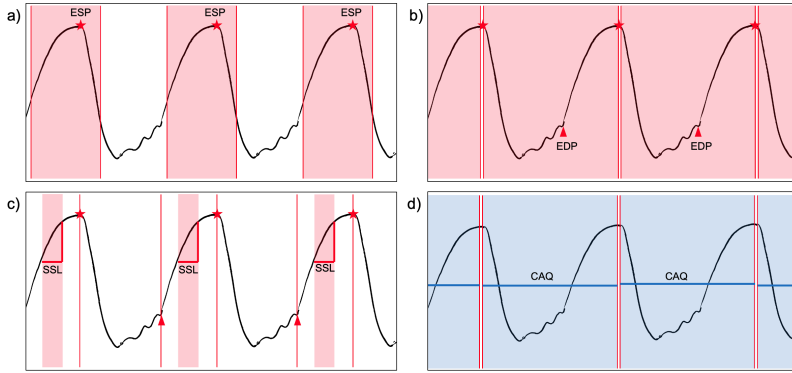


**Figure B.3 :** Schematics of the feature extraction algorithms for end-systolic pressure (a), end-diastolic pressure (b), systolic slope (c) and cardiac cycle averaged flow rate (d).

## B.5 Validity of proposed analytical model

The presented mathematical model used to explain the flow-dependency of pressure measurements at a constant total pressure is based on some simplifications. In the publication it is assumed, that violations of these simplifications only cause small pressure changes compared to the flow-induced pressure changes that are expected according to Bernoulli's principle.

The first assumption is the validity of Bernoulli's principle, which in theory is only valid for inviscid fluid (viscosity of 0 cP) and along streamlines of laminar flow. The first requirement is violated as fluids relevant to the presented application have non-zero viscosity. To estimate if the second requirement of laminar flow is violated the Reynolds number ( $Re$ ) can be used, which helps to predict flow patterns in different fluid flow situations. It can be calculated using the following with the Reynolds number  $Re$ , the density  $\rho$ , the radius of the cannula at the point of sensing  $R$ , the flow velocity  $v$ , the dynamic viscosity  $\mu$  and the flow rate  $Q$ .

$$Re = \frac{\rho \cdot R \cdot v^2}{\mu} = \frac{\rho \cdot Q}{\pi \cdot R \cdot \mu} \quad (\text{B.4})$$

## B.5 Validity of proposed analytical model

**Table B.2:** Reynolds number at different flow rates at the position of the large diameter (LDS) and small diameter sensor (SDS) (Dynamic viscosity  $\mu = 3.5mPa \cdot s$ )

Flow rate Q (L/min)	1	5	10
Reynolds number at LDS (R=7.7 mm)	210	1049	2097
Reynolds number at SDS (R=5.7 mm)	280	1402	2803

At low Reynolds numbers, flows tend to be dominated by laminar flow, while at high Reynolds numbers flows tend to be turbulent. For blood, turbulent flow is expected for a Reynolds number larger than 2000.

Table B.2 shows the Reynolds numbers at the approximate location of the SDS and LDS sensing sites at flow rates between 1 and 10 L/min. It can be seen, that both the SDS and LDS positions the Reynolds number exceeds 2000 at a flow rate of 10 L/min. The assumption of laminar flow, therefore, might be violated at upper end of the flow regime relevant to the presented application. Since both requirements for the application of Bernoulli's equations are violated, the presented model must be considered an approximation and deviations from the ideal behavior are to be expected.

The second assumption is that frictional losses can be neglected. Equation B.5 was, therefore, simplified by removing  $p_{loss}$ .

$$p_{static,transmitted} = p_{total} - p_{dynamic} - p_{loss} \quad (B.5)$$

To determine if this is justified, the following equations are derived to calculate the expected losses and compare them to the approximate dynamic pressures on which the presented sensing concept is based on. Two formulas are available to estimate the expected pressure loss  $\Delta p$  per length  $S$  of a tube with parallel walls. The Hagen-Poiseuille formula is used to estimate pressure losses in laminar flow conditions and the Darcy-Weissbach formula is used in non-laminar flow conditions. These formulas apply to tubes with parallel walls. In following, equations are derived to calculate the pressure loss at specific locations in

B

a tapered tube based on both formulas.

### Hagen-Poiseuille (laminar flow assumption)

The Hagen-Poiseuille formula is:

$$\frac{\Delta p}{S} = \frac{8\mu Q}{\pi} \frac{1}{R^4} := \frac{a_{HP} \cdot Q}{R^4} \quad (\text{B.6})$$

The incremental pressure loss over a tube length  $dz$  is:

$$-dp = \frac{a_{HP} \cdot Q}{R^4} dz \quad (\text{B.7})$$

The taper function of the conical tube and its derivative are:

$$R(z) = \frac{R_L - R_0}{L} \cdot z \quad (\text{B.8})$$

$$\frac{dR(z)}{dz} = \frac{R_L - R_0}{L} := m \quad (\text{B.9})$$

Integrating Equation B.7 using the lubrication approximation (assumption that an increment of a conical tube has parallel walls) and substituting  $dz$  with  $dR$  using the derivative of the taper function

$$\int_{p_S}^{p_{in}} -dp = \frac{a_{HP} \cdot Q}{m} \cdot \int_{R_S}^{R_{in}} \frac{1}{R^4} dR \quad (\text{B.10})$$

results in the pressure loss  $p_{loss,HP}$  from the cannula edge to the sensing position according to

$$p_{loss,HP}(S) = \frac{a_{HP} \cdot Q \cdot S}{3} \left( \frac{1}{R_S^3} - \frac{1}{R_{in}^3} \right) \frac{1}{R_{in} - R_S} \quad (\text{B.11})$$

### Darcy-Weissbach (no laminar flow assumption)

The above derivation can be performed analogously for the Darcy-Weissbach formula, where  $f_D$  is the Darcy friction factor (empirical value of 0.06 in regime  $Re = 2000-4000$ ).



### B.5 Validity of proposed analytical model

$$\frac{\Delta p}{S} = \frac{f_D \cdot \rho \cdot Q^2}{4\pi^2} \frac{1}{R^5} := \frac{a_{DW} \cdot Q^2}{R^5} \quad (\text{B.12})$$

$$-dp = \frac{a_{DW} \cdot Q^2}{R^5} dz \quad (\text{B.13})$$

$$\int_{p_S}^{p_{in}} -dp = \frac{a_{DW} \cdot Q^2}{m} \cdot \int_{R_S}^{R_{in}} \frac{1}{R^5} dR \quad (\text{B.14})$$

$$p_{loss,DW}(S) = \frac{a_{DW} \cdot Q^2 \cdot S}{4} \left( \frac{1}{R_S^4} - \frac{1}{R_{in}^4} \right) \frac{1}{R_{in} - R_S} \quad (\text{B.15})$$

The expected losses are calculated at the SDS and LDS positions for flow rates between 1 - 10 L/min and presented in Table B.3 along with the dynamic pressure on with the sensor concept is based on. The dynamic pressure is calculated using the following equation:

$$\begin{aligned} p_{dynamic} &= \frac{\rho}{2} \cdot v^2 = \frac{\rho}{2} \cdot \left( \frac{Q}{A} \right)^2 \\ &= \frac{\rho \cdot Q^2}{2 \cdot \pi^2} \cdot \frac{1}{R(z)^4} := \frac{a_{dynamic} \cdot Q^2}{R(z)^4} \end{aligned} \quad (\text{B.16})$$

It can be seen, that the pressure losses based on both the Hagen-Poiseuille and the Darcy-Weissbach formulars are small compared to the dynamic pressure. Therefore, it is legitimate to neglect pressure losses in the inflow cannula application.

**Table B.3:** Comparison of dynamic pressure term and pressure loss terms at different flow rates for the large diameter (LDS) and small diameter sensor (SDS)

<b>Flow rate Q (L/min)</b>	<b>1</b>	<b>5</b>	<b>10</b>
$p_{dynamic}$ (LDS/SDS) (mmHg)	0.04/0.12	0.89/3.06	3.56/12.22
$p_{loss,HP}$ (LDS/SDS) (mmHg)	0.00/0.01	0.01/0.04	0.02/0.08
$p_{loss,DW}$ (LDS/SDS) (mmHg)	0.00/0.00	0.02/0.09	0.07/0.34

# **C In vitro testing and comparison of additively manufactured polymer impellers for the CentriMag blood pump**

The following sections provide supporting information for Chapter 5. Section C.2 was provided by the author's collaborator in this project Jonas Abeken (The Interface Group, Institute of Physiology, University of Zurich, Zurich, Switzerland).

## **C.1 Additive manufacturing processes**

All four AM principles used in this study are based on building parts layer-by-layer. Briefly, in selective laser sintering (SLS) a laser fuses the particles of thermoplastic polymer powder by scanning over the cross-section of the printed part in the respective layer. Repeated application of a powder layer and laser scanning leads to the construction of the object. Multi-jet Fusion (MJF) is a combination of SLS with conventional 2D printing. An infrared-absorbing ink is dispensed on thermoplastic polymer powder in the cross-section to be fused. Consequent heating by an infrared energy source fuses the powder particles in the entire cross-section simultaneously. SLS and MJF do not require the use of any support structures. The residual powder is removed from the finished object by sand-blasting. In material jetting (MJ) a printhead dispenses droplets of photosensitive materials that are solidified under UV light in each layer. Materials with different properties can be printed simultaneously, allowing to print a gel-like support material in which the final object is embedded. The support can be removed by water jet. In stereolithography (SLA) an object is created on a build platform that is lowered layer-by-layer into a bath

of a photosensitive resin while a scanning UV laser beam selectively solidifies the resin in the cross-sectional areas. Rod-shaped structures are always needed to connect the part and the build platform. Manual removal of the support rods and sanding at the part-rod interface is needed.

## C.2 Computational fluid dynamics simulation



**Figure C.1:** Overview of the computational fluid domain. Blue: inlet, red: outlet, grey: impeller, translucent: inner wall of housing and extended outflow tubing.

CFD simulations were performed using the STAR-CCM+ software (Siemens, München, Germany). Simulations were conducted on the original pump geometry assuming smooth no-slip walls. The outlet tubing was extended to achieve a developed flow profile at the outlet boundary. As the impeller displacement along the axis of rotation changes with the operating point, it was determined experimentally with Hall sensors and set accordingly for the simulation. An overview of the entire fluid domain is provided in Figure C.1.

Both inlet and outlet were set as pressure boundaries with a prescribed static pressure head of 105 and 350 mmHg, respectively and the impeller motion was implemented using a sliding mesh, rotating at either 2350 rpm or 4050 rpm, reproducing the VAD- and ECMO-like operating conditions, respectively. Blood was modeled as a Newtonian fluid with a density of  $1050 \text{ kg/m}^3$ . The dynamic viscosity was set to 3.5 cP as proposed by the FDA in a study on CFD simulation of blood flow [213]. Unsteady Reynolds-averaged Navier-Stokes equations were solved with a segregated, implicit scheme and second-order accuracy in time and space with convergence criteria set to  $10^{-5}$  for continuity

## C.2 Computational fluid dynamics simulation

and momentum residuals. The flow was modelled as fully turbulent using Menter’s SST k- $\omega$  method [214].

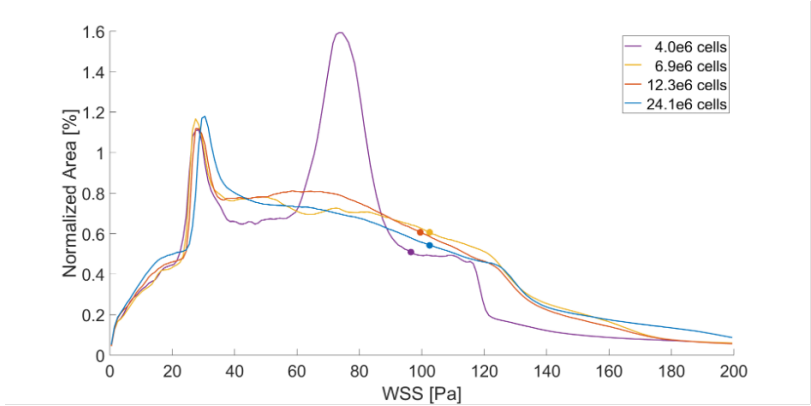


**Figure C.2:** Histogram outlines of WSS on the impeller calculated with computational grids of different sizes. The resulting average WSS are indicated with markers on the respective outlines.

A grid independence study was performed for the ECMO condition including meshes with 4.0, 6.9, 12.3 and 24.1 million cells. Time steps were chosen to achieve an average convective Courant number  $U \cdot \Delta t / \Delta x \approx 1$ , where  $U$  is the local velocity,  $\Delta t$  is the time step and  $\Delta x$  is the cubic root of the cell volume. The resulting time steps for the successively finer grid resolutions corresponded to 4.5, 3, 2 and 1.25 degree of rotation, respectively. Figure C.2 shows the resulting histogram outlines of WSS on the impeller for the different mesh resolutions. The mesh with 12.3 million cells was selected as final grid due to its good agreement with the higher resolution one and its acceptable computational cost. It consisted of polyhedral cells, including 6 to 10 prism layers to achieve  $y^+ \approx 1$  on all surfaces. A representative slice of the mesh is depicted in Figure C.3.

C In vitro validation of additively manufactured impellers

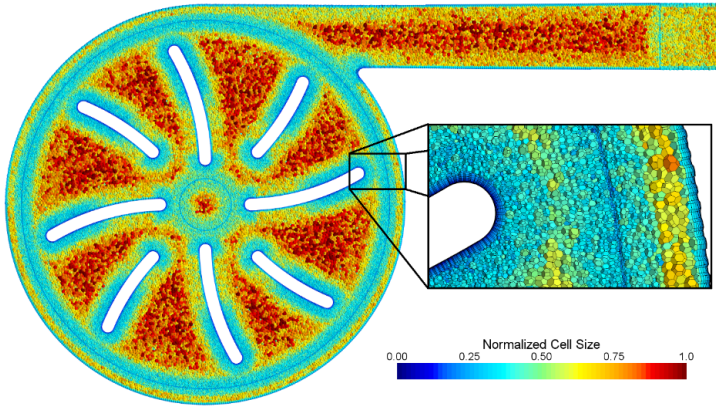


Figure C.3: Cells on slice perpendicular to rotational axis at height of impeller blades. The normalized cell size is computed by the cubic root of the cell volume divided by 0.45 mm, the target cell size of the core mesh.

### C.3 Mock circulatory loop for hydraulic measurements

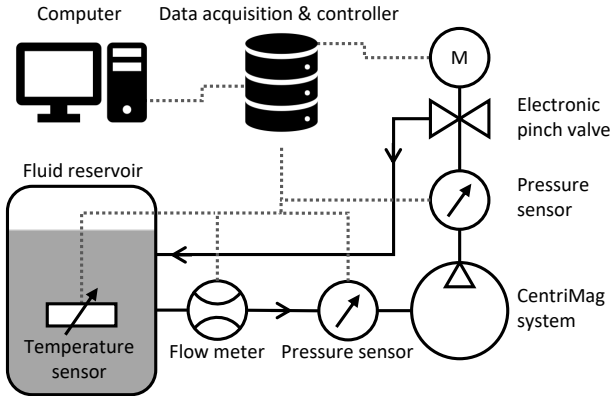


Figure C.4: Schematic of the test bench for hydraulic in vitro testing.

## C.4 Mock circulatory loop for hemolysis measurements

**Table C.1:** Specification of the components of the test bench for hydraulic measurements.

Function	Device	Manufacturer
Flow meter	Sonoflow CO.55/120 clamp-on sensor	Sonotec Ultraschallsensorik Halle GmbH, Halle, Germany
Electronic pinch valve	MPPV-8 valve, DRV-1 step motor drive	Resolution Air, Cincinnati, OH, USA
Temperature sensor	NTC thermistor 500 series	Honeywell, IL, USA
Pressure sensor	Pressure transducer type 528	Huba Controll AG, Würenlos, Switzerland
Data acquisition card	USB 6212	National Instruments, Austin, TX, USA

A schematic of the test bench for hydraulic in vitro testing is shown in Figure C.4. It consists of a computer, a data acquisition card, a motor controller for an electronic pinch valve, pressure sensors at the pump in- and outlet, a flow meter and a temperature sensor for measuring the temperature of the fluid in the reservoir. The CentriMag system again consists of a pump head, a motor and a control unit. The use of data acquisition card and the implementation of the electronic pinch valve enabled the automated acquisition of all sensor data over the entire flow range at fixed pump speeds. Details on the used components are listed in Table C.1.

## C.4 Mock circulatory loop for hemolysis measurements

A schematic of the test bench used for hemolysis testing is shown in Figure C.5. It consists of a blood reservoir immersed in a temperature controlled water bath, a flow meter, pressure sensors at the pump in- and outlet and a manual pinch valve. The CentriMag system consists of a pump head, a motor and a control unit. Details on the used components are listed in Table C.2.

## C In vitro validation of additively manufactured impellers

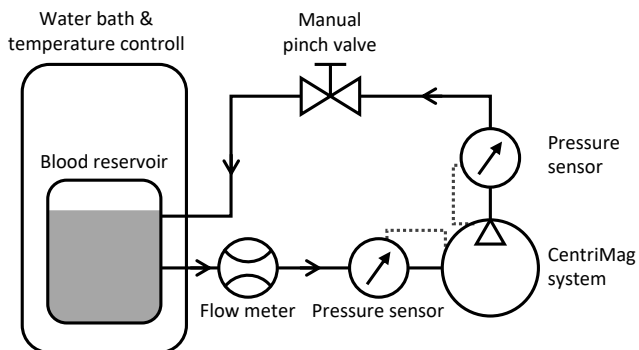


**Figure C.5:** Schematic of the test bench for hemolysis testing.

**Table C.2:** Specification of the components of the test bench for hemolysis measurements.

Function	Device	Manufacturer
Flow meter	Sonoflow CO.55/120 clamp-on sensor	Sonotec Ultraschallsensorik Halle GmbH, Halle, Germany
Pressure sensor	DTXPlus pressure transducers	Argon Medical Devices Inc., Frisco, TX, USA
Temperature control	CORIO C thermostat	Julabo GmbH, Seelbach, Germany



## Bibliography

- [1] P. Ponikowski, S. D. Anker, K. F. AlHabib, M. R. Cowie, T. L. Force, S. Hu, T. Jaarsma, H. Krum, V. Rastogi, L. E. Rohde, U. C. Samal, H. Shimokawa, B. Budi Siswanto, K. Sliwa, and G. Filippatos, “Heart failure: preventing disease and death worldwide,” *ESC Heart Failure*, vol. 1, no. 1, pp. 4–25, 2014.
- [2] A. P. Ambrosy, G. C. Fonarow, J. Butler, O. Chioncel, S. J. Greene, M. Vaduganathan, S. Nodari, C. S. Lam, N. Sato, A. N. Shah, and M. Gheorghiade, “The global health and economic burden of hospitalizations for heart failure: Lessons learned from hospitalized heart failure registries,” *Journal of the American College of Cardiology*, vol. 63, no. 12, pp. 1123–1133, 2014.
- [3] P. A. Heidenreich, N. M. Albert, L. A. Allen, D. A. Bluemke, J. Butler, G. C. Fonarow, J. S. Ikonomidis, O. Khavjou, M. A. Konstam, T. M. Maddox, G. Nichol, M. Pham, I. L. Piña, and J. G. Trogdon, “Forecasting the Impact of Heart Failure in the United States,” *Circulation: Heart Failure*, vol. 6, pp. 606–619, may 2013.
- [4] “International Thoracic Organ Transplant (ITOT) Registry,” <https://ishltregistries.org/registries/>.
- [5] E. J. Molina, P. Shah, M. S. Kiernan, W. K. Cornwell, H. Copeland, K. Takeda, F. G. Fernandez, V. Badhwar, R. H. Habib, J. P. Jacobs, D. Koehl, J. K. Kirklin, F. D. Pagani, and J. A. Cowger, “The Society of Thoracic Surgeons Intermacs 2020 Annual Report,” *The Annals of Thoracic Surgery*, vol. 111, no. 3, pp. 778–792, 2021.
- [6] “HeartMate3 Education Brochure,” <https://www.heartmate.com/>, 2021.

## BIBLIOGRAPHY

- [7] K. D. Aaronson, M. S. Slaughter, L. W. Miller, E. C. McGee, W. G. Cotts, M. A. Acker, M. L. Jessup, I. D. Gregoric, P. Loyalka, O. H. Frazier, V. Jeevanandam, A. S. Anderson, R. L. Kormos, J. J. Teuteberg, W. C. Levy, D. C. Naftel, R. M. Bittman, F. D. Pagani, D. R. Hathaway, and S. W. Boyce, "Use of an intrapericardial, continuous-flow, centrifugal pump in patients awaiting heart transplantation," *Circulation*, vol. 125, no. 25, pp. 3191–3200, 2012.
- [8] J. Baras Shreibati, J. D. Goldhaber-Fiebert, D. Banerjee, D. K. Owens, and M. A. Hlatky, "Cost-Effectiveness of Left Ventricular Assist Devices in Ambulatory Patients With Advanced Heart Failure," *JACC: Heart Failure*, vol. 5, no. 2, pp. 110–119, 2017.
- [9] J. Carlson, "HeartMate 3 gets FDA approval for extended use," <https://apnews.com/article/c3915182c1ad48b0991785fc935eb7f2>, 2018.
- [10] S. G. Moreno, N. Novielli, and N. J. Cooper, "Cost-effectiveness of the implantable HeartMate II left ventricular assist device for patients awaiting heart transplantation," *Journal of Heart and Lung Transplantation*, vol. 31, no. 5, pp. 450–458, 2012.
- [11] C. A. Milano and A. A. Simeone, "Mechanical circulatory support: Devices, outcomes and complications," *Heart Failure Reviews*, vol. 18, pp. 35–53, jan 2013.
- [12] M. Schmid Daners, F. Kaufmann, R. Amacher, G. Ochsner, M. J. Wilhelm, A. Ferrari, E. Mazza, D. Poulidakos, M. Meboldt, and V. Falk, "Left Ventricular Assist Devices: Challenges Toward Sustaining Long-Term Patient Care," *Annals of Biomedical Engineering*, vol. 45, pp. 1836–1851, aug 2017.
- [13] E. L. Wu, M. C. Stevens, J. P. Pauls, and U. Steinseifer, *First-generation ventricular assist devices*, vol. di. Elsevier Inc., 2018.
- [14] M. S. Slaughter, J. G. Rogers, C. A. Milano, S. D. Russell, J. V. Conte, D. Feldman, B. Sun, A. J. Tatoes, R. M. Del-

- gado, J. W. Long, T. C. Wozniak, W. Ghumman, D. J. Farrar, and O. H. Frazier, “Advanced Heart Failure Treated with Continuous-Flow Left Ventricular Assist Device,” *New England Journal of Medicine*, vol. 361, pp. 2241–2251, dec 2009.
- [15] J. F. Gülich, *Kreiselpumpen: ein Handbuch für Entwicklung, Anlagenplaung und Betrieb*. Springer, 2013.
- [16] R. Balasubramanian and S. Bradshaw, “Influence of Impeller Leading Edge Profile on Cavitation and Suction Performance,” *Proceedings of Twenty-Seventh International Pump Users Symposium*, no. March 2012, pp. 34–44, 2011.
- [17] A. P. Yoganathan, K. B. Chandran, and F. Sotiropoulos, “Flow in Prosthetic Heart Valves: State-of-the-Art and Future Directions,” *Annals of Biomedical Engineering*, vol. 33, pp. 1689–1694, dec 2005.
- [18] M. M. Faghieh and M. K. Sharp, “Modeling and prediction of flow-induced hemolysis: a review,” *Biomechanics and Modeling in Mechanobiology*, vol. 18, pp. 845–881, aug 2019.
- [19] K. H. Fraser, T. Zhang, M. E. Taskin, B. P. Griffith, and Z. J. Wu, “A Quantitative Comparison of Mechanical Blood Damage Parameters in Rotary Ventricular Assist Devices: Shear Stress, Exposure Time and Hemolysis Index,” *Journal of Biomechanical Engineering*, vol. 134, p. 081002, aug 2012.
- [20] M. E. Taskin, K. H. Fraser, T. Zhang, C. Wu, B. P. Griffith, and Z. J. Wu, “Evaluation of Eulerian and Lagrangian Models for Hemolysis Estimation,” *ASAIO Journal*, vol. 58, no. 4, pp. 363–372, 2012.
- [21] D. Zimpfer, M. Strueber, P. Aigner, J. D. Schmitto, A. E. Fi-ane, R. Larbalestier, S. Tsui, P. Jansz, A. Simon, S. Schueler, F. Moscato, and H. Schima, “Evaluation of the HeartWare ventricular assist device Lavare cycle in a particle image velocimetry model and in clinical practice,” *European Journal of Cardiothoracic Surgery*, vol. 50, no. 5, pp. 839–848, 2016.

## BIBLIOGRAPHY

- [22] J. J. Teuteberg, J. C. Cleveland, J. Cowger, R. S. Higgins, D. J. Goldstein, M. Keebler, J. K. Kirklin, S. L. Myers, C. T. Salerno, J. Stehlik, F. Fernandez, V. Badhwar, F. D. Pagani, and P. Atluri, “The Society of Thoracic Surgeons Intermacs 2019 Annual Report: The Changing Landscape of Devices and Indications,” *Annals of Thoracic Surgery*, vol. 109, no. 3, pp. 649–660, 2020.
- [23] B. Thamsen, M. Granegger, and U. Kertzscher, “Blood Damage in Ventricular Assist Devices,” *The International Journal of Artificial Organs*, vol. 39, pp. 147–149, apr 2016.
- [24] J. S. Hanke, G. Dogan, A. Zoch, M. Ricklefs, L. Wert, C. Feldmann, C. Bara, M. Shrestha, J. Tillmanns, T. Kempf, J. Bauersachs, A. Haverich, and J. D. Schmitto, “One-year outcomes with the HeartMate 3 left ventricular assist device,” *Journal of Thoracic and Cardiovascular Surgery*, vol. 156, no. 2, pp. 662–669, 2018.
- [25] S. Boës, B. Thamsen, M. Haas, M. S. Daners, M. Meboldt, and M. Granegger, “Hydraulic Characterization of Implantable Rotary Blood Pumps,” *IEEE Transactions on Biomedical Engineering*, vol. 66, pp. 1618–1627, jun 2019.
- [26] L. Wiegmann, S. Boës, D. de Zélicourt, B. Thamsen, M. Schmid Daners, M. Meboldt, and V. Kurtcuoglu, “Blood Pump Design Variations and Their Influence on Hydraulic Performance and Indicators of Hemocompatibility,” *Annals of Biomedical Engineering*, vol. 46, no. 3, pp. 417–428, 2018.
- [27] M. B. Gorbet and M. V. Sefton, *Biomaterial-associated thrombosis: Roles of coagulation factors, complement, platelets and leukocytes*. Woodhead Publishing Limited, 2006.
- [28] E. Potthoff, D. Franco, V. D’Alessandro, C. Starck, V. Falk, T. Zambelli, J. A. Vorholt, D. Poulikakos, and A. Ferrari, “Toward a rational design of surface textures promoting endothelialization,” *Nano Letters*, vol. 14, no. 2, pp. 1069–1079, 2014.

- [29] F. Robotti, D. Franco, L. Bänninger, J. Wyler, C. T. Starck, V. Falk, D. Poulikakos, and A. Ferrari, “The influence of surface micro-structure on endothelialization under suprphysiological wall shear stress,” *Biomaterials*, vol. 35, no. 30, pp. 8479–8486, 2014.
- [30] R. J. Gordon, A. D. Weinberg, F. D. Pagani, M. S. Slaughter, P. S. Pappas, Y. Naka, D. J. Goldstein, W. P. Dembitsky, J. C. Giacalone, J. Ferrante, D. D. Ascheim, A. J. Moskowitz, E. A. Rose, A. C. Gelijns, and F. D. Lowy, “Prospective, multicenter study of ventricular assist device infections,” *Circulation*, vol. 127, no. 6, pp. 691–702, 2013.
- [31] J. MacIver and H. J. Ross, “Quality of life and left ventricular assist device support,” *Circulation*, vol. 126, no. 7, pp. 866–874, 2012.
- [32] A. M. Bernhardt, T. Schlöglhofer, V. Lauenroth, F. Mueller, M. Mueller, A. Schoede, and C. Klopsch, “Prevention and early treatment of driveline infections in ventricular assist device patients – The DESTINE staging proposal and the first standard of care protocol,” *Journal of Critical Care*, vol. 56, pp. 106–112, 2020.
- [33] J. C. Whalen, R. L.; Molokhia, F. A.; Jeffery, D. L.; Huffman, F. N.; Norman, “Current studies with simulated nuclear-powered left ventricular assist devices,” *Transactions - American Society for Artificial Internal Organs*, vol. 18, no. 1, p. 1, 1972.
- [34] “Abbott’s in-development fully implantable heart pump systems earns FDA’s breakthrough devices designation,” <https://abbott.mediaroom.com/>, 2021.
- [35] “Medtronic Receives FDA “Breakthrough Device Designation” for Developing Fully Implantable Heart Pump,” <https://newsroom.medtronic.com/news-releases/news-release-details/medtronic-receives-fda-breakthrough-device-designation-0/>, 2021.

## BIBLIOGRAPHY

- [36] K. Bourque, D. B. Gernes, H. M. Loree, J. Scott Richardson, V. L. Poirier, N. Barletta, A. Fleischli, G. Foiera, T. M. Gempp, R. Schoeb, K. N. Litwak, T. Akimoto, M. J. Watach, and P. Litwak, “HeartMate III: Pump design for a centrifugal LVAD with a magnetically levitated rotor,” *ASAIO Journal*, vol. 47, no. 4, pp. 401–405, 2001.
- [37] A. Petrou, *Intelligent Rotary Blood Pumps with Physiological Response*. Dissertation (no. 25148), ETH Zürich, 2018.
- [38] S. A. Dual, J. M. Zimmermann, J. Neuenschwander, N. H. Cohrs, N. Solowjowa, W. J. Stark, M. Meboldt, and M. Schmid Daners, “Ultrasonic sensor concept to fit a ventricular assist device cannula evaluated using geometrically accurate heart phantoms,” *Artificial Organs*, vol. 43, no. 5, pp. 467–477, 2019.
- [39] S. Staufert and C. Hierold, “Novel Sensor Integration Approach for Blood Pressure Sensing in Ventricular Assist Devices,” *Procedia Engineering*, vol. 168, pp. 71–75, 2016.
- [40] H. Schima, W. Trubel, A. Moritz, G. Wieselthaler, H. G. Stohr, H. Thoma, U. Losert, and E. Wolner, “Noninvasive Monitoring of Rotary Blood Pumps: Necessity, Possibilities, and Limitations,” *Artificial Organs*, vol. 16, no. 2, pp. 195–202, 1992.
- [41] A. H. H. Alomari, A. V. Savkin, M. Stevens, D. G. Mason, D. L. Timms, R. F. Salamonsen, and N. H. Lovell, “Developments in control systems for rotary left ventricular assist devices for heart failure patients: A review,” *Physiological Measurement*, vol. 34, no. 1, 2013.
- [42] K. Reesink, A. Dekker, T. Van Der Nagel, C. Beghi, F. Leonardi, P. Botti, G. De Cicco, R. Lorusso, F. Van Der Veen, and J. Maessen, “Suction due to left ventricular assist: Implications for device control and management,” *Artificial Organs*, vol. 31, no. 7, pp. 542–549, 2007.
- [43] A. Petrou, J. Lee, S. Dual, G. Ochsner, M. Meboldt, and M. Schmid Daners, “Standardized Comparison of Selected Phys-

- iological Controllers for Rotary Blood Pumps: In Vitro Study,” *Artificial Organs*, vol. 42, no. 3, pp. E29–E42, 2018.
- [44] L. Wiegmann, B. Thamsen, D. de Zélicourt, M. Granegger, S. Boès, M. Schmid Daners, M. Meboldt, and V. Kurtcuoglu, “Fluid Dynamics in the HeartMate 3: Influence of the Artificial Pulse Feature and Residual Cardiac Pulsation,” *Artificial Organs*, vol. 43, no. 4, pp. 363–376, 2019.
- [45] M. Granegger, B. Thamsen, T. Schlöglhofer, S. Lach, A. Escher, T. Haas, M. Meboldt, M. Schweiger, M. Hübler, and D. Zimpfer, “Blood trauma potential of the HeartWare Ventricular Assist Device in pediatric patients,” *The Journal of Thoracic and Cardiovascular Surgery*, vol. 159, pp. 1519–1527.e1, apr 2020.
- [46] H. Proff and A. Staffen, “Challenges of Additive Manufacturing Why companies don’t use Additive Manufacturing in serial production,” *Deloitte*, pp. 24–25, 2019.
- [47] B. Burke and P. Basiliere, “An enterprise architect’s best practices for 3D printing,” *Gartner Research*, 2015.
- [48] F. Fontana, C. Klahn, and M. Meboldt, “Value-driven clustering of industrial additive manufacturing applications,” *Journal of Manufacturing Technology Management*, vol. 30, no. 2, pp. 366–390, 2019.
- [49] D. Lehmus, C. Aumund-Kopp, F. Petzoldt, D. Godlinski, A. Haberkorn, V. Zöllmer, and M. Busse, “Customized Smartness: A Survey on Links between Additive Manufacturing and Sensor Integration,” *Procedia Technology*, vol. 26, pp. 284–301, 2016.
- [50] S. Staufert, P. Gutzwiller, F. Mushtaq, and C. Hierold, “Surface Nanostructuring of Ti6Al4 v Surfaces for Parylene-C Coatings with Ultradurable Adhesion,” *ACS Applied Nano Materials*, vol. 1, pp. 1586–1594, apr 2018.
- [51] K. von Petersdorff-Campen, M. Dupuch, C. Hierold, M. Meboldt, and M. Schmid Daners, “Pressure and Bernoulli-based flow measurement via a tapered inflow VAD cannula,”

## BIBLIOGRAPHY

- IEEE Transactions on Biomedical Engineering (under review)*, 2021.
- [52] K. von Petersdorff-Campen, Y. Hauswirth, J. Carpenter, A. Hagmann, S. Boës, M. Schmid Daners, D. Penner, and M. Meboldt, “3D Printing of Functional Assemblies with Integrated Polymer-Bonded Magnets Demonstrated with a Prototype of a Rotary Blood Pump,” *Applied Sciences*, vol. 8, p. 1275, aug 2018.
- [53] K. von Petersdorff-Campen, J. Abeken, D. de Zélicourt, V. Kurtcuoglu, M. Meboldt, and M. Schmid Daners, “In Vitro Testing and Comparison of Additively Manufactured Polymer Impellers for the CentriMag Blood Pump,” *ASAIO Journal*, vol. 67, pp. 306–313, mar 2021.
- [54] K. von Petersdorff-Campen and M. Schmid Daners, “Hemolysis Testing In Vitro: A Review of Challenges and Potential Improvements,” *ASAIO Journal (online first)*, may 2021.
- [55] K. von Petersdorff-Campen, P. Fischer, A. Bogdanova, and M. Schmid Daners, “Potential factors for poor reproducibility of in vitro hemolysis testing,” *ASAIO Journal (accepted for publication)*, 2021.
- [56] J. K. Kirklin, R. Cantor, P. Mohacsi, J. Gummert, T. De By, M. M. Hannan, R. L. Kormos, S. Schueler, L. H. Lund, T. Nakatani, R. Taylor, and J. Lannon, “First Annual IMACS Report: A global International Society for Heart and Lung Transplantation Registry for Mechanical Circulatory Support,” *Journal of Heart and Lung Transplantation*, vol. 35, no. 4, pp. 407–412, 2016.
- [57] C. A. Theochari, G. Michalopoulos, E. K. Oikonomou, S. Giannopoulos, I. P. Doulamis, M. Alvarez Villela, and D. G. Kokkinidis, “Heart transplantation versus left ventricular assist devices as destination therapy or bridge to transplantation for 1-year mortality: A systematic review and meta-analysis,” *Annals of Cardiothoracic Surgery*, vol. 7, no. 1, pp. 3–11, 2018.



- [58] J. J. Han, M. A. Acker, and P. Atluri, “Left ventricular assist devices synergistic model between technology and medicine,” *Circulation*, vol. 138, no. 24, pp. 2841–2851, 2018.
- [59] J. K. Kirklin, F. D. Pagani, R. L. Kormos, L. W. Stevenson, E. D. Blume, S. L. Myers, M. A. Miller, J. T. Baldwin, J. B. Young, and D. C. Naftel, “Eighth annual INTERMACS report: Special focus on framing the impact of adverse events,” *Journal of Heart and Lung Transplantation*, vol. 36, no. 10, pp. 1080–1086, 2017.
- [60] M. Mansouri, R. F. Salamonsen, E. Lim, R. Akmeliawati, and N. H. Lovell, “Preload-based starling-like control for rotary blood pumps: Numerical comparison with pulsatility control and constant speed operation,” *PLoS ONE*, vol. 10, no. 4, pp. 1–16, 2015.
- [61] A. Petrou, M. Monn, M. Meboldt, and M. Schmid Daners, “A Novel Multi-objective Physiological Control System for Rotary Left Ventricular Assist Devices,” *Annals of Biomedical Engineering*, pp. 1–12, 2017.
- [62] E. Bullister, S. Reich, and J. Shuetz, “Physiologic control algorithms for rotary blood pumps using pressure sensor input,” *Artificial Organs*, vol. 26, no. 11, pp. 931–938, 2002.
- [63] G. Ochsner, R. Amacher, M. J. Wilhelm, S. Vandenberghe, H. Tevaearai, A. Plass, A. Amstutz, V. Falk, and M. Schmid Daners, “A Physiological Controller for Turbodynamic Ventricular Assist Devices Based on a Measurement of the Left Ventricular Volume,” *Artificial Organs*, vol. 38, no. 7, pp. 527–538, 2014.
- [64] M. Vollkron, H. Schima, L. Huber, R. Benkowski, G. Morello, and G. Wieselthaler, “Development of a reliable automatic speed control system for rotary blood pumps,” *Journal of Heart and Lung Transplantation*, vol. 24, no. 11, pp. 1878–1885, 2005.
- [65] K. Ohuchi, D. Kikugawa, K. Takahashi, M. Uemura, M. Nakamura, T. Murakami, T. Sakamoto, and S. Takatani, “Control

## BIBLIOGRAPHY

- strategy for rotary blood pumps,” *Artificial Organs*, vol. 25, no. 5, pp. 366–370, 2001.
- [66] Y. Wu, P. E. Allaire, G. Tao, M. Adams, Y. Liu, H. G. Wood, and D. B. Olsen, “A bridge from short-term to long-term left ventricular assist device - Experimental verification of a physiological controller,” *Artificial Organs*, vol. 28, no. 10, pp. 927–932, 2004.
- [67] Y. Wu, P. E. Allaire, G. Tao, and D. Olsen, “Modeling, estimation, and control of human circulatory system with a left ventricular assist device,” *IEEE Transactions on Control Systems Technology*, vol. 15, no. 4, pp. 754–767, 2007.
- [68] M. Guglin, B. George, S. Branam, and A. Hart, “CardioMEMSTM in LVAD Patients: A Case Series,” *The VAD Journal*, pp. 1–6, 2016.
- [69] M. Granegger, F. Moscato, F. Casas, G. Wieselthaler, and H. Schima, “Development of a pump flow estimator for rotary blood pumps to enhance monitoring of ventricular function,” *Artificial Organs*, vol. 36, no. 8, pp. 691–699, 2012.
- [70] N. Malagutti, D. M. Karantonis, S. L. Cloherty, P. J. Ayre, D. G. Mason, R. F. Salamonsen, and N. H. Lovell, “Noninvasive average flow estimation for an implantable rotary blood pump: A new algorithm incorporating the role of blood viscosity,” *Artificial Organs*, vol. 31, no. 1, pp. 45–52, 2007.
- [71] A. Funakubo, S. Ahmed, I. Sakuma, and Y. Fukui, “Flow rate and pressure head estimation in a centrifugal blood pump,” *Artificial Organs*, vol. 26, no. 11, pp. 985–990, 2002.
- [72] D. Rüschen, M. Rimke, J. Gesenhues, S. Leonhardt, and M. Walter, “Online cardiac output estimation during transvalvular left ventricular assistance,” *Computer Methods and Programs in Biomedicine*, vol. 171, pp. 87–97, 2019.
- [73] A. Petrou, M. Kanakis, K. Magkoutas, B. De Vries, M. Meboldt, and M. Schmiddaners, “Cardiac Output Estimation: Online Implementation for Left Ventricular Assist Device Support,” *IEEE*

- Transactions on Biomedical Engineering*, vol. 9294, no. c, pp. 1–10, 2020.
- [74] E. Bullister, S. Reich, P. D’Entremont, N. Silverman, and J. Sluetz, “A blood pressure sensor for long-term implantation,” *Artificial Organs*, vol. 25, no. 5, pp. 376–379, 2001.
- [75] B. Fritz, J. Cysyk, R. Newswanger, W. Weiss, and G. Rosenberg, “Development of an Inlet Pressure Sensor for Control in a Left Ventricular Assist Device,” *ASAIO Journal*, vol. 56, pp. 180–185, may 2010.
- [76] A. F. Stephens, A. Busch, R. F. Salamonsen, S. D. Gregory, and G. D. Tansley, “A novel fibre Bragg grating pressure sensor for rotary ventricular assist devices,” *Sensors and Actuators, A: Physical*, vol. 295, pp. 474–482, 2019.
- [77] I. Saito, T. Chinzei, T. Isoyama, H. Miura, A. Kouno, T. Ono, H. Nakagawa, S. Yamaguchi-Sekine, W. Shi, Y. Inoue, A. Kishi, and Y. Abe, “Implementation of the natural heartbeat synchronize control for the undulation pump ventricular assist device using the inflow pressure,” *IFMBE Proceedings*, vol. 19 IFMBE, no. January 2016, pp. 62–65, 2008.
- [78] W. Shi, I. Saito, T. Chinzei, T. Isoyama, H. Miura, A. Kouno, T. Ono, H. Nakagawa, S. Yamaguchi, Y. Inoue, A. Kishi, and Y. Abe, “Development of an auto calibration method for the implantable blood pressure sensor in the undulation pump ventricular assist device (UPVAD),” *IFMBE Proceedings*, vol. 19 IFMBE, pp. 66–69, 2008.
- [79] L. Brancato, G. Keulemans, T. Verbelen, B. Meyns, and R. Puers, “An implantable intravascular pressure sensor for a ventricular assist device,” *Micromachines*, vol. 7, no. 8, pp. 1–17, 2016.
- [80] M. D. Zhou, C. Yang, Z. Liu, J. P. Cysyk, and S. Y. Zheng, “An implantable Fabry-Pérot pressure sensor fabricated on left ventricular assist device for heart failure,” *Biomedical Microdevices*, vol. 14, no. 1, pp. 235–245, 2012.

## BIBLIOGRAPHY

- [81] G. Ochsner, R. Amacher, A. Amstutz, A. Plass, M. Schmid Daners, H. Tevaearai, S. Vandenberghe, M. J. Wilhelm, and L. Guzzella, “A Novel Interface for Hybrid Mock Circulations to Evaluate Ventricular Assist Devices,” *IEEE Transactions on Biomedical Engineering*, vol. 60, pp. 507–516, feb 2013.
- [82] S. Liao, M. Neidlin, Z. Li, B. Simpson, and S. D. Gregory, “Ventricular flow dynamics with varying LVAD inflow cannula lengths: In-silico evaluation in a multiscale model,” *Journal of Biomechanics*, vol. 72, pp. 106–115, 2018.
- [83] F. M. Colacino, F. Moscato, F. Piedimonte, G. Danieli, S. Nicosia, and M. Arabia, “A modified elastance model to control mock ventricles in real-time: Numerical and experimental validation,” *ASAIO Journal*, vol. 54, no. 6, pp. 563–573, 2008.
- [84] T. Kenner, “The measurement of blood density and its meaning,” *Basic Research in Cardiology*, vol. 84, no. 2, pp. 111–124, 1989.
- [85] D. Rüschen, M. Rimke, J. Gesenhues, S. Leonhardt, and M. Walter, “Continuous cardiac output estimation under left ventricular assistance,” *IFAC-PapersOnLine*, vol. 28, no. 20, pp. 569–574, 2015.
- [86] C. Reyes, N. Voskoboynikov, K. Chorpenning, J. A. LaRose, M. C. Brown, N. J. Nunez, D. Burkhoff, and D. Tamez, “Accuracy of the HVAD pump flow estimation algorithm,” *ASAIO Journal*, vol. 62, no. 1, pp. 15–19, 2016.
- [87] J. A. Potkay, “Long term, implantable blood pressure monitoring systems,” *Biomedical Microdevices*, vol. 10, no. 3, pp. 379–392, 2008.
- [88] W. T. Abraham, P. B. Adamson, A. Hasan, R. C. Bourge, S. V. Pamboukian, M. F. Aaron, and N. Y. Raval, “Safety and accuracy of a wireless pulmonary artery pressure monitoring system in patients with heart failure,” *American Heart Journal*, vol. 161, no. 3, pp. 558–566, 2011.

- [89] M. C. Stevens, N. R. Gaddum, M. Pearcy, R. F. Salamonsen, D. L. Timms, D. G. Mason, and J. F. Fraser, “Frank-starling control of a left ventricular assist device,” *Proceedings of the Annual International Conference of the IEEE Engineering in Medicine and Biology Society, EMBS*, pp. 1335–1338, 2011.
- [90] D. Burkhoff, I. Mirsky, and H. Suga, “Assessment of systolic and diastolic ventricular properties via pressure-volume analysis: A guide for clinical, translational, and basic researchers,” *American Journal of Physiology - Heart and Circulatory Physiology*, vol. 289, no. 2 58-2, 2005.
- [91] D. Brown, B.-M. Ma, and Z. Chen, “Developments in the processing and properties of NdFeb-type permanent magnets,” *Journal of Magnetism and Magnetic Materials*, vol. 248, pp. 432–440, aug 2002.
- [92] L. Li, A. Tirado, I. C. Nlebedim, O. Rios, B. Post, V. Kunc, R. R. Lowden, E. Lara-Curzio, R. Fredette, J. Ormerod, T. A. Lograsso, and M. P. Paranthaman, “Big Area Additive Manufacturing of High Performance Bonded NdFeB Magnets,” *Scientific Reports*, vol. 6, no. 1, 2016.
- [93] C. Huber, C. Abert, F. Bruckner, C. Pfaff, J. Kriwet, M. Groenefeld, I. Teliban, C. Vogler, and D. Suess, “Topology optimized and 3D printed polymer-bonded permanent magnets for a predefined external field,” *Journal of Applied Physics*, vol. 122, p. 53904, aug 2017.
- [94] C. Huber, C. Abert, F. Bruckner, M. Groenefeld, S. Schuschnigg, I. Teliban, C. Vogler, G. Wautischer, R. Windl, and D. Suess, “3D Printing of Polymer-Bonded Rare-Earth Magnets with a Variable Magnetic Compound Fraction for a Predefined Stray Field,” *Scientific Reports*, vol. 7, no. 1, 2017.
- [95] J. Jaćimović, F. Binda, L. G. Herrmann, F. Greuter, J. Genta, M. Calvo, T. Tomše, and R. A. Simon, “Net Shape 3D Printed NdFeB Permanent Magnet,” *Advanced Engineering Materials*, vol. 19, p. 1700098, aug 2017.

## BIBLIOGRAPHY

- [96] M. P. Paranthaman, C. S. Shafer, A. M. Elliott, D. H. Siddel, M. A. McGuire, R. M. Springfield, J. Martin, R. Fredette, and J. Ormerod, “Binder Jetting: A Novel NdFeB Bonded Magnet Fabrication Process,” *JOM*, vol. 68, pp. 1978–1982, jul 2016.
- [97] Y. Yan, L. Liu, C. Ding, L. Nguyen, J. Moss, Y. Mei, and G.-Q. Lu, “Additive Manufacturing of Magnetic Components for Heterogeneous Integration,” in *2017 IEEE 67th Electronic Components and Technology Conference (ECTC)*, pp. 324–330, IEEE, may 2017.
- [98] B. G. Compton, J. W. Kemp, T. V. Novikov, R. C. Pack, C. I. Nlebedim, C. E. Duty, O. Rios, and M. P. Paranthaman, “Direct-write 3D printing of NdFeB bonded magnets,” *Materials and Manufacturing Processes*, vol. 33, pp. 109–113, jan 2018.
- [99] L. Li, K. Jones, B. Sales, J. L. Pries, I. Nlebedim, K. Jin, H. Bei, B. K. Post, M. S. Kesler, O. Rios, V. Kunc, R. Fredette, J. Ormerod, A. Williams, T. A. Lograsso, and M. P. Paranthaman, “Fabrication of highly dense isotropic Nd-Fe-B nylon bonded magnets via extrusion-based additive manufacturing,” *Additive Manufacturing*, vol. 21, pp. 495–500, may 2018.
- [100] E. M. Schumer, M. C. Black, G. Monreal, and M. S. Slaughter, “Left ventricular assist devices: Current controversies and future directions,” *European Heart Journal*, vol. 37, no. 46, pp. 3434–3439b, 2016.
- [101] M. Nishida, T. Negishi, D. Sakota, R. Kosaka, O. Maruyama, T. Hyakutake, K. Kuwana, and T. Yamane, “Properties of a monopivot centrifugal blood pump manufactured by 3D printing,” *Journal of Artificial Organs*, vol. 19, pp. 322–329, dec 2016.
- [102] A. L. Throckmorton, J. Y. Kapadia, S. G. Chopski, S. S. Bhavsar, W. B. Moskowitz, S. D. Gullquist, J. J. Gangemi, C. M. Haggerty, and A. P. Yoganathan, “Numerical, Hydraulic, and Hemolytic Evaluation of an Intravascular Axial Flow Blood Pump to Mechanically Support Fontan Patients,” *Annals of Biomedical Engineering*, vol. 39, pp. 324–336, jan 2011.

- [103] W. K. Chan, Y. W. Wong, C. K. Chua, C. W. Lee, and C. Feng, “Rapid manufacturing techniques in the development of an axial blood pump impeller,” *Proceedings of the Institution of Mechanical Engineers, Part H: Journal of Engineering in Medicine*, vol. 217, pp. 469–475, jun 2003.
- [104] A. Lalehpour and A. Barari, “Post processing for Fused Deposition Modeling Parts with Acetone Vapour Bath,” *IFAC-PapersOnLine*, vol. 49, no. 31, pp. 42–48, 2016.
- [105] A. Garg, A. Bhattacharya, and A. Batish, “Chemical vapor treatment of ABS parts built by FDM: Analysis of surface finish and mechanical strength,” *The International Journal of Advanced Manufacturing Technology*, vol. 89, pp. 2175–2191, mar 2017.
- [106] L. Galantucci, F. Lavecchia, and G. Percoco, “Experimental study aiming to enhance the surface finish of fused deposition modeled parts,” *CIRP Annals*, vol. 58, no. 1, pp. 189–192, 2009.
- [107] M. S. Alsoufi and A. E. Elsayed, “Surface Roughness Quality and Dimensional Accuracy—A Comprehensive Analysis of 100% Infill Printed Parts Fabricated by a Personal/Desktop Cost-Effective FDM 3D Printer,” *Materials Sciences and Applications*, vol. 09, no. 01, pp. 11–40, 2018.
- [108] “Vacodym - Vacuumschmelze GmbH & Co. KG,” <https://www.vacuumschmelze.de/>, 2018.
- [109] “Magnetfabrik Bonn: Produkte: Magnete nach Formgebung: Spritzguss,” [https://www.magnetfabrik.de/magnetfabrik\\_de/](https://www.magnetfabrik.de/magnetfabrik_de/), 2018.
- [110] J. Linneweber, P. M. Dohmen, U. Kerzschner, K. Affeld, Y. Nosé, and W. Konertz, “The effect of surface roughness on activation of the coagulation system and platelet adhesion in rotary blood pumps,” *Artificial Organs*, vol. 31, no. 5, pp. 345–351, 2007.
- [111] Y. Kim, H. Yuk, R. Zhao, S. A. Chester, and X. Zhao, “Printing ferromagnetic domains for untethered fast-transforming soft materials,” *Nature*, vol. 558, no. 7709, pp. 274–279, 2018.

## BIBLIOGRAPHY

- [112] J. R. Kennington, S. H. Frankel, J. Chen, S. C. Koenig, M. A. Sobieski, G. A. Giridharan, and M. D. Rodefled, “Design Optimization and Performance Studies of an Adult Scale Viscous Impeller Pump for Powered Fontan in an Idealized Total Cavopulmonary Connection,” *Cardiovascular Engineering and Technology*, vol. 2, no. 4, pp. 237–243, 2011.
- [113] E. Okamoto, T. Hashimoto, T. Inoue, and Y. Mitamura, “Blood compatible design of a pulsatile blood pump using computational fluid dynamics and computer-aided design and manufacturing technology,” *Artificial Organs*, vol. 27, no. 1, pp. 61–67, 2003.
- [114] D. Rajenthirakumar and K. A. Jagadeesh, “Analysis of interaction between geometry and efficiency of impeller pump using rapid prototyping,” *The International Journal of Advanced Manufacturing Technology*, vol. 44, pp. 890–899, oct 2009.
- [115] C. H. Chan, I. L. Pieper, R. Hambly, G. Radley, A. Jones, Y. Friedmann, K. M. Hawkins, S. Westaby, G. Foster, and C. A. Thornton, “The CentriMag Centrifugal Blood Pump as a Benchmark for In Vitro Testing of Hemocompatibility in Implantable Ventricular Assist Devices,” *Artificial Organs*, vol. 39, pp. 93–101, feb 2015.
- [116] “Context 3D Printing Report.,” <https://contextworld.com/>, 2019.
- [117] N. S. Cheng, “Formula for the viscosity of a glycerol-water mixture,” *Industrial and Engineering Chemistry Research*, vol. 47, no. 9, pp. 3285–3288, 2008.
- [118] ASTM International, “F1841-19 Standard Practice for Assessment of Hemolysis in Continuous Flow Blood Pumps,” *ASTM Standards*, vol. 13, no. Reapproved 2013, pp. 1–5, 2019.
- [119] M. Harboe, “A Method for Determination of Hemoglobin in Plasma by Near-Ultraviolet Spectrophotometry,” *Scandinavian Journal of Clinical and Laboratory Investigation*, vol. 11, pp. 66–70, jan 1959.



- [120] S. N. Wood, N. Pya, and B. Säfken, “Smoothing Parameter and Model Selection for General Smooth Models,” *Journal of the American Statistical Association*, vol. 111, no. 516, pp. 1548–1563, 2016.
- [121] O. Maruyama, Y. Numata, M. Nishida, T. Yamane, I. Oshima, Y. Adachi, and T. Masuzawa, “Hemolysis caused by surface roughness under shear flow,” *Journal of Artificial Organs*, vol. 8, no. 4, pp. 228–236, 2005.
- [122] H. Schlichting and K. Gersten, *Boundary-layer theory*. Springer, 2016.
- [123] T. Adams, C. Grant, and H. Watson, “A Simple Algorithm to Relate Measured Surface Roughness to Equivalent Sand-grain Roughness,” *International Journal of Mechanical Engineering and Mechatronics*, vol. 1, no. 1, 2012.
- [124] M. V. Kameneva and J. F. Antaki, “Mechanical trauma to blood,” *Biomedical and Health Research-Commission of the European Communities Then IOS Press*, vol. 69, p. 206, 2007.
- [125] C. H. H. Chan, I. L. Pieper, C. R. Robinson, Y. Friedmann, V. Kanamarlapudi, and C. A. Thornton, “Shear Stress-Induced Total Blood Trauma in Multiple Species,” *Artificial Organs*, vol. 41, pp. 934–947, oct 2017.
- [126] R. A. Malinauskas, “Plasma Hemoglobin Measurement Techniques for the In Vitro Evaluation of Blood Damage Caused by Medical Devices,” *Artificial Organs*, vol. 21, no. 12, pp. 1255–1267, 2008.
- [127] K. Naito, E. Suenaga, Z. L. Cao, H. Suda, T. Ueno, M. Natsuaki, and T. Itoh, “Comparative hemolysis study of clinically available centrifugal pumps,” *Artificial organs*, vol. 20, no. 6, pp. 560–3, 1996.
- [128] D. M. Saylor, P. W. Buehler, R. P. Brown, and R. A. Malinauskas, “Predicting Plasma Free Hemoglobin Levels in Patients Due to Medical Device-Related Hemolysis,” *ASAIO Journal*, vol. 65, pp. 207–218, mar 2019.

## BIBLIOGRAPHY

- [129] L. H. Herbertson, S. E. Olia, A. Daly, C. P. Noatch, W. A. Smith, M. V. Kameneva, and R. A. Malinauskas, “Multilaboratory study of flow-induced hemolysis using the FDA benchmark nozzle model,” *Artificial organs*, vol. 39, no. 3, pp. 237–248, 2015.
- [130] S. M. Bowley and R. A. Malinauskas, “Evaluation Of Parameters Affecting Bovine Blood Hemolysis Testing,” *Delta*, vol. 140, p. 160, 2003.
- [131] K. H. Fraser, M. E. Taskin, B. P. Griffith, and Z. J. Wu, “The use of computational fluid dynamics in the development of ventricular assist devices,” *Medical Engineering & Physics*, vol. 33, pp. 263–280, apr 2011.
- [132] J. Apel, R. Paul, S. Klaus, T. Siess, and H. Reul, “Assessment of Hemolysis Related Quantities in a Microaxial Blood Pump by Computational Fluid Dynamics,” *Artificial Organs*, vol. 25, pp. 341–347, may 2001.
- [133] K. Naito, K. Mizuguchi, and Y. Nose, “The Need for Standardizing the Index of Hemolysis,” vol. 8, no. 1, pp. 7–10, 1994.
- [134] K. Mizuguchi, G. A. Damm, G. S. Aber, R. J. Bozeman, J. W. Bacak, P. A. Svejksky, Y. Orime, Y. Ohara, K. Naito, K. Tassai, K. Makinouchi, S. Takatani, Y. Nosé, G. P. Noon, and M. E. DeBakey, “Does Hematocrit Affect In Vitro Hemolysis Test Results? Preliminary Study with Baylor/NASA Prototype Axial Flow Pump,” *Artificial Organs*, vol. 18, pp. 650–656, sep 1994.
- [135] K. Mizuguchi, S. Kitamura, G. Damm, R. Benkowsky, J. Glueck, G. Aber, J. Bacak, P. Svjkovsky, Y. Nosé, G. P. Noon, and M. E. Debakey, “In Vitro Hemolysis Test Method for Developing an Axial Flow Ventricular Assist Device,” in *Heart Replacement*, vol. 66, pp. 237–243, Tokyo: Springer Japan, 1996.
- [136] M. Mueller, H. Schima, H. Engelhardt, A. Salat, D. Olsen, U. Losert, and E. Wolner, “In Vitro Hematological Testing of Rotary Blood Pumps: Remarks on Standardization and Data

- Interpretation,” *Artificial Organs*, vol. 17, pp. 103–110, nov 2008.
- [137] S. E. Olia, L. H. Herbertson, R. A. Malinauskas, and M. V. Kameneva, “A Reusable, Compliant, Small Volume Blood Reservoir for In Vitro Hemolysis Testing,” *Artificial Organs*, vol. 41, pp. 175–178, feb 2017.
- [138] L. Wiegmann, D. A. de Zélicourt, O. Speer, A. Muller, J. S. Goede, B. Seifert, and V. Kurtcuoglu, “Influence of Standard Laboratory Procedures on Measures of Erythrocyte Damage,” *Frontiers in Physiology*, vol. 8, pp. 1–11, sep 2017.
- [139] ASTM International, “F1830-19 Standard Practice for Collection and Preparation of Blood for Dynamic in vitro Evaluation of Hemolysis in Blood Pumps,” *ASTM Standards*, vol. 18, no. 9, pp. 18–20, 2019.
- [140] C. H. H. Chan, K. K. Ki, I. Y. Chu, J. Rolls, S. Morris, T. J. Lee, S. Bindorfer, J. P. Pauls, I. Idachi, and J. F. Fraser, “In vitro Hemocompatibility Evaluation of the HeartWare Ventricular Assist Device Under Systemic, Pediatric and Pulmonary Support Conditions,” *ASAIO Journal*, vol. Publish Ah, jul 2020.
- [141] L. Kuck, M. J. Simmonds, C. H. H. Chan, J. P. Pauls, G. D. Tansley, F. Feldmann, and A. P. McNamee, “Ex vivo assessment of erythrocyte tolerance to the HeartWare ventricular assist device operated in three discrete configurations,” *Artificial Organs*, dec 2020.
- [142] W. Sun, S. Wang, Z. Chen, J. Zhang, T. Li, K. Arias, B. P. Griffith, and Z. J. Wu, “Impact of high mechanical shear stress and oxygenator membrane surface on blood damage relevant to thrombosis and bleeding in a pediatric ECMO circuit,” *Artificial Organs*, vol. 44, no. 7, pp. 717–726, 2020.
- [143] G. Radley, I. L. Pieper, C. R. Robinson, S. Ali, M. Beshr, O. Bodger, and C. A. Thornton, “In Vitro Benchmarking Study of Ventricular Assist Devices in Current Clinical Use,” *Journal of Cardiac Failure*, vol. 26, pp. 70–79, jan 2020.

## BIBLIOGRAPHY

- [144] E. Woelke, M. Klein, I. Mager, T. Schmitz-Rode, U. Steinseifer, J. Arens, and J. C. Clauser, “Miniaturized Test Loop for the Assessment of Blood Damage by Continuous-Flow Left-Ventricular Assist Devices,” *Annals of Biomedical Engineering*, vol. 48, pp. 768–779, feb 2020.
- [145] C. H. H. Chan, D. Nandakumar, N. Balletti, J. Horobin, E. L.-J. Wu, M. Bouquet, A. Stephens, J. P. Pauls, G. Tansley, J. F. Fraser, M. J. Simmonds, and S. D. Gregory, “In Vitro Hemocompatibility Evaluation of Modified Rotary Left to Right Ventricular Assist Devices in Pulmonary Flow Conditions,” *ASAIO Journal*, vol. 66, pp. 637–644, jun 2020.
- [146] M. Nikfar, M. Razizadeh, J. Zhang, R. Paul, Z. J. Wu, and Y. Liu, “Prediction of mechanical hemolysis in medical devices via a Lagrangian strain-based multiscale model,” *Artificial Organs*, vol. 44, pp. 348–368, aug 2020.
- [147] J. Ding, S. Niu, Z. Chen, T. Zhang, B. P. Griffith, and Z. J. Wu, “Shear-Induced Hemolysis: Species Differences,” *Artificial Organs*, vol. 39, pp. 795–802, sep 2015.
- [148] A. Makhro, R. Huisjes, L. P. Verhagen, M. d. M. Mañú-Pereira, E. Llaudet-Planas, P. Petkova-Kirova, J. Wang, H. Eichler, A. Bogdanova, R. van Wijk, J. L. Vives-Corrans, and L. Kaestner, “Red cell properties after different modes of blood transportation,” *Frontiers in Physiology*, vol. 7, no. JUL, 2016.
- [149] C. R. Sargent, I. L. Perkins, V. Kanamarlapudi, C. Moriarty, and S. Ali, “Hemodilution Increases the Susceptibility of Red Blood Cells to Mechanical Shear Stress During In Vitro Hemolysis Testing,” *ASAIO Journal*, vol. online, pp. 1–10, sep 2020.
- [150] S. K. Doke and S. C. Dhawale, “Alternatives to animal testing: A review,” *Saudi Pharmaceutical Journal*, vol. 23, no. 3, pp. 223–229, 2015.
- [151] R. Paul, J. Apel, S. Klaus, F. Schugner, P. Schwindke, and H. Reul, “Shear Stress Related Blood Damage in Laminar Couette Flow,” *Artificial Organs*, vol. 27, pp. 517–529, jun 2003.

- [152] T. Zhang, M. E. Taskin, H.-B. Fang, A. Pampori, R. Jarvik, B. P. Griffith, and Z. J. Wu, “Study of Flow-Induced Hemolysis Using Novel Couette-Type Blood-Shearing Devices,” *Artificial Organs*, vol. 35, pp. 1180–1186, dec 2011.
- [153] F. Boehning, T. Mejia, T. Schmitz-Rode, and U. Steinseifer, “Hemolysis in a Laminar Flow-Through Couette Shearing Device: An Experimental Study,” *Artificial Organs*, vol. 38, jun 2014.
- [154] J. Guo, L. Hou, J. Hou, J. Yu, and Q. Hu, “Generation of Ultra-Thin-Shell Microcapsules Using Osmolarity-Controlled Swelling Method,” *Micromachines*, vol. 11, p. 444, apr 2020.
- [155] N. Doshi, A. S. Zahr, S. Bhaskar, J. Lahann, and S. Mitragotri, “Red blood cell-mimicking synthetic biomaterial particles,” *Proceedings of the National Academy of Sciences*, vol. 106, pp. 21495–21499, dec 2009.
- [156] M. N. Holme, I. A. Fedotenko, D. Abegg, J. Althaus, L. Babel, F. Favarger, R. Reiter, R. Tanasescu, P.-L. Zaffalon, A. Ziegler, B. Müller, T. Saxer, and A. Zumbuehl, “Shear-stress sensitive lenticular vesicles for targeted drug delivery,” *Nature Nanotechnology*, vol. 7, pp. 536–543, aug 2012.
- [157] M. Hu, S. Peil, Y. Xing, D. Döhler, L. Caire da Silva, W. H. Binder, M. Kappl, and M. B. Bannwarth, “Monitoring crack appearance and healing in coatings with damage self-reporting nanocapsules,” *Materials Horizons*, vol. 5, no. 1, pp. 51–58, 2018.
- [158] E. T. A. van den Dungen, B. Loos, and B. Klumperman, “Use of a Profluorophore for Visualization of the Rupture of Capsules in Self-Healing Coatings,” *Macromolecular Rapid Communications*, vol. 31, pp. 625–628, apr 2010.
- [159] O. Maruyama, K. Yamaguchi, M. Nishida, T. Onoguchi, T. Tsutsui, T. Jikuya, and T. Yamane, “Hemolytic Evaluation Using Polyurethane Microcapsule Suspensions in Circula-

## BIBLIOGRAPHY

- tory Support Devices: Normalized Index of Hemolysis Comparisons of Commercial Centrifugal Blood Pumps,” *Artificial Organs*, vol. 32, pp. 146–156, feb 2008.
- [160] O. Maruyama, T. Yamane, M. Nishida, A. Aouidef, T. Tsutsui, T. Jikuya, and T. Masuzawa, “Fractural Characteristic Evaluation of a Microcapsule Suspension Using a Rotational Shear Stressor,” *ASAIO Journal*, vol. 48, pp. 365–373, jul 2002.
- [161] O. Maruyama, T. Yamane, N. Tsunemoto, M. Nishida, T. Tsutsui, and T. Jikuya, “A Preliminary Study of Microcapsule Suspension for Hemolysis Evaluation of Artificial Organs,” *Artificial Organs*, vol. 23, pp. 274–279, mar 1999.
- [162] Y. Ootaki, K. Kamohara, D. Horvath, A. Massiello, L. Golding, B. Lukic, W. Weiss, O. Maruyama, and K. Fukamachi, “Hemolysis Evaluation of Centrifugal Pumps Using Microcapsule Suspension,” *The International Journal of Artificial Organs*, vol. 29, pp. 1185–1189, dec 2006.
- [163] I. El-Gibaly and M. Anwar, “Hemolysate-filled polyethyleneimine and polyurea microcapsules as potential red blood cell substitutes: effect of aqueous monomer type on properties of the prepared microcapsules,” *International Journal of Pharmaceutics*, vol. 278, pp. 25–40, jun 2004.
- [164] D. E. Discher and F. Ahmed, “Polymersomes,” *Annual Review of Biomedical Engineering*, vol. 8, pp. 323–341, aug 2006.
- [165] A. Ofner, I. Mattich, M. Hagander, A. Dutto, H. Seybold, P. A. Rühls, and A. R. Studart, “Controlled Massive Encapsulation via Tandem Step Emulsification in Glass,” *Advanced Functional Materials*, vol. 29, jan 2019.
- [166] M. Pohl, O. Samba, M. O. Wendt, and G. Vlastos, “Shear stress related hemolysis and its modelling by mechanical degradation of polymer solutions,” *The International Journal of Artificial Organs*, vol. 21, no. 2, pp. 107–113, 1998.

- [167] M. Pohl, M. O. Wendt, B. Koch, and G. Vlastos, “Mechanical degradation of polyacrylamide solutions as a model for flow induced blood damage in artificial organs,” *Biorheology*, vol. 37, no. 4, pp. 313–324, 2000.
- [168] M. Pohl, M. Wendt, B. Koch, R. Kühnei, O. Samba, and G. Vlastos, “Modellfluide für Blut bei der In-vitro-Testung künstlicher Herzklappen,” *Zeitschrift für Medizinische Physik*, vol. 11, no. 3, pp. 187–194, 2001.
- [169] R. E. Goldstein, “Green Algae as Model Organisms for Biological Fluid Dynamics,” *Annual Review of Fluid Mechanics*, vol. 47, pp. 343–375, jan 2015.
- [170] C. Wang and C. Q. Lan, “Effects of shear stress on microalgae – A review,” *Biotechnology Advances*, vol. 36, pp. 986–1002, jul 2018.
- [171] E. M. Spiden, P. J. Scales, S. E. Kentish, and G. J. Martin, “Critical analysis of quantitative indicators of cell disruption applied to *Saccharomyces cerevisiae* processed with an industrial high pressure homogenizer,” *Biochemical Engineering Journal*, vol. 70, pp. 120–126, jan 2013.
- [172] L. B. Leverett, J. D. Hellums, C. P. Alfrey, and E. C. Lynch, “Red Blood Cell Damage by Shear Stress,” *Biophysical Journal*, vol. 12, no. 3, pp. 257–273, 1972.
- [173] A. M. Sallam and N. H. Hwang, “Human red blood cell hemolysis in a turbulent shear flow: Contribution of Reynolds shear stresses,” *Biorheology*, vol. 21, pp. 783–797, dec 1984.
- [174] A. Overbeck, I. Kampen, and A. Kwade, “Mechanical characterization of yeast cells: effects of growth conditions,” *Letters in Applied Microbiology*, vol. 61, pp. 333–338, oct 2015.
- [175] H. Lange, P. Taillandier, and J. P. Riba, “Effect of high shear stress on microbial viability,” *Journal of Chemical Technology and Biotechnology*, vol. 76, pp. 501–505, may 2001.

## BIBLIOGRAPHY

- [176] J. Leiva and E. Geffroy, “Evolution of the Size Distribution of an Emulsion under a Simple Shear Flow,” *Fluids*, vol. 3, p. 46, jun 2018.
- [177] G. Chen and D. Tao, “An experimental study of stability of oil–water emulsion,” *Fuel Processing Technology*, vol. 86, pp. 499–508, feb 2005.
- [178] C. Zhou, M. K. Hedayati, and A. Kristensen, “Multifunctional waveguide interferometer sensor: simultaneous detection of refraction and absorption with size-exclusion function,” *Optics Express*, vol. 26, pp. 24372–24383, sep 2018.
- [179] C. Zhou, M. Keshavarz Hedayati, X. Zhu, F. Nielsen, U. Levy, and A. Kristensen, “Optofluidic Sensor for Inline Hemolysis Detection on Whole Blood,” *ACS Sensors*, vol. 3, pp. 784–791, apr 2018.
- [180] M. Kersaudy-Kerhoas and E. Sollier, “Micro-scale blood plasma separation: from acoustophoresis to egg-beaters,” *Lab on a Chip*, vol. 13, pp. 3323–3346, 2013.
- [181] M. Matthiae, X. Zhu, R. Marie, and A. Kristensen, “In-line whole blood fractionation for Raman analysis of blood plasma,” *The Analyst*, vol. 144, no. 2, pp. 602–610, 2019.
- [182] S. Tripathi, Y. V. B. Kumar, A. Agrawal, A. Prabhakar, and S. S. Joshi, “Microdevice for plasma separation from whole human blood using bio-physical and geometrical effects,” *Scientific Reports*, vol. 26749, pp. 1–15, jun 2016.
- [183] M. Robinson, H. Marks, T. Hinsdale, K. Maitland, and G. Coté, “Rapid isolation of blood plasma using a cascaded inertial microfluidic device,” *Biomicrofluidics*, vol. 11, pp. 1–15, mar 2017.
- [184] T. Kwon, H. Prentice, J. De Oliveira, N. Madziva, M. E. Warkiani, J.-F. P. Hamel, and J. Han, “Microfluidic Cell Retention Device for Perfusion of Mammalian Suspension Culture,” *Scientific Reports*, vol. 7, p. 6703, dec 2017.



- [185] J. Marchalot, Y. Fouillet, and J.-L. Achard, “Multi-step microfluidic system for blood plasma separation: architecture and separation efficiency,” *Microfluidics and Nanofluidics*, vol. 17, pp. 167–180, jul 2014.
- [186] T. Laurell, F. Petersson, and A. Nilsson, “Chip integrated strategies for acoustic separation and manipulation of cells and particles,” *Chem. Soc. Rev.*, vol. 36, no. 3, pp. 492–506, 2007.
- [187] H. Jiang, X. Weng, C. H. Chon, X. Wu, and D. Li, “A microfluidic chip for blood plasma separation using electro-osmotic flow control,” *Journal of Micromechanics and Microengineering*, vol. 21, aug 2011.
- [188] H. Gong, B. P. Bickham, A. T. Woolley, and G. P. Nordin, “Custom 3D printer and resin for  $18\ \mu\text{m} \times 20\ \mu\text{m}$  microfluidic flow channels,” *Lab on a Chip*, vol. 17, no. 17, pp. 2899–2909, 2017.
- [189] Y. Ren, S. Ray, and Y. Liu, “Reconfigurable Acrylic-tape Hybrid Microfluidics,” *Scientific Reports*, vol. 9, dec 2019.
- [190] D. I. Walsh, D. S. Kong, S. K. Murthy, and P. A. Carr, “Enabling Microfluidics: from Clean Rooms to Makerspaces,” *Trends in Biotechnology*, vol. 35, pp. 383–392, may 2017.
- [191] A. K. Tran, A. Sapkota, J. Wen, J. Li, and M. Takei, “Linear relationship between cytoplasm resistance and hemoglobin in red blood cell hemolysis by electrical impedance spectroscopy & eight-parameter equivalent circuit,” *Biosensors and Bioelectronics*, vol. 119, pp. 103–109, nov 2018.
- [192] C. G. Olthof, P. M. J. M. de Vries, P. M. Kouw, P. L. Oe, H. Schneider, J. J. de Lange, and A. J. M. Donker, “Non-invasive conductivity method for detection of dynamic body fluid changes: in vitro and in vivo validation,” *Nephrology Dialysis Transplantation*, vol. 8, no. 1, pp. 41–46, 1993.
- [193] E. Treo, C. Felice, M. Tirado, M. Valentinuzzi, and D. Cervantes, “Comparative Analysis of Hematocrit Measurements by

## BIBLIOGRAPHY

- Dielectric and Impedance Techniques,” *IEEE Transactions on Biomedical Engineering*, vol. 52, pp. 549–552, mar 2005.
- [194] F. Jaspard, M. Nadi, and A. Rouane, “Dielectric properties of blood: an investigation of haematocrit dependence,” *Physiological Measurement*, vol. 24, pp. 137–147, feb 2003.
- [195] E. Treo, C. Felice, M. Tirado, M. Valentinuzzi, and D. Cervantes, “Hematocrit Measurement by Dielectric Spectroscopy,” *IEEE Transactions on Biomedical Engineering*, vol. 52, pp. 124–127, jan 2005.
- [196] G. Gárdos, “The function of calcium in the potassium permeability of human erythrocytes,” *Biochimica et Biophysica Acta*, vol. 30, pp. 653–654, dec 1958.
- [197] J. J. Teuteberg, J. C. Cleveland, J. Cowger, R. S. Higgins, D. J. Goldstein, M. Keebler, J. K. Kirklin, S. L. Myers, C. T. Salerno, J. Stehlik, F. Fernandez, V. Badhwar, F. D. Pagani, and P. Atluri, “The Society of Thoracic Surgeons Intermacs 2019 Annual Report: The Changing Landscape of Devices and Indications,” *The Annals of Thoracic Surgery*, vol. 109, pp. 649–660, mar 2020.
- [198] L. Vercaemst, “Hemolysis in cardiac surgery patients undergoing cardiopulmonary bypass: a review in search of a treatment algorithm,” *The journal of extra-corporeal technology*, vol. 40, pp. 257–267, dec 2008.
- [199] J. P. Ferreira, J. Butler, P. Rossignol, B. Pitt, S. D. Anker, M. Kosiborod, L. H. Lund, G. L. Bakris, M. R. Weir, and F. Zannad, “Abnormalities of Potassium in Heart Failure: JACC State-of-the-Art Review,” *Journal of the American College of Cardiology*, vol. 75, no. 22, pp. 2836–2850, 2020.
- [200] B. Walpoth, V. Mehan, R. Rogulenko, B. Aeschbacher, G. Vucic, D. Mettler, U. Althaus, and B. Meier, “Left Heart Bypass in the Pig with a Centrifugal Pump Using Cannulae Prepared for Percutaneous Placement,” *The International Journal of Artificial Organs*, vol. 21, pp. 285–290, may 1998.

- [201] M. Frimat, I. Boudhabhay, and L. T. Roumenina, “Hemolysis Derived Products Toxicity and Endothelium: Model of the Second Hit,” *Toxins*, vol. 11, p. 660, nov 2019.
- [202] C. R. Bartoli, D. Zhang, J. Kang, S. Hennessy-Strahs, D. Restle, J. Howard, G. Redline, C. Bermudez, P. Atluri, and M. A. Acker, “Clinical and In Vitro Evidence That Subclinical Hemolysis Contributes to LVAD Thrombosis,” *The Annals of Thoracic Surgery*, vol. 105, pp. 807–814, mar 2018.
- [203] R. P. Rother, L. Bell, P. Hillmen, and M. T. Gladwin, “The Clinical Sequelae of Intravascular Hemolysis and Extracellular Plasma Hemoglobin,” *JAMA*, vol. 293, p. 1653, apr 2005.
- [204] M. V. Kameneva, J. F. Antaki, K. K. Yeleswarapu, and H. S. Watach, M. J., Griffith, B. P., Borovetz, “Plasma protective effect on red blood cells exposed to mechanical stress.,” *ASAIO Journal*, pp. M571–5, 1997.
- [205] H. Doornenbal, A. K. Tong, and N. L. Murray, “Reference values of blood parameters in beef cattle of different ages and stages of lactation.,” *Canadian journal of veterinary research = Revue canadienne de recherche veterinaire*, vol. 52, pp. 99–105, jan 1988.
- [206] L. Rusoff, J. Johnston, and C. Branton, “Blood Studies of Breeding Dairy Bulls. I. Hematocrit, Hemoglobin, Plasma Calcium, Plasma Inorganic Phosphorus, Alkaline Phosphatase Values, Erythrocyte Count, and Leucocyte Count,” *Journal of Dairy Science*, vol. 37, pp. 30–36, jan 1954.
- [207] I. Radkowska and E. Herbut, “Hematological and biochemical blood parameters in dairy cows depending on the management system,” *Animal Science Papers and Reports*, vol. 32, no. 4, pp. 317–325, 2014.
- [208] D. Vallejo-Timarán, J. Montoya-Zuluaga, V. Castillo-Vanegas, and J. Maldonado-Estrada, “Parity and season affect hematological, biochemical, and milk parameters during the early post-

## BIBLIOGRAPHY

- partum period in grazing dairy cows from high-tropics herds,” *Heliyon*, vol. 6, p. e04049, may 2020.
- [209] L. Golbeck, I. Cohrs, T. Scheu, and W. Grünberg, “Changes of the erythrocyte phenotype and blood biochemistry in dairy calves during the first ten weeks of age,” *PeerJ*, vol. 7, p. e7248, jul 2019.
- [210] L. Roland, M. Drillich, and M. Iwersen, “Hematology as a diagnostic tool in bovine medicine,” *Journal of Veterinary Diagnostic Investigation*, vol. 26, pp. 592–598, sep 2014.
- [211] D. Wood and G. F. Quiroz-Rocha, “Normal hematology of cattle,” in *Schalm’s veterinary hematology* (D. J. Weiss and K. J. Wardrop, eds.), pp. 829–835, Wiley, 6 ed., 2010.
- [212] V. Stankevič and Č. Šimkevičius, “Thermal errors in media-separating housings of pressure sensors,” *Sensors and Actuators, A: Physical*, vol. 75, no. 3, pp. 215–221, 1999.
- [213] S. F. C. Stewart, E. G. Paterson, G. W. Burgreen, P. Hariharan, M. Giarra, V. Reddy, S. W. Day, K. B. Manning, S. Deutsch, M. R. Berman, M. R. Myers, and R. A. Malinauskas, “Assessment of CFD Performance in Simulations of an Idealized Medical Device: Results of FDA’s First Computational Interlaboratory Study,” *Cardiovascular Engineering and Technology*, vol. 3, no. 2, pp. 139–160, 2012.
- [214] F. R. Menter, “Two-equation eddy-viscosity turbulence models for engineering applications,” *AIAA Journal*, vol. 32, no. 8, pp. 1598–1605, 1994.

# Curriculum Vitae

## Personal Data

Name Kai von Petersdorff-Campen  
Date of birth February 2, 1992, Germany  
Nationality German

## Education

2017 – 2021 PhD candidate in mechanical engineering, Product Development Group Zurich, ETH Zurich, Switzerland  
2016 – 2017 Master thesis in metal physics and biocorrosion, Laboratory of Metal Physics and Technology, ETH Zurich, Switzerland  
2011 – 2017 Master of science in material science (best of class), RWTH Aachen University, Germany  
2002 – 2010 High school education, Quirinus Gymnasium Neuss, Germany

## Professional Experience

2018 – 2020 Project Lead, Design and Technology Lab, Zurich, Switzerland  
since 2017 Founder, Collision avoidance system for water sports, Rowcus (Radian GmbH), Zurich, Switzerland  
2015 Intern, Graphene additives for silicone rubbers, Cabot Corporation, Boston, MA, USA  
2012 – 2013 Tutor, Institute for Crystallography, RWTH Aachen University, Germany

## **Honors**

- |           |  |
|-----------|--|
| 2019      | Third Place - Global Case Competition, Cambridge Consulting Network  |
| 2018      | Award recipient of the Mock Circulation Loop Challenge of the American Society of Artificial Internal Organs (ASAIO) |
| 2016      | proRWTH Springorum Award for Academic Excellence   |
| 2016–2017 | IDEA League Student Research Grant   |
| 2012–2017 | Scholar of the German National Academic Foundation   |
| 2012–2017 | Member of the RWTH Dean's List   |

## List of Publications

### Ventricular Assist Devices

von Petersdorff-Campen, K., Schmid Daners, M., Meboldt, M. (2018). Overcoming the limits of design: Magnet 3D printing for rapid development of turbodynamic ventricular assist devices. *ASAIO Journal*, Vol. 64, No. Supplement 1

von Petersdorff-Campen, K., Hauswirth, Y., Carpenter, J., Hagmann, A., Boës, S., Schmid Daners, M., Penner, D., Meboldt, M. (2018). 3D printing of functional assemblies with integrated polymer-bonded magnets demonstrated with a prototype of a rotary blood pump. *Applied Sciences*, 8(8), 1275.

von Petersdorff-Campen, K., Abeken, J., De Zélicourt, D., Kurtcuoglu, V., Meboldt, M., Schmid Daners, M. (2020). In Vitro Testing and Comparison of Additively Manufactured Polymer Impellers for the CentriMag Blood Pump. *ASAIO Journal* Vol. 67 No. 3.

von Petersdorff-Campen, K., Schmid Daners, M. (2021). Hemolysis testing in vitro: A review of challenges and potential improvements. *ASAIO Journal (online first)*.

von Petersdorff-Campen, K., Fischer, P., Bogdanova, A., & Schmid Daners, M. (2021). Potential factors behind poor reproducibility of in vitro hemolysis testing. *ASAIO Journal (online first)*.

von Petersdorff-Campen, K., Dupuch, M., , Meboldt, M., Hierold, C., & Schmid Daners, M. (2021). Pressure and Bernoulli-based Flow Measurement via a Tapered Inflow VAD Cannula. *IEEE Transactions on Biomedical Engineering (online first)*.

### Ventilators for Covid-19

Meboldt, M., von Petersdorff-Campen, K., Boës, S., & Batliner, M. (2020). Deployment of ventilators to developing countries: A critical review in light of the Covid-19 crisis: A report for the national Covid-19 scientific taskforce and the executive board of ETH Zurich. ETH research collection, available online: <https://www.research-collection.ethz.ch/handle/20.500.11850/456250>